NON-DISSOCIATIVE SINGLE-ELECTRON IONIZATION OF DIATOMIC MOLECULES

by

WES CORBIN ERBSEN

B.Sc., East Tennessee State University, 2008

A THESIS

submitted in partial fulfillment of the

requirements for the degree

MASTER OF SCIENCE

Department of Physics

College of Arts and Sciences

KANSAS STATE UNIVERSITY

Manhattan, Kansas

2013

Approved by:

Major Professor

Carlos Trallero

Copyright

Abstract

Over the past four decades, the single-electron ionization of atoms has been a subject of great interest within the ultra-fast community. While contemporary *atomic* ionization models tend to agree well with experiment across a wide range of intensities ($10^{13} - 10^{15}$ W/cm^2), analogous models for the ionization of *molecules* are currently lacking in accuracy. The deficiencies present in molecular ionization models constitute a formidable barrier for experimentalists, who wish to model the single-electron ionization dynamics of molecules in intense laser fields.

The primary motivation for the work presented in this thesis is to provide a comprehensive data set which can be used to improve existing models for the strong-field ionization of molecules. Our approach is to simultaneously measure the singly-charged ion yield of a diatomic molecule paired with a noble gas atom, both having commensurate ionization potentials. These measurements are taken as a function of the laser intensity, typically spanning two orders of magnitude ($10^{13} - 10^{15}$ W/cm^2). By taking the ratio of the *molecular* to *atomic* yields as a function of laser intensity, it is possible to "cancel out" systematic errors which are common to both species, *e.g.* from laser instability, or temperature fluctuations. This technique is very powerful in our ionization studies, as it alludes to the distinct mechanisms leading to the ionization of both molecular and atomic species at the same intensity which are not a function of the experimental conditions. By using the accurate treatments of atomic ionization in tandem with existing molecular ionization models as a benchmark, we can use our experimental ratios to modify existing molecular ionization theories. We hope that the data procured in this thesis will be used in the development of more accurate treatments describing the strong-field ionization of molecules.

[This page intentionally left blank]

Table of Contents

[This page intentionally left blank]

List of Figures

[This page intentionally left blank]

List of Tables

[This page intentionally left blank]

Acknowledgments

I would first like to thank my advisor and mentor, Dr. Carlos Trallero, who not only supported my research in J.R. Macdonald Lab over the years, but also provided valuable feedback along every step of the way. I would also like to thank my group members, especially Stefan Zigo, Pratap Timilsina and Derrek Wilson, who have never hesitated in helping me with whatever I needed, whenever I needed it. In addition, I thank Varun Makhija and Xiaoming Ren for their help with the laser system, and also their willingness to lend a hand in the middle of the night.

I would also like to thank my committee members, Dr. Artem Rudenko and Dr. Vinod Kumarappan, who provided very useful feedback, and always made time to discuss important aspects of my research. In addition, I thank Dr. Brian Washburn for always giving sound advice when it was needed most. I wish to thank Hui Li and Dr. Lew Cocke for teaching me many useful experimental techniques, and also for training me in the use of the VMI-TOFMS, which was used throughout this work.

I would also like to acknowledge the support staff, including Bob Krause, Al Rankin, Mike Wells, Vince Needham, Scott Chainey and Charles Fehrenbach, for providing support and for tolerating my inquisitiveness and relentless attention to detail. I also extend a special thanks to Dr. Anh-Thu Le, who provided the theory used in this work.

Not the least of all, I wish to thank all my fellow graduate students, who have not only provided a continuous source of much-needed support over the years, but also served as a source of entertainment.

[This page intentionally left blank]

Dedication

I dedicate this thesis to my family, who encouraged me to follow my dreams and supported me every step of the way. You mean everything to me.

[This page intentionally left blank]

Chapter 1

Introduction & Background

1.1 Scope of this Thesis

Over the past four decades, the single-electron ionization of atoms has been a subject of great interest within the ultra-fast community [1–4], and contemporary ionization models tend to agree well with experiment [5–8]. However, analogous models for the ionization of molecules are currently lacking in accuracy [9–11]. The deficiencies present in molecular ionization models constitute a formidable barrier for experimentalists, who wish to model single-electron ionization dynamics of molecules in intense laser fields. The primary motivation for our molecular ionization experiments in this work is to provide additional experimental data that can be directly compared with existing theoretical models for molecular ionization. The data which we collect will be used in the development of more accurate treatments describing the strong-field ionization of molecules.

We approach this problem by making simultaneous measurements of the total ionization yield for a molecule/atom pair having similar ionization potentials. The intensity-dependent ionization yields for the singly charged ions for both the molecule and atom are divided, producing a M^+:A^+ ratio which spans the intensity range of the simultaneously measured ion yields. By taking the *ratio* of both simultaneous measurements, we can eliminate effects due to the experimental conditions at the time the data was collected, such as instantaneous fluctuations in the laser intensity or alignment. Using the accurate treatments for atomic ionization models as a benchmark, we can use this ratio to modify existing molecular ionization theories. This ratio of the molecular species to the atomic

species is the main result we wish to obtain in this work.

The first two chapters constitute the introduction and motivation to this study; an introduction to the concepts relevant to strong-field processes are discussed below, while a summary of current atomic and molecular ionization theories are presented in Chapter 2. The experimental details of our measurements are presented in Chapter 3, which includes discussions on the experimental techniques used to gather our data. The results of our ionization experiments are contained within Chapter 4, where we analyze our results and discuss the physical interpretations and compare with other similar measurements. Chapter 5 constitutes other experimental developments procured in the study of strong-field ultra-fast phenomena, with special focus on the development of a new pulse shaper design.

1.2 Single-Electron Ionization of Atoms and Molecules

Single electron ionization from atoms exposed to short intense laser pulses is one of the most fundamental and well studied photoinduced reactions in nonlinear strong-field physics. In this section, we will discuss the different ionization mechanisms responsible for the removal of a single electron from an atom. Before any external field is applied, as in Fig. 1.1(a), the electron is bound only by the static Coulomb potential generated by the positively charged atomic nucleus. In this state, the electron is bound-state energy with $E = -E_{\mathrm{B}}$, where E_{B} is the binding potential of the atomic core. In this case, the electron is permanently confined to the Coulomb potential and the system will not be ionized, which is the case in Fig. 1.1(a).

However, if we slowly turn on an oscillating external electric field, the binding potential becomes distorted. The total effective potential that the electron experiences, $V_{\mathrm{eff}}(r)$, is proportional to superposition of the binding potential, $V(r)$, and the applied field, $V'(r)$, by the following relationship:

$$V_{\mathrm{eff}}(r) = -\frac{Z}{r} - \mathscr{E} r, \tag{1.1}$$

where Z is the net charge of the nucleus, and $\mathscr{E}$ is the applied electric field. The cartoon depicted in

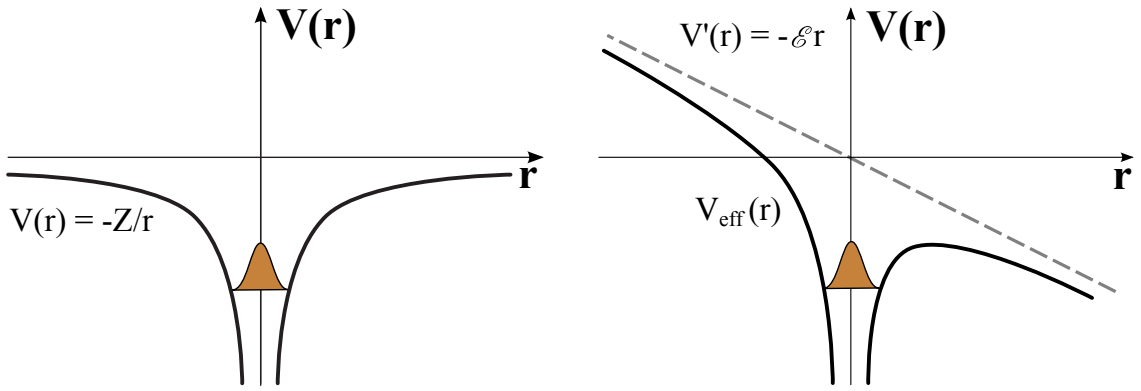

(a) Bound electron in a Coulomb potential

(b) Effective potential distorted by external electric field

Figure 1.1: *Effective binding potential of a generalized atomic system. Figure 1.1(a) represents the static field case resulting in a bound electron. When an oscillating electric field is applied, as in Fig. 1.1(b), the effective potential becomes distorted.*

Fig. 1.1 represents only what happens to the effective binding potential of the electron. The physical mechanism which are responsible for the electron leaving the binding action of the atomic core will be discussed in the following sections. In particular, we will discuss the three primary ionization mechanisms; the idea behind each is depicted in Fig. 1.2.

Multi-photon ionization is a process where an initially bound electron accepts many photons in order to reach continuum. The number of photons absorbed is proportional to the binding energy of the electron divided by the energy of a single photon. Once the electron accepts enough photons to reach continuum, the electron becomes detached. This is depicted in Fig. 1.2(a), and will be discussed in greater detail in §1.2.1 on pg. 4.

Tunneling ionization occurs by suppressing the static Coulomb potential, creating a short potential barrier, as in Fig. 1.2(b). The electron has a non-zero probability of tunneling through this barrier, where it can escape from the binding action of the nucleus. In order for tunneling ionization to occur, the applied electric field must be strong enough to severely distort the static Coulomb potential $V(r)$. For this reason, the onset of tunneling ionization occurs only at high intensities. This will be discussed in §1.2.2.

Over-the-barrier ionization is when the applied electric field is so strong that the effective potential creates a barrier that is below the binding potential of the electron. When this happens, the

electron can simply detach, and an ion is produced. This process can be seen in Fig. 1.2(c), and will be discussed in §1.2.3.

1.2.1 Multi-photon Ionization

Multi-photon ionization is a strong-field process which occurs when an atom or molecule absorbs *multiple* photons, leading to the ionization of the target species [12, 13]. The intensities at which the ionization rate is said to be "multi-photon" is species-dependent, and is quantified using the Keldysh parameter, which is discussed in §1.2.4 on pg. 8. Typical intensity ranges are $10^{10} - 10^{13}$ W/cm^2. Schematically, the reaction of a multi-photon single-electron ionization is described by

$$A + n\hbar\omega \longrightarrow A^+ + e^-,$$

where $\hbar\omega$ is the photon energy of the applied field, and n represents the number of photons absorbed.

We first note that the source of the applied field used in all experiments presented in this work is a Ti:Sapph multi-pass system, having an output characterized by a central wavelength of $\lambda = 800$ nm. For this central wavelength, the energy of a single photon is $E = 1.55$ eV. We also recognize that the lowest ionization potential I_p of all species studied here is Xenon, which has $I_p = 12.13$ eV. Therefore, a single photon does not have enough energy to raise the electron to the continuum [2]. However, ionization still does occur with our laser source in the low-intensity limit; the mechanism responsible is referred to as Multi-photon Ionization (MPI) [2], and is depicted in Fig. 1.2(a).

In the multi-photon limit, the target species absorbs multiple photons until the electron has enough energy to overcome the binding energy of the nucleus. The species is ionized without suppressing the static-field potential. The number of photons needed to raise the electron to the continuum is easily calculated by dividing the ionization potential of the target species by the energy of a single photon. For example, Xenon has $I_p = 12.13$ eV, so a minimum of 8 photons are required for the electron to reach continuum. On the other hand, Argon, having $I_p = 15.76$ eV, requires 11 photons to ionize.* In order to quantify the *rate* at which ionization occurs in the MPI regime,

*If the target species absorbs more than the minimum number of photon required for ionization to occur, then a process often referred to as above-threshold ionization occurs. In this scheme, the continuum electron gains more kinetic energy than in the multi-photon case.

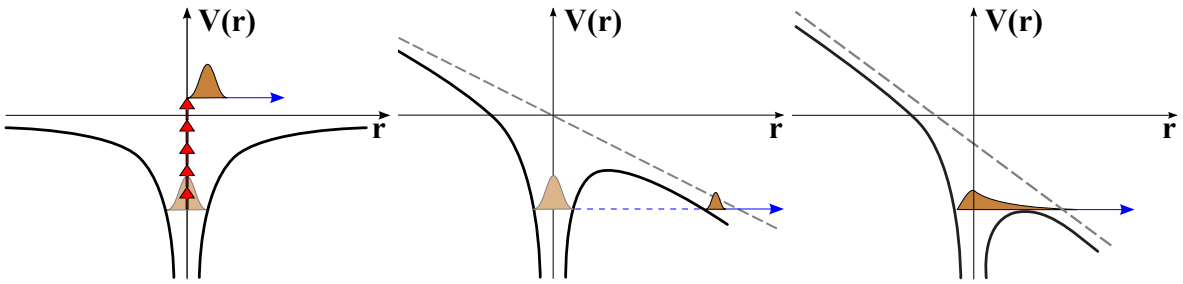

(a) Multi-photon Ionization (b) Tunnel Ionization (c) Over-the-barrier Ionization

Figure 1.2: *Mechanisms of Ionization. It low intensities, MPI dominates, where a multitude of low-energy photons are used to raise the electron to the continuum. At higher intensities, the applied field suppresses the coulomb potential, allowing the electron to tunnel through the effective barrier. At the highest intensities, the effective barrier is suppressed below the binding energy of the electron, allowing to classically ionize.*

we must employ perturbation theory. To first order, applying perturbation theory describes the interaction of a single photon with a single species. The transition dipole amplitude behaves like $|P_{fi}| \propto I_0$. We can directly extend this proportionality to reflect the result obtained through n^{th} order perturbation theory. However, in n^{th} order perturbation theory, then n photons contribute to the ionization of the target species. For the n^{th} order case, the time-dependent expansion coefficients $c_n(t)$ appears n times in the calculation. The transition amplitude in n^{th} order perturbation theory will scale in powers of n as:

$$P_{fi}^n = \sigma_n I_0^n, \tag{1.2}$$

where σ_n is the generalized cross-section, and I_0 is the peak intensity of the driving field. The ionization rate can be found by evaluating the following first order separable differential equation:

$$\frac{dN_1}{dt} = N_0 \sigma_n I_0^n. \tag{1.3}$$

Here N_0 signifies the number of neutral target atoms, and N_1 are the number of ions created. In the lab, what we measure is a signal being generated by the ions created. In general, the term *yield* is used to describe the number of ionization events, and is proportional to N_1. Therefore, by measuring the yield as a function of intensity, we can see how the ionization rate changes as a function of

intensity.

Yield plots are typically plotted in a log-log scale; the reasoning behind this is that, according to (1.3), the ion yield will scale in powers of n in intensity. If we plot the number of ions detected vs. intensity in a log-log scale, then the yield will change linearly with intensity in the low-intensity region. The slope in this region will indicate the number of photons absorbed. This slope, and therefore the multi-photon order, can be evaluated by taking the logarithm of the yield dividing by the logarithm of the intensity:

$$n = \frac{\log\left[\mathrm{d}N_1/\mathrm{d}t\right]}{\log\left[I_0\right]}. \tag{1.4}$$

A theoretical yield plot is presented in Fig. 1.3, where the multi-photon order from (A.1) is evaluated for the intensity-dependent Xe^+ ion yield.

1.2.2 Tunneling Ionization

If the magnitude of the applied field is increased from the multi-photon limit, then at some critical intensity the field becomes large enough to significantly distort the symmetric Coulomb potential, as seen in Fig. 1.1(b). Here we see that with the application of a sufficiently large field, the more the effective potential will bend over, breaking the $1/r$ symmetry of the Coulomb potential and creating a short barrier. It is important to realize that the degree of distortion increases proportional to the intensity. Classically, the electron is still bound to the atomic core, and does not have enough energy to escape to the continuum. In reality, the electron actually has a non-zero probability of ionizing. This is due to *tunneling*. This can be seen in Fig. 1.2(b). For more information on the concept of tunneling, refer to a standard graduate textbook on quantum physics, for example [14, 15].

Unlike MPI processes, which occur by multiple excitation of the electron through intermediate states, TI processes occur by the electron penetrating the barrier. It should be noted that for pure tunneling, the initial and final electronic states have the same total energy. This will be discussed in more detail in Chapter 2.

This is a purely quantum mechanical process – for any non-zero external field, there is a position along the field axis beyond which the binding potential lies below the binding energy. The electron

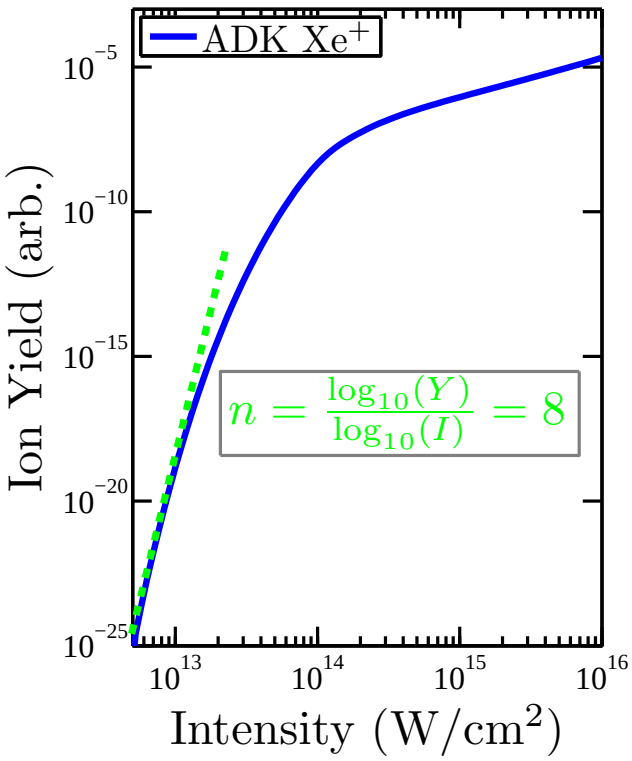

Figure 1.3: *MATLAB ADK yield calculation for the Xe^+ ion. The slope in the MPI regime indicates the multi-photon order, signified by a dashed green line in this plot. We remark that the abrupt change in slope in the vicinity of 10^{14} W/cm^2 is due to saturation of the first charge state within the volume of the laser focus.*

can tunnel through a potential barrier, even when the saddlepoint of the effective potential is well above the bound state energy of the electron. Tunneling ionization occurs before the onset of the classical ionization regime, which is discussed in the next section.

1.2.3 Over-the-barrier Ionization

If the applied field is increased further from the tunneling regime, then the dominant ionization mechanism becomes over-the-barrier ionization occurs. In this regime, the Coulomb potential is suppressed *below* the bound-state energy of the electron, as in Fig. 1.2(c). Therefore, the electron will inevitably "leak out" into the continuum, without having to tunnel through any barrier. It is in this sense that over-the-barrier ionization processes are referred to as a classical ionization mechanism.

No further discussions on over-the-barrier ionization will occur in this work for the following reasons. The required intensity to induce this process are above what is easily reachable with many laser systems. Furthermore, when such intensities are reached, dissociation becomes much more likely to occur. Additionally, at such intensities, many higher charge states are created, since there is enough energy to strip the atom of several valence electrons. We recall that the purpose of this work is to quantify single-electron ionization; In the over-the-barrier ionization regime, the total ion yield of the first charge state will be depleted by the presence of higher charge states.

1.2.4 Classifying Ionization Regimes

Tunneling ionization became an area of intense research in the mid 1960's, and a key principle investigator to this phenomenon was Keldysh. During this time, he realized that it is possible to classify the regime under which ionization occurs based on independent measurements of the experimental conditions. By following this procedure, he discovered that he was able to quantify the regime under which an ionization event occurs. The parameter that he introduced in order to achieve this, now often referred to as the *Keldysh adiabacity parameter*, is defined as [2]:

$$\gamma = \sqrt{\frac{I_\mathrm{p}}{2U_\mathrm{p}}}, \tag{1.5}$$

where I_p is the ionization potential of an atom or molecule, and U_p is the ponderomotive energy of the electron. The ponderomotive potential is qualitatively defined as the amount of kinetic energy that an electron picks up in the oscillating electromagnetic field. Quantitatively, it is defined by:

$$U_\mathrm{p} = \frac{I_0}{4\omega^2}, \tag{1.6}$$

where I_0 is the peak intensity of the electric field, and ω is the frequency of oscillation of the electric field. From (1.5), it is easy to see that the Keldysh parameter is a dimensionless parameter, and is proportional to the ratio of the ionization potential to the amount of energy that the electron picks up in the oscillating electric field.

If an electron gains a small amount of energy from the field compared to the ionization potential,

then it can only reach continuum by occupying intermediate excited states. If, on the other hand, the magnitude of the oscillating electric field is large enough compared to the ionization potential, then the effective binding potential is lowered enough so that the electron can tunnel through the finite residual barrier. Keldysh quantified these two extremes with γ as follows:

$$\gamma > 1 : I_{\mathrm{p}} > U_{\mathrm{p}} \longrightarrow \text{Multi-photon Ionization}$$
$$\gamma < 1 : I_{\mathrm{p}} < U_{\mathrm{p}} \longrightarrow \text{Tunneling Ionization.}$$

The Keldysh parameter may be interpreted in other ways as well. For instance, γ can be thought of as the ratio of the time required to tunnel through the barrier to the oscillation period of the electric field.

Tunneling is more likely to occur when the field is applied for a long time with respect to the oscillation period of the laser field. In terms of the Keldysh parameter, we see that $\gamma < 1$ corresponds to a very slow, deep distortion of the Coulomb potential, letting the electron tunneling out into the continuum. This marks the onset of tunneling ionization. If, however, the driving field oscillates very quickly, then a value of $\gamma > 1$ corresponds to the electron populating more and more energetic states until the electron finally has enough energy to escape. Therefore, we say that a value of $\gamma > 1$ signifies that the electron was ionized in the multi-photon regime.

From these classifications, we recognize that the function of the Keldysh parameter is to mark the vague transition from MPI and TI processes. While this provides a useful metric for predicting the likelihood that ionization will occur in each regime, it should be used with caution. In particular,

Table 1.1: *Keldysh parameter for some common gases*

Species	I_p (eV)	γ @ 10^{13}W/cm^2	γ @ 10^{14}W/cm^2
N_2	15.58	3.60	1.14
Ar	15.76	3.62	1.15
CO	14.01	3.60	1.14
Kr	14.00	3.42	1.08
O_2	13.07	3.17	1.00
Xe	12.13	3.18	1.01

this classification fails when $\gamma = 1$, since no single value of γ represents a sharp transition from one regime to the other. Therefore, we must only use the Keldysh parameter to distinguish between extreme regimes. In fact, in many experiments the actual ionization mechanism can be thought of as a mixture of both MPI and TI processes.

For a real-world example, let's investigate the critical intensity at which Xenon transitions from being in the multi-photon regime or the tunneling regime. This can be evaluated by setting $\gamma = 1$, and solving (1.5) using (1.6) for the intensity, I_0. It turns out that for a driving field centered around $\lambda = 800$ nm, the critical intensity for Xe^+ becomes $I_0 \sim 1.0 \times 10^{14}$ W/cm^2. More examples of the gases used in this work can be seen in Table 1.1.

Furthermore, by inspecting Fig. 1.3, we see that at around an intensity of $\sim 1.0 \times 10^{14}$ W/cm^2, the ion yield no longer follows a linear path. The reason for this is that after saturation of the first charge state, the Xe^+ yield continues to increase due to the growth of the entire focal volume [16, 17]. This effect is sometimes referred to as *volume saturation*, and is an effect caused by increasing the intensity beyond saturation intensity, which leads to a depletion of the Xe^+ ion, and simultaneously causing a sharp rise in the Xe^{++} yield. This will be discussed in more detail in Chapter 4.

1.3 Multiple Ionization of Atoms and Molecules

In this section, we will introduce the concept of multiple-electron ionization. In experimental yield curves for a doubly ionized species (*e.g.*, Xe^{++}), a very unique structure develops along the curve (see Fig. 1.4). We see that there is a very distinctive knee-shaped structure in the Xe^{++} signal [18, 19], which occurs at the interstitial region between the multi-photon limit and the tunneling limit. At this intensity, sequential ionization starts to dominate over non-sequential ionization for increasing intensity. Specifically, we see that this curve exhibits two changes of slope, as opposed to just one in the singly-charged ion.

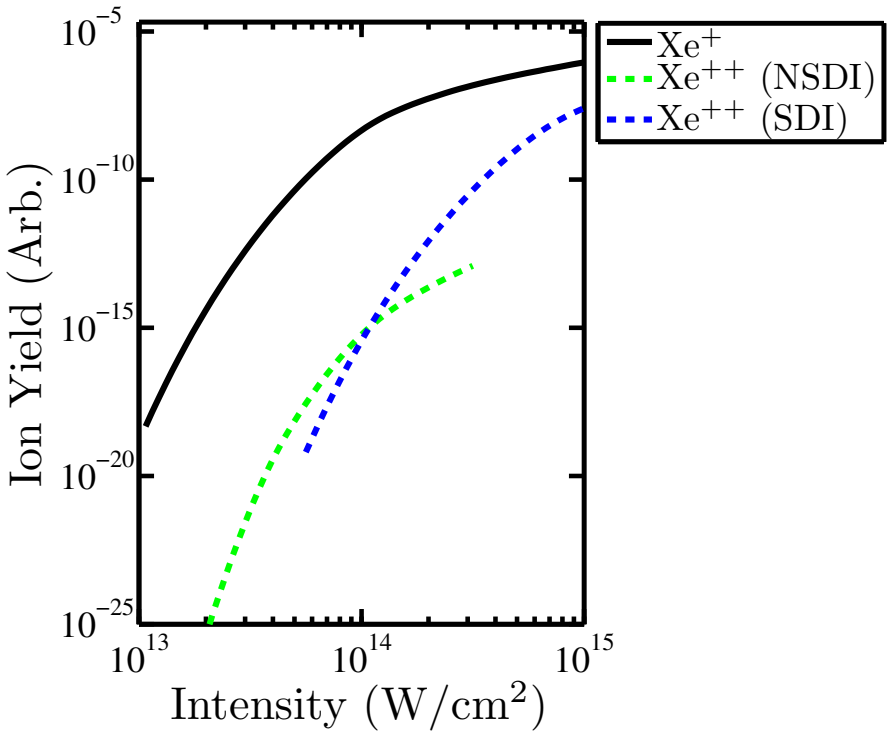

Figure 1.4: *ADK ion curves calculated with MATLAB for both Xe^+ and Xe^{++}, indicating contributions to the second charge state due to both sequential and non-sequential events.*

1.3.1 Sequential Double Ionization (SDI)

After some critical intensity, the neutral target atom will become ionized. Increasing the intensity further will not lead to a higher ion yield of the singly-ionized charge state; in reality, past this critical intensity, the single-ion yield will *decrease* with increasing intensity. The reasoning for this is as follows. Past the critical intensity, the single-ions in the target volume become saturated. Increasing the intensity further will cause the ions in the target volume to ionize again. This process is referred to as Sequential Double Ionization (SDI). This process may be repeated as soon as the second charge state becomes saturated. We can quantify this sequential ionization process by the following stepwise process:

$$A + n_1\hbar\omega \longrightarrow A^+ + e^-$$

$$A^+ + n_2\hbar\omega \longrightarrow A^{++} + e^-,$$

where n_1 and n_2 are the number of photons absorbed in each step. The rate at which an atom or molecule is sequentially ionized can be found by solving the following set of differential equations:

$$\begin{aligned}\frac{dN_0}{dt} &= -N_0 W_0 \\ \frac{dN_1}{dt} &= N_0 W_0 - N_1 W_1 \\ \frac{dN_2}{dt} &= N_2 W_1 - N_2 W_2,\end{aligned}$$

Where N_i represents the population of the i^{th} charge state, and W_i represents the corresponding ionization rate. These equations can be generalized as well,

$$\frac{dN_i}{dt} = N_{i-1} W_{i-1} - N_i W_i. \tag{1.7}$$

This allows one to evaluate the current charge state population from relative populations of the previous charge states in the SDI regime.

1.3.2 Non-sequential Double Ionization (NSDI)

Non-sequential double ionization was first reported in the early 1980's [17], and was first observed for the Xe^{++} [20]. Further studies of NDI have been carried out for noble gas atoms [21, 22] as well as molecules [23, 24]. A naive interpretation of the divergence of the SDI rates from experiment at low intensities can be interpreted as two electrons being ionized from a neutral atom "simultaneously," rather than sequentially. It was later determined that in fact there is a time delay between the ionization steps in the a typical NSDI process, occurring in accordance with the recollision model [25]. In the rescattering picture, an electron tunnels out into the continuum where it is driven back to the ion core by the oscillating electric field. The electron may recombine and induce high-harmonic generation, or scatter from the core. This scattering may occur elastically, in which the electron continues to be accelerated by the field, or inelastically, inducing simultaneous ionization.

An analogous model to the SDI rate can be introduced for the low-intensity region of the

experimental doubly-charged ion yield plots. In this scheme, a doubly-charged ion is created simultaneously from the neutral ground state,

$$A + n\hbar\omega \longrightarrow A^{++} + 2e^{-}.$$

We may write set of rate equations describing this process in the NSDI regime. However, in order to calculate the population for the second charge state directly populated from the number of neutrals, the new conditions must be taken into account in the rate equations:

$$\begin{aligned}
\frac{\mathrm{d}N_0}{\mathrm{d}t} &= -N_0 W_{01} \\
\frac{\mathrm{d}N_1}{\mathrm{d}t} &= N_0 W_{01} - N_1 W_{12} \\
\frac{\mathrm{d}N_2}{\mathrm{d}t} &= N_1 W_{12} - N_2 W_{23},
\end{aligned}$$

where the ionization rates are specific to the process it entails, *e.g.* W_{01} is the rate for the $A \rightarrow A^{+}$ transition, and so on. W_{23} signifies the total ionization rate to the final charge state.

[This page intentionally left blank]

Chapter 2

Summary of Current Theories

The fundamental nature of tunneling is of central importance in strong-field physics. A large amount of resources have been expended in an effort to gain a more accurate understanding of this process. Ionization models based on tunneling in atoms tend to be quite accurate in the tunneling regime; however, in more complicated systems, such as molecules, present a difficult problem to theorists.

In this chapter, we will discuss several current theories for the ionization rates of atoms and molecules. Each of these theories is put into historical context, accompanied by a brief overview of the model. All theories discussed in this chapter are based on the ionization rate derived for Hydrogen, extended for multi-electron atoms or molecules using the Single Active Electron (SAE) approximation. The SAE approximation considers ionization to be a pure one-electron process, in which the other electrons are treated as being static.

The first of these theories is tunnel ionization in the Hydrogen atom in its ground state subjected to an external field. The derivation of the ionization rates for Hydrogen was formally introduced by Landau [1], which served as the basis for many subsequent models. The first such model that came after this derivation was developed by Perelomov *et al.* [3], in which they considered ionization occurring in a time-dependent field, extended to Hydrogenic atoms. Ammosov *et al.* [4] extended this theory by considering the effect of an alternating electric field in the tunneling regime. Tong *et al.* [26] extended the ADK theory to account for the ionization of *molecules*, by appropriate modifications to the ionization rate to account for the non-spherical symmetry of molecules.

2.1 Ionization Rates and Yields

Ultimately, what we measure in the lab is a *signal*, whereas theory predicts a *rate*. The signal is obtained by integrating the rate over spatial and temporal coordinates. This demonstrates one of the main problems with comparing experiment to theory – comparing the experimentally determined *yields* with the theoretical *rate*. In particular, the measured signal is a convolution of the physical rate integrated over both space and time. This integral equation is difficult to de-convolute, as there are uncertainties in both the temporal integral as well as the spatial integral.

Nevertheless, we wish to link these quantities as closely as possible, which is needed in order to provide useful data which can be used to existing ionization models. Ultimately, we are interested in determining a closed-form analytic expression for the ion yield, or signal, of a particular species as a function of intensity. The first approximation we will employ is to assume a cylindrical geometry at the interaction region. This is done by appropriately choosing the dimensions of the gas jet such that at the region where the jet and the laser radiation coincide, the width of the jet is insignificant compared to any spatial variation of the laser beam (See Fig. 2.1). More criteria used to evaluate the reasonableness of utilizing cylindrical geometry is that the Rayleigh range needs to be larger than the width of the jet at the interaction region, *e.g.* $Z_{\mathrm{R}} \gg \ell$, where Z_{R} is the *Rayleigh range*, and is quantified by the Rayleigh Range, $Z_{\mathrm{R}} = \frac{\pi w_0^2}{\lambda}$. Qualitatively, the Rayleigh Range is the distance along the propagation direction of the beam, where the half-width at the narrowest point (the *minimum spot size*, w_0) increases by a factor of $\sqrt{2}$. By assuming that $Z_{\mathrm{R}} \gg \ell$, we can utilize cylindrical symmetry of the laser over the interaction region. The explicit derivation of the *rate equations* is included in Appendix A on pg. 137.

2.2 Theoretical Models for Ionization Rates of Atoms

2.2.1 Tunnel Ionization

The first derivation of tunnel ionization was first presented by Landau [1] using the semi-classical approximation in parabolic coordinates, and our derivation shown here follows his methodology. We start with the Time-Independent Schrödinger Equation (TISE) for a Hydrogen atom in a static

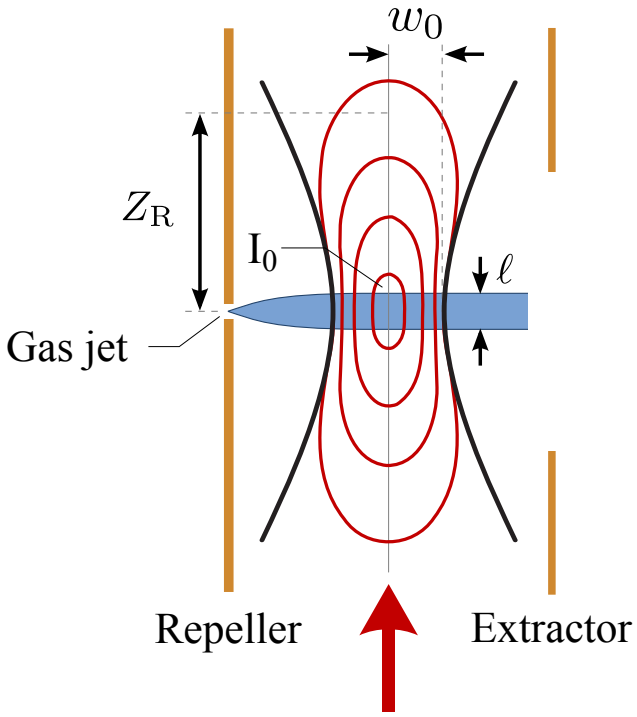

Figure 2.1: *Intensity variation of a focused beam over the width of the jet at the interaction region, ℓ. The divergence of the focused beam is quantified via the Rayleigh range, Z_R. The laser here is black, and the iso-intensity contours are shown in red, while the jet is blue.*

field,

$$\left(-\frac{\nabla^2}{2}+E+\frac{1}{r}+\mathscr{E}z\right)\psi(r,\theta,\phi)=0, \tag{2.1}$$

where ∇^2 is the spherical Laplacian, $\mathscr{E}$ is the electric field, and E represents the eigenenergies. For a Hydrogen atom in a spherically symmetric potential, evaluating the TISE is straightforward, as separation of variables is viable in this coordinate system. For a potential which does not contain spherical symmetry, such as what happens when a static field is applied, separation of variables is only possible in *parabolic coordinates*. We will proceed along this avenue; the connecting formulae allowing us to convert to this coordinate system are available in Table 2.1. Additionally, we require the parabolic Laplacian [27],

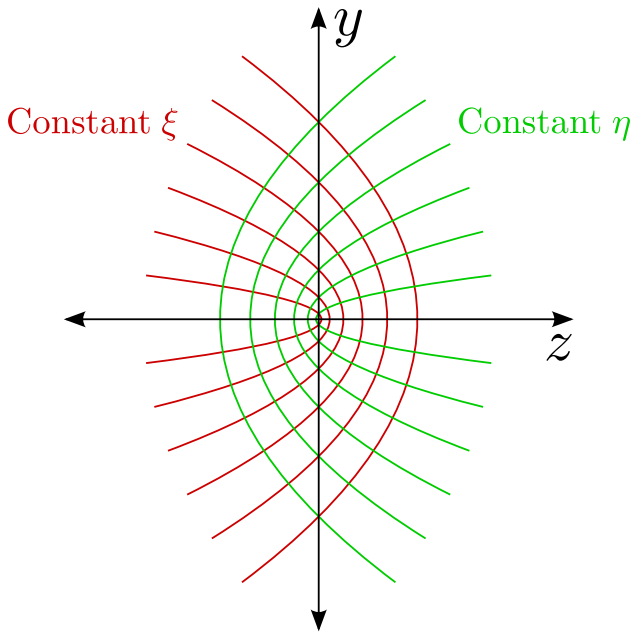

Figure 2.2: *The parabolic coordinate system. The coordinate surfaces for* η *and* ξ *are paraboloids, which are mirrored around the y-axis.*

$$\nabla^2 = \frac{4}{\xi+\eta}\left[\frac{\partial}{\partial\xi}\left(\xi\frac{\partial}{\partial\xi}\right)+\frac{\partial}{\partial\eta}\left(\eta\frac{\partial}{\partial\eta}\right)\right]+\frac{1}{\xi\eta}\frac{\partial^2}{\partial\phi^2}. \tag{2.2}$$

At this point, we wish to substitute the parabolic Laplacian operator from (2.2), as well as the appropriate connecting formulae from Table 2.1 into the TISE from (2.1):

$$\left\{\frac{2}{\xi+\eta}\left[\frac{\partial}{\partial\xi}\left(\xi\frac{\partial}{\partial\xi}\right)+\frac{\partial}{\partial\eta}\left(\eta\frac{\partial}{\partial\eta}\right)\right]+\frac{1}{\xi\eta}\frac{\partial^2}{\partial\phi^2}+E+\frac{2}{\xi+\eta}+\frac{\mathscr{E}}{2}(\xi-\eta)\right\}\psi(\xi,\eta,\phi)=0 \tag{2.3}$$

Table 2.1: *Connecting formulae for converting to parabolic coordinates.*

Parabolic → Cartesian	**Cartesian → Parabolic**
$x=\sqrt{\xi\eta}\cos\phi$	$\xi=r+z$
$y=\sqrt{\xi\eta}\sin\phi$	$\eta=r-z$
$z=(\xi-\eta)/2$	$\phi=\tan^{-1}(y/x)$
$r=(\xi+\eta)/2$	

It is possible to solve this partial differential equation via the method of separation of variables, similar to solving the TISE for the field-free Hydrogen atom in spherical coordinates. We assume that a separable solution exists in the following form:

$$\psi(\xi,\eta,\phi) = f_1(\xi)f_2(\eta)f_3(\phi), \tag{2.4}$$

where f_i represents the dependent variables, which are a function of the independent parabolic coordinate axes. This equation implies that $\psi(\xi,\eta,\phi)$ can be decomposed into three *separate* functions, which are *independent* of the others. This is the first step in solving partial differential equations based on the method of *separation of variables*. Simply by inspection, we can see that by substituting the separable solution from (2.4) into (2.3), that the ϕ-dependent terms can be separated from the remainder of the terms, precisely as what occurs in solving the TISE in *spherical* coordinates. The normalized solution of this elementary second-order differential equation can be easily found,

$$\frac{1}{f_3(\phi)}\frac{\mathrm{d}^2 f_3(\phi)}{\mathrm{d}\phi^2} = -m^2 \longrightarrow f_3(\phi) = \frac{e^{im\phi}}{\sqrt{2\pi}} \tag{2.5}$$

where we have chosen m^2 to be the separation constant, where m turns out to signify the *magnetic quantum number*. By including the solution for $f_3(\phi)$ from (2.5) into (2.4) and substituting the result into (2.3), we can separate the remaining variables. After simplification,

$$\left\{\frac{\partial}{\partial\xi}\left(\xi\frac{\partial}{\partial\xi}\right) + \left[\frac{E}{2}\xi - \frac{m^2}{4\xi} - \frac{\mathscr{E}}{4}\xi^2 + \beta_1\right]\right\} f_1(\xi) = 0 \tag{2.6a}$$

$$\left\{\frac{\partial}{\partial\eta}\left(\eta\frac{\partial}{\partial\eta}\right) + \left[\frac{E}{2}\eta - \frac{m^2}{4\eta} + \frac{\mathscr{E}}{4}\eta^2 + \beta_2\right]\right\} f_2(\eta) = 0 \tag{2.6b}$$

where β_1 and β_2 are the separation constants for (2.6a) and (2.6b), respectively, and are related to a total separation constant according to $\beta = \beta_1 + \beta_2 = 1$. We can rewrite (2.6a) and (2.6b) by making a change of variables, in the form of:

$$\rho_1(\xi) = \sqrt{\xi} f_1(\xi), \qquad \text{and} \quad \rho_2(\eta) = \sqrt{\eta} f_2(\eta)$$

Substituting ρ_1 and ρ_2 into (2.6a) and (2.6b), respectively, yields

$$\left\{\frac{\mathrm{d}^2}{\mathrm{d}\xi^2}+\left[\frac{E}{2}-\frac{m^2-1}{4\xi^2}-\frac{\mathscr{E}}{4}\xi+\frac{\beta_1}{\xi}\right]\right\}\rho_1(\xi)=0$$
$$\left\{\frac{\mathrm{d}^2}{\mathrm{d}\eta^2}+\left[\frac{E}{2}-\frac{m^2-1}{4\eta^2}+\frac{\mathscr{E}}{4}\eta+\frac{\beta_2}{\eta}\right]\right\}\rho_2(\eta)=0 \tag{2.7}$$

Our field is applied along the positive z-axis, and therefore the electron will be driven out opposite to this direction. This corresponds to a large value of η and a small value of ξ; therefore focus our attention towards find the solution for $\rho_2(\eta)$ in (2.7). Our goal in this section is to evaluate the tunneling ionization rate formula for Hydrogen in the ground state, and so we substitute the values $E=1/2$, $m=0$ and $\beta_2=1/2$ into (2.7),

$$\frac{\mathrm{d}^2\rho_2(\eta)}{\mathrm{d}\eta^2}+\left[\frac{1}{4}+\frac{1}{4\eta^2}+\frac{\mathscr{E}}{4}\eta+\frac{1}{2\eta}\right]\rho_2(\eta)=0. \tag{2.8}$$

We are now tasked with finding a solution for $\rho_2(\eta)$ from (2.8), and for this purpose we employ the semi-classical approximation. This approximation, also called the Wentzel-Kramers-Brillouin (WKB) approximation [28], is especially fruitful in obtaining approximate solutions to the TISE in one dimension [14]. In essence, applying the WKB approximation to a particle of energy E through a static potential $V(z)$ can be expressed in the form

$$\psi(z)=\exp\left[\pm ip(z)z\right], \qquad \text{where} \quad p(z)=\sqrt{2[E-V(z)]}$$

with $p(z)$ representing the classical momentum, which is real if $E>V$ and imaginary if $E<V$. We can apply this methodology to a Hydrogen atom in a static field, which we achieve by matching the wave function in the classical and non-classical regions. The classical wave function is simply the unperturbed eigenfunction of a Hydrogen atom in its ground state,

$$\psi(\xi,\eta)=\frac{1}{\sqrt{\pi}}\exp\left[-\frac{\xi+\eta}{2}\right]. \tag{2.9}$$

We wish to match this classical wave function to the non-classical form *inside* the effective potential barrier, which we denote as η_0. We match the standard WKB solution [14] to the classical solution

from (2.9) by using it as a boundary condition, in the sense that our final solution must reduce to (2.9) in the classical region. The final solution at the exit of the barrier takes the form [1],

$$\rho_2(\eta) = \sqrt{\frac{\eta_0 |p_0|}{\pi p(\eta)}} \exp\left[\frac{\xi + \eta_0}{2} + i\int_{\eta_0}^{\eta_1} p(\eta)\, d\eta + \frac{i\pi}{4}\right] \tag{2.10}$$

where $p(\eta)$ is the square root of the bracketed term in (2.8), and p_0 represents the η-root of $p(\eta) = 0$, where we find that since the electron is far away from the η direction ($\eta \gg 1$), that $|p_0| \simeq 1/2$. We can make a similar approximation for $p(\eta)$ by the following expansion,

$$p(\eta) = \frac{1}{2}\sqrt{\mathscr{E}\eta - 1} - \frac{1}{2\eta\sqrt{1 - \mathscr{E}\eta}} + \ldots \tag{2.11}$$

Substituting (2.11) into (2.10) and taking the modulus squared yields,

$$|\rho_2(\eta)|^2 = \frac{\eta_0}{\pi\sqrt{\mathscr{E}\eta - 1}} \exp\left[-\xi - \int_{\eta_0}^{\eta_1} \left(\sqrt{1 - \mathscr{E}\eta} + \frac{1}{\eta\sqrt{1 - \mathscr{E}\eta}} - \eta_0\right) d\eta\right], \tag{2.12}$$

where for $\eta_1 \simeq 1/\mathscr{E}$, while recognizing that $\mathscr{E}\eta_0 \ll 1$, (2.12) becomes

$$|\rho_2(\eta)|^2 = \frac{4}{\pi\mathscr{E}\sqrt{\mathscr{E}\eta - 1}} \exp\left[-\xi - \frac{2}{3\mathscr{E}}\right]. \tag{2.13}$$

The ionization rate is evaluated by calculating the current through an arbitrary surface perpendicular to the field direction. This is performed by integrating the current density, which is equivalent to the product of charge density ($|\psi|^2$) and the velocity of the electrons perpendicular to our surface (v_z):

$$w = 2\pi \int_0^{\infty} |\psi|^2 v_z\, \rho d\rho \tag{2.14}$$

where ρ in this context refers to the cylindrical radius of our perpendicularly-oriented surface, and the electron velocity perpendicular to this plane is $v_z \simeq \sqrt{\mathscr{E}\eta - 1}$, and we also note that $\xi = 0$, in accordance with our choice of coordinate origins. We can evaluate the rate from (2.14), which finally yields

$$\boxed{w = \frac{4}{\mathscr{E}} \exp\left[-\frac{2}{3\mathscr{E}}\right]}. \tag{2.15}$$

This simple result gives the ionization rate of Hydrogen atom in its ground state as a function of field strength. The result holds for field strengths $\mathscr{E} \ll 1$. We see in (2.15) that the ionization rate increases as $\mathscr{E}$ increases until the effective potential is suppressed below the binding energy of the electron, marking the onset of OTB ionization. OTB ionization was discussed in Chapter 1.2, and a cartoon indicating this process is shown in Fig. 1.2(c) on pg. 5.

The rate derived above is the basis for many other strong-field ionization theories. This method can be extended to handle the time-dependent fields and any atomic state by the methods of developed by Perelomov, Popov and Terent′ev in 1966 [3], which will be discussed in the next section.

2.2.2 Perelomov-Popov-Terent'ev (PPT)

While the tunneling approach applied to a ground-state Hydrogen atom in a static field is certainly enlightening, its applicability to more complicated systems is limited. One of the first corrections to tunnel ionization was introduced in 1966 and is now known as the Perelomov-Popov-Terent'ev (PPT) model [3]. In this seminal paper, they developed a model for calculating the ionization probability of an atom in the presence of an *alternating* electric field. One of the main difference between PPT and the tunneling theory presented by Landau is that the semi-classical solutions must accurately reflect the forces applied on the electron at the exit of the potential barrier, which are influenced by the presence of an alternating field.

One of the key assumptions used in this derivation is that the interaction between the ionized electron and the ionic core falls off at large distances more rapidly than $1/r$. We must define some key quantities, which will be used in this section:

$$\begin{aligned}
\mathscr{E}_0 &= \kappa^3 \Rightarrow (2I_\mathrm{p})^{3/2} \\
\omega_t &= \frac{\mathscr{E}}{\kappa} \Rightarrow \frac{2\mathscr{E}I_\mathrm{p}}{\mathscr{E}_0} \\
\gamma &= \frac{\omega}{\omega_t} \Rightarrow \frac{\omega\sqrt{2I_\mathrm{p}}}{\mathscr{E}} \\
\lambda &= \frac{Z}{\sqrt{2I_\mathrm{p}}}
\end{aligned}$$

where γ is the Keldysh parameter, and ω is the tunneling frequency. We now introduce a generalization of our static-field rate from (2.15) for a Hydrogenic atom in a static field with arbitrary quantum numbers [29]

$$w_{\text{stat}}(\mathscr{E}) = I_{\text{p}}|C_{m\ell}|^2 \frac{(2\ell+1)(\ell+|m|)!}{2^{|m|}(|m|)!(\ell-|m|)!}\left(\frac{2\mathscr{E}_0}{\mathscr{E}}\right)^{2\lambda-|m|-1}\exp\left[-\frac{2\mathscr{E}_0}{3\mathscr{E}}\right]. \tag{2.16}$$

We find the ionization rate of an atom in an alternating field in the tunneling limit ($\gamma \ll 1$) by averaging the ionization probability of the static field rate from (2.16) over the period of the laser field:

$$w(\mathscr{E},\omega) = \left(\frac{3\mathscr{E}}{\pi\mathscr{E}_0}\right)^{1/2} w_{\text{stat}}(\mathscr{E}). \tag{2.17}$$

This equation is valid for the case of an alternating field because in the tunneling limit, the frequency of the laser field is much less than the tunneling frequency in the adiabatic limit where $\gamma \ll 1$. In the multi-photon limit, where $\gamma \gg 1$, the rate can be calculated by introducing a time-dependent oscillation in the field, in the form $\mathscr{E}(t) = \mathscr{E}\cos\omega t$, which corresponds to the action of an alternating laser field. Furthermore, we can draw similar conclusions when $\gamma \gg 1$, where we recognize that the ionization probability is actually the *sum* of the individual probabilities associated with many-photon processes, where an integer number of photons are absorbed. Quantitatively [3],

$$w(\mathscr{E},\omega) = \sum_{n\geq\nu}^{\infty} w_n(\mathscr{E},\omega), \tag{2.18}$$

where ν is the minimum number of photons needed to bring the electron to continuum, and $w_n(\mathscr{E},\omega)$ is the ionization probability according to the absorption of n photons at a frequency of ω. When $\gamma \gg 1$, the summation from (2.18) reduces to the first term in the series, signifying that the ionization rate from $w_n(\mathscr{E},\omega)$ falls off rapidly with increasing values of n. The full PPT rate equation for a linearlly polarized field with arbitrary ℓ and m must incorporate the tunnelling limit solution from

(2.17) as well as the multi-photon limit from (2.18):

$$w_{\mathrm{PPT}}(\mathscr{E},\omega) = I_{\mathrm{p}}|C_{m\ell}|^2 \left(\frac{6}{\pi}\right)^{1/2} \frac{(2\ell_1)(\ell+|m|)!}{2^{|m|}(|m|)!(\ell-|m|)!} \times \left(\frac{\mathscr{E}\sqrt{1+\gamma^2}}{2\mathscr{E}_0}\right)^{|m|+3/2} A_m(\omega,\gamma)\exp\left[-\frac{2\mathscr{E}_0}{3\mathscr{E}}g(\gamma)\right], \tag{2.19}$$

where

$$\begin{aligned}
A_m(\omega,\gamma) =& \frac{4}{|m|!\sqrt{3\pi}}\frac{\gamma^2}{1+\gamma^2}\sum_{n\geq\nu}^{\infty} e^{-\alpha(n-\nu)} w_m\left(\sqrt{\beta(n-\nu)}\right) \\
w_m(x) =& \frac{x^{2|m|+1}}{2}\int_0^1 \frac{e^{-x^2 t}t^{|m|}}{(1-t)^{1/2}}\,\mathrm{d}t \\
\alpha(\gamma) =& 2\left[\sinh^{-1}\gamma - \frac{\gamma}{\sqrt{1+\gamma^2}}\right] = \begin{cases} 2\gamma^3/3 & \gamma \ll 1 \\ 2(\ln 2\gamma - 1) & \gamma \gg 1 \end{cases} \\
g(\gamma) =& \frac{3}{2\gamma}\left[\left(1+\frac{1}{2\gamma^2}\right)\sinh^{-1}\gamma - \frac{\sqrt{1+\gamma^2}}{2\gamma}\right] = \begin{cases} 1-\gamma^2/10+9\gamma^4/280 & \gamma \ll 1 \\ 3\gamma^{-1}/2(\ln 2\gamma - 1/2) & \gamma \gg 1 \end{cases} \\
\beta =& \frac{2\gamma}{\sqrt{1+\gamma^2}}.
\end{aligned}$$

Ammosov *et al.* [4] introduced an alternate rate similar to (2.19) in the case of complex atoms in an alternating field in the tunneling limit.

2.2.3 Ammosov-Delone-Krainov (ADK)

Ammosov *et al.* [4] simplified the PPT theory by deriving an approximate expression for the $C_{n^*\ell^*}$ terms. This was accomplished by joining the asymptotic wave function of the free electron with that of the classical radial wave function of the bound electron. This model has proven to be a valuable tool for the study of strong field atomic physics. The key point of ADK is that ionization occurs in such a short period of time compared to the optical period of the driving field, that it can can be regarded as quasi-static. In slowly varying fields, *e.g.* when $\gamma \ll 1$, ADK assumes that the field changes slowly enough such that the static tunneling rates can be calculated for each instantaneous

value of the applied field, and the final ADK rate being determined from the sum of all the static rates. An alteration occurs in the definition of the quantum numbers within the formalism of the ADK model; they introduce an effective principle quantum number and orbital quantum number n^* and ℓ^*, where $\ell^* = n_0^* - 1$, and n_0^* sis the effective principle quantum number for the lowest state. For linear polarization in the low-frequency limit, the ADK rate equation takes the form, [4, 26, 30]

$$w_{\mathrm{ADK}}(\mathscr{E},\omega) = \left(\frac{3}{2\pi}\right)^{3/2} \frac{(2\ell+1)(\ell+|m|)!}{2^{|m|}(|m|)!(\ell-|m|)!} \frac{Z^3}{3n^{*3}} \left(\frac{4\widetilde{e}}{n^{*2}-\ell^{*2}}\right)^{n^*} \times \left(\frac{n^*-\ell^*}{n^*+\ell^*}\right)^{\ell+1/2} \left(\frac{2Z^3}{n^{*3}\mathscr{E}}\right)^{2n^*-|m|-3/2} \exp\left[-\frac{2Z^3}{3n^{*3}\mathscr{E}}\right], \tag{2.20}$$

where $\widetilde{e}$ is Euler's constant [31]. We finally note that the ADK model follows some critical assumptions. Firstly, it assumes that only the initial and final atomic states are needed to describe the ionization rate, and different atoms are characterized only by their ionization potential and the effective quantum numbers involved in the transition in the weak-field limit. Accordingly, ADK implies that the details of the electronic structure are unimportant [9]. However, as we shall see in Chapter 4, this theory is not adequate in describing molecules having the same I_{p} as similar atomic systems.

2.3 Theoretical Models for Ionization Rates of Molecules

Two strong-field molecular ionization models will be discussed in this section: the molecular tunneling theory, and the molecular strong field approximation. Molecular ADK theory, often referred to as MO-ADK [26], claims that the rate of ionization for a molecule in an oscillating field may be determined from the time-averaged static rates. In essence, MO-ADK is an extension of the ADK tunneling theory, generalized to take into account the non-spherical symmetry of the molecular system. Like we saw for ADK, the limit of this approach depends critically on the value of the Keldysh paramter, γ, where the best convergence occurs in the tunneling regime ($\gamma \ll 1$). The molecular analogue to the Strong Field Approximation (SFA), often referred to as MO-SFA [11, 32], which are based on the Keldysh-Faisal-Reiss (KFR) model [33–35], and will be discussed

in §2.3.2. A qualitative comparison between MO-ADK and MO-SFA can be seen in Fig. 2.3.

2.3.1 Molecular ADK theory

In order to obtain the tunneling ionization rates for *molecules*, we follow a similar path as we did with the ADK rate formula, in that we must consider the electronic wave functions in the asymptotic region. In particular, the ADK model for atoms was derived for an electronic state that initially has a well-defined spherical harmonics. To employ analytical expressions for the ionization rates for molecules, one has to express the molecular electronic wave function in the asymptotic region in terms of summations of spherical harmonics in a one-center expansion [26].

The MO-ADK ionization rate of a linear diatomic molecule aligned at an angle θ with respect to the polarization of a slowly varying field is given by [26]

$$w_{\text{MO-ADK}}(\mathscr{E}) = \frac{B^2(m)}{2^{|m|}|m|!}\frac{1}{\kappa^{(2Z/\kappa)-1}}\left(\frac{2\kappa^3}{\mathscr{E}}\right)^{(2Z/\kappa)-|m|-1}\exp\left[-\frac{2\kappa^3}{3\mathscr{E}}\right] \tag{2.21}$$

where we have defined $\kappa = \sqrt{2I_p}$, Z to be the residual charge of the molecular system, and m as the projection of the angular momentum on the molecular axis of the HOMO [36]. The function $B(m)$ is defined as

$$B(m) = \sum_{\ell} C_\ell Q(\ell, m),$$

where $Q(\ell, m)$ is given by

$$Q(\ell, m) = (-1)^m \sqrt{\frac{(2\ell+1)(\ell+|m|)!}{2(\ell-|m|)!}}.$$

The structure parameter, C_ℓ are obtained by fitting the molecular wavefunction in the asymptotic region [37]. The structure parameters can be calculated in a number of different ways, for example by way of the multiple scattering method [38, 39]. Values for the structure parameters $C_{\ell m}$ are provided from various sources in the literature [26, 37, 39]. Some example values of C_ℓ are given in Table 2.2.

In this thesis, I will use MO-ADK as the benchmark theoretical model for molecular ionization.

Table 2.2: *Values for C_ℓ derived for MO-ADK [26] for the three molecules studied in this work.*

Species	C_0	C_1	C_2	C_3	C_4
N_2	2.02	-	0.78	-	0.04
CO	1.43	0.76	0.28	0.02	-
O_2	-	-	0.62	-	0.03

All theoretical data presented in our results in Chapter 4 have been provided by Anh-Thu Le, a renowned AMO theoretician working on the forefront of strong-field ionization [40–42].

2.3.2 Molecular Strong-Field Approximation (MO-SFA)

The molecular analogue to the Strong Field Approximation (SFA), often referred to as MO-SFA [11, 32], which are based on the historically named Keldysh-Faisal-Reiss (KFR) model. This model was originally investigated by Keldysh in 1964 [2], with further studies conducted by Faisal [34] and then by Reiss [35]. In essence, SFA is used to describe nonresonant multiphoton ionization of atoms. The molecular SFA is based on the S-matrix formulation, where one considers the transition from a field-free initial state to the Volkov final state [11].

While SFA has been extremely successful in predicting the total ionization yields [43–45], the applicability of this method is questionable, since formulations of this theory provide different results depending on the gauge used in the calculation. Two gauges used in this theory are the *length gauge*, and the *velocity gauge*. The MO-SFA-VG was developed by Muth-Böhm *et al.* in 2000 [32], while the principle investigators of the MO-SFA-LG formulation were Kjeldsen *et al.* in 2004 [36]. Each provide different expressions for the transition amplitudes between states, and currently, there is no reason to believe that one is more correct than the other [11].

Like other ionization theories, SFA relies on some key assumptions. First, it assumes that the initial bound tate of the electronic system is unaffected by the presence of the external field, and also that the continuum the continuum electron is not influenced by the binding potential of the core [46]. This is valid if the magnitude of the field is large enough to dominate the long-range Coulomb potential [47]. These two assumptions imply that SFA only considers the initial and final electronic states, and does not consider intermediate resonances that may occurr between these limits.

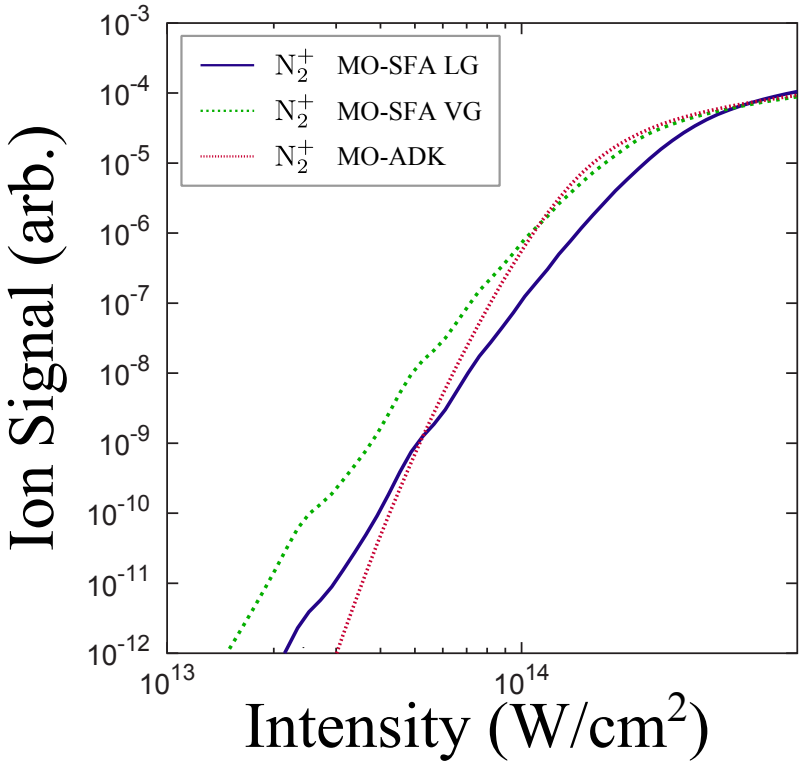

Figure 2.3: *Intensity-dependent yield plot for the single-electron ionization of N_2 with results from MO-SFA LG, MO-SFA VG, and MO-ADK using $\tau = 250$ fs and $w_0 = 98$ μm. Adapted from [11].*

In our experimental results in Chapter 4 on pg. 77, we have included some MO-SFA-LG results, which were adapted from the work provided by Kjeldsen *et al.* in 2005 [11] for comparison studies in the ionization rate of atoms and molecules through the strong field approximation. These results are presented in the ratios for each of the molecule/atom pairs we study in this work, however since they are calculated using parameters which do not reflect our experimental conditions, they are included as a reference only, and comparisons between this data and ours will not be made.

Chapter 3

Experimental Setup

Our experimental setup consists of three major components: The laser system which produces femtosecond laser pulses, our optical layout which modulates the intensity going into our chamber, and our experimental apparatus, which is a velocity-map-imaging time-of-flight mass spectrometer. The purpose of this chapter is to introduce these critical components, as well as to discuss the implications in our measurement system. Each of the critical components relevant to our research are addressed individually in the following sections.

3.1 Ultra-fast Laser System

Since the advent of the laser in 1960, scientists everywhere have embraced the new technology as an invaluable tool in the study of fundamental processes in the natural sciences. Lasers have been developed which are based on a myriad of different sources, such as dyes, gases and semiconductors. The laser system we use in this work is a *pulsed* laser, which allows us to probe transient subatomic processes.

The laser system used in this work is the Kansas Light Source (KLS), which provides an emission spectrum centered at 790 nm, and the temporal pulse width of 30 fs, at 2 mJ/pulse at a repetition rate of 2 kHz. A summary of the relevant statistics for this laser source is provided in Table 3.1. Our laser system consists of four major components: the oscillator, stretcher, amplifier, and the compressor. The latter three components constitute an amplification technique known as

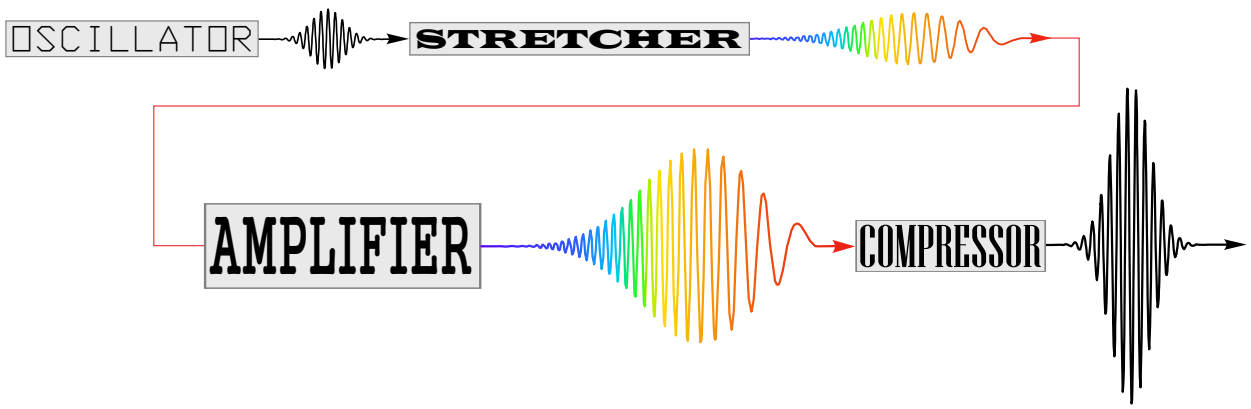

Figure 3.1: *The general working principle of the amplification of low-energy pulses is through Chirp Pulse Amplification.*

Chirped Pulse Amplification (CPA) [48, 49] - the general scheme behind this technique is shown in Fig. 3.1.

Without the use of the CPA technique, the results will be catastrophic, as demonstrated in the following scenario. During amplification, a circulating pulse travels through a gain medium a number of times before exits the cavity; every pass the pulse takes through the gain media its energy is increased. After a certain number of passes, the pulse will have a sufficiently high peak intensity to cause the optics to become damaged, stopping operation and ending the experiment. Chirped pulse amplification circumvents this issue by dispersing the energy spectrum *before* it enters the amplifier cavity. This way, amplification occurs for any given pulse over a longer period of time, which decreases the intensity according to $I_0 \sim \tau^{-1}$. If the intensity is decreased below the damage threshold for the optics, then the system is sustainable. After the pulse exits, the energy spectrum is collimated, yielding in a short, intense laser pulse. The dispersive element used in this argument before the amplifier is called the *stretcher*, and the collimating element is called the *compressor*. They are invaluable elements critical in the generation of femtosecond pulses.

3.1.1 Femtosecond Oscillator

The femtosecond laser pulse is born in the oscillator, in the heart of which lies a Titanium Sapphire (Ti:Sapph) crystal. Lasers based on this gain media are famed for the short intense pulses that they

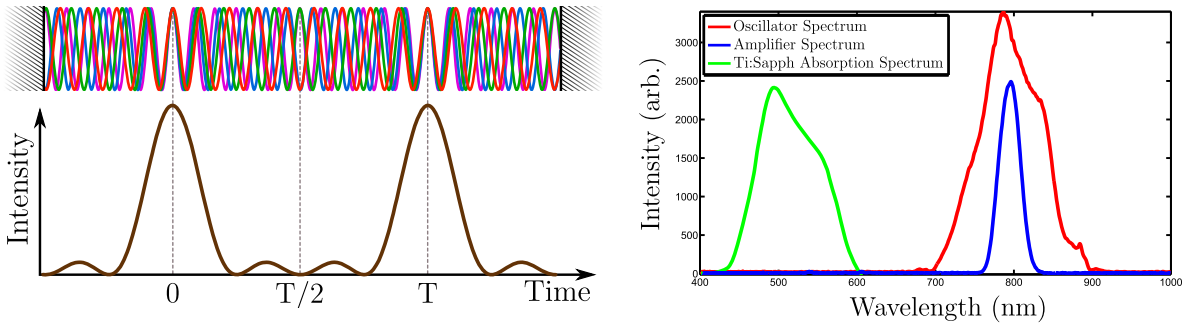

(a) Longitudinal modes in a resonant cavity

(b) Ti:Sapph absorption and emission spetra

Figure 3.2: *Kerr mode-locked Ti:Sapph oscillator working principle and emission spectra. (a) depicts the longitudinal modes within the cavity experience a cyclic phasing and dephasing. At both $t = 0$ and $t = T$, we see constructive interference of the allowed modes leading to the production of a train of pulses, separated by $t = T$. At $t = T/2$, the opposite behavior is observed – complete destructive interference leading to total attenuation of the signal. In (b) we see the absorption and emission spectra characteristic of a laser system utilizing a Ti:Sapph gain medium.*

are able to produce. The Ti:Sapph crystal, denoted as Ti^{3+}: Al_2O_3, is a Titanium-doped sapphire, where the Al^{3+} ions in the sapphire are replaced with Ti^{3+} ions. The Ti:Sapph crystal used in the KLS multi-pass amplifier is doped precisely at 0.25%. This crystal is pumped by a Nd-YAG laser [`Coherent Verdi DPSS`] which lases at 532 nm, which coincides with the absorption band of the Ti:Sapph gain media, as seen in Fig. 3.2(b). Population inversion is achieved Ti:Sapph as a gain media, and the electronic decay in the four-level system of Ti:Sapphs corresponds to emission centered around 790 nm. This produces a Continuous-Wave (CW) laser beam, however the oscillator can be made to work in pulsed operation by *mode-locking* the oscillator cavity. Mode-locking, or

Table 3.1: *Vital statistic for the oscillator and amplifier for KLS*

	Oscillator	**Amplifier**
Average Power	350 mW	4 W
Pulse Energy	5 nJ	2 mJ
Pulse Width	12 fs	30 fs
Repetition Rate	80 MHz	2 kHz
Central Wavelength	790 nm	790 nm
Bandwidth	95 nm	40 nm

phase-locking, refers to the process in which the oscillator operates in pulsed mode, rather than in its default CW state. This is achieved by *locking* the phases between the *modes* of different frequencies oscillating in the resonant laser cavity. When this happens, all the longitudinal modes are in phase with one another, constructively forming a periodic train of short pulses, as in Fig. 3.2(a). The time between the pulses is proportional to the amount of time it takes the pulse to circulate the cavity.

The limit to how short these pulses can be is proportional to the width of the gain profile, which determines the number of modes that the cavity can support. If a Ti:Sapph gain medium is used, then the gain bandwidth is very large, and the pulses can have a duration measured in fs (10^{-15} s). The absorption and emission spectra for the Ti:Sapph gain media can be seen in Fig. 3.2(b).

The mechanism of mode-locking can be explained as follows. The range of allowed frequencies in such a resonant cavity of a laser is determined by the frequency region over which the gain of the lasing medium exceeds the resonator loss. When this happens, amplification occurs, but only in these periods where the gain exceeds the loss. We can control when and how the gain exceeds the loss by introducing a discrimination which support the existence of pulses, and at the same time attenuate all other forms of operation. Put another way, the net gain should be positive at the peak of the pulse to allow for amplification, but both before and after the gain should be negative, suppressing the wings of the pulse, effectively shortening the pulse in time.

However, we find that many modes fulfill this condition automatically, and the total output depends on the relative frequencies, amplitudes and phases of all such modes. If there is nothing which fixes these quantities in relation to one another, then they will vary independently as a function of time, and the output from this system will evolve unpredictably. If, however, the modes are forced to maintain a fixed phase relationship and equal frequency spacing, then the output will behave in a well-defined manner. Upon fulfillment of this condition, the laser system is then said to be mode-locked.

In fact, the understanding of the conditions which are responsible for a laser operating in a pulsed regime rather than its natural continuous-wave (CW) state is a question of great interest [50–54]. At first, it was thought that mode-locking occurred spontaneously, and was sometimes referred to as “magic mode-locking,” since the mechanism responsible was not understood at the time [55–57]. Others found that mode-locking could be induced by tapping on a mirror mount in

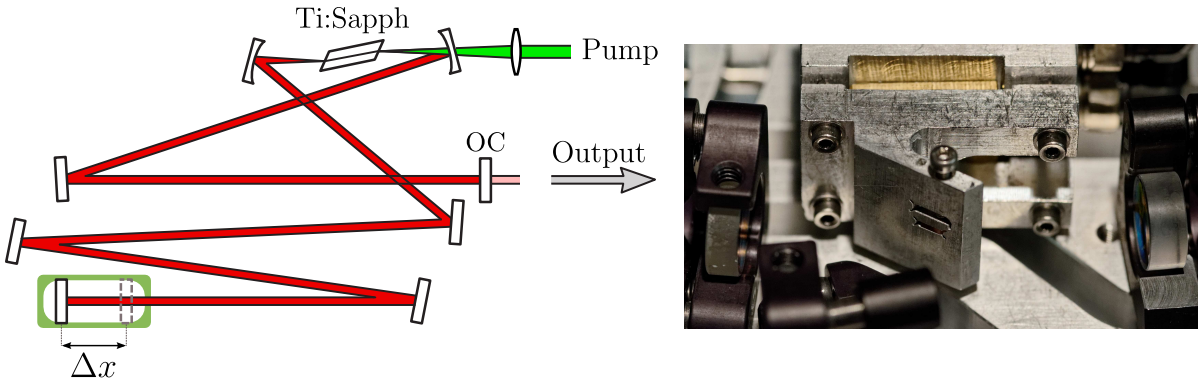

(a) KLS oscillator ray diagram

(b) Ti:Sapph crystal in KLS

Figure 3.3: *Oscillator cavity of KLS, where OC signifies the Output Coupler. (a) is the layout of major optical elements present in the oscillator which are responsible for pulse formation. The oscillator achieves mode-locking by displacing the end mirror by a distance Δx. (b) shows a photograph of the Ti:Sapph crystal at the same orientation as the corresponding elements in (a). The crystal is located inside the lower indentation in the crystal holder in (b), where the crystal itself is approximately the size of a single grain of rice.*

the resonator cavity, providing a "morning wake-up kick" [58, 59].

A CW laser system achieves mode-locking through the following procedure. We first recall that the saturable absorber (Kerr medium in a passively mode-locked system, as used in this work) acts to favor signal spikes, even if they are small. This bias acts to attenuate the CW modes in the cavity. Assuming that only a handful of modes oscillate in the CW regime, we only need to vary the cavity length *slightly*, perturbing the standing wave patterns of all current modes. In temporarily changing the cavity conditions, we inevitably reach a certain cavity length that will allow for the currently oscillating modes to constructively interfere, causing a slight increase in intensity. This intensity spikes is then favored by the action of the crystal. The pulses then recirculate the cavity, each trip they engulf more and more of the total circulating energy in the cavity, which further restricts the presence of CW modes. This is repeated until the most intense noise spike saturates the gain so much that all the other pulses circulating the cavity experience no net gain upon further recirculation. This leaves us with a single ultrashort pulse. A cartoon of the KLS oscillator can be seen in Fig. A.1(a), while a photograph of the Ti:Sapph crystal in our oscillator can be seen in Fig. A.1(b). A summary of the important parameters for our oscillator can be seen in Table 3.1.

In the process of controlling both gain and loss in a resonant cavity, extra care must be taken to

remove any elements within the laser cavity which are capable of discriminating the longitudinal modes unintentionally; the reason for this is because modes of different frequency may be amplified differently with respect to the frequency-dependent loss mechanism. For this reason, all transmissive optical elements within the laser cavity must be aligned to the *Brewster angle* to minimize losses due to reflection [54]. However, while the Ti:Sapph laser is famed for its ability to generate ultrashort pulses, the physical properties of the gain media make unintentional mode discrimination much more likely. The wide bandwidth of Ti:sapphire implies that the cavity must be carefully designed to allow each frequency to "see" the crystal at Brewster's angle. Without this consideration, a loss bias is introduced, inhibiting the formation of pulses in the cavity.

3.1.2 Stretcher

Before the pulse can be amplified, the energy spectrum must be dispersed; the device which serves this purpose is the stretcher [49]. In fact, the stretcher disperses the pulse in time, stretching the energy contained within the original pulse over a longer time period. This dispersion can be quantified by expanding the frequency-dependent phase around a central frequency ω_0 [60],

$$\Phi(\omega) = \varphi_0 + (\omega-\omega_0)\overbrace{\left(\frac{d\varphi(\omega)}{d\omega}\right)}^{\text{GDD}}_{\omega_0} + \frac{1}{2!}(\omega-\omega_0)^2\overbrace{\left(\frac{d^2\varphi(\omega)}{d_2\omega}\right)}^{\text{GVD}}_{\omega_0} + \cdots \tag{3.1}$$

where the first braced term in (3.1) represents the Group Delay Dispersion (GDD), while the second term is the Group Velocity Dispersion (GVD). The temporal broadening of a laser pulse due to GVD occurs because different frequency components of the pulse propagate with different velocities [61]. A value of GVD>0 indicates *positive* dispersion, whereas when GVD<0 there is *negative* dispersion. The GVD may be introduced after a pulse travels through a dispersive media as in Fig. 3.13 on pg. 46, or alternatively by a diffraction grating or a prism. Our laser system utilizes the former, since diffraction gratings disperse the frequencies by reflection, rather than transmission through an optical material which would introduce additional chirp. In a grating, chirp is achieved according to a well-characterized frequency-dependent angular separation, in which the diffracted light is dispersed along different angles proportional to the wavelength.

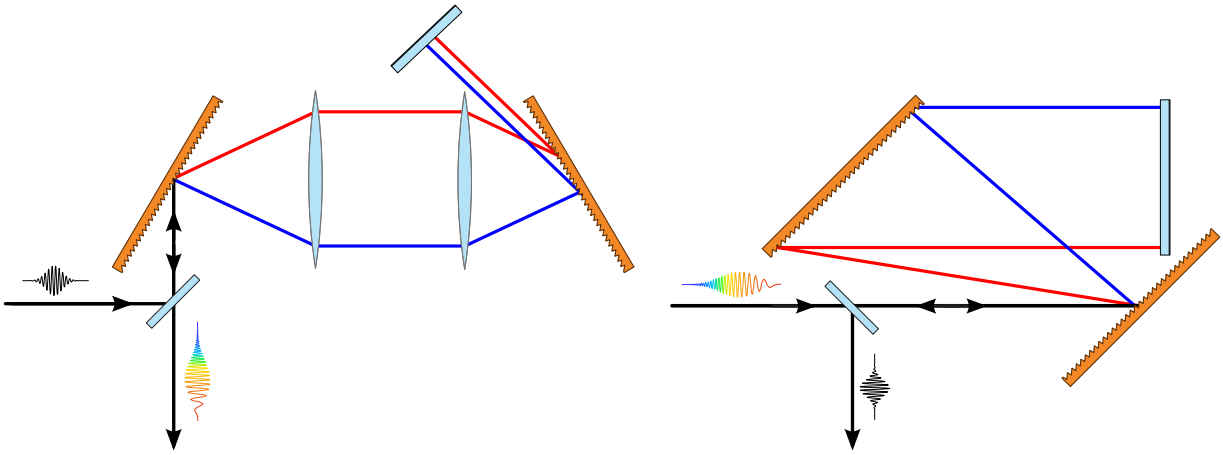

(a) Stretcher (b) Compressor

Figure 3.4: *Basic working principle of the stretcher and compressor used in the KLS amplifier. The stretcher creates positive dispersion, while the compressor provides negative dispersion.*

In fact, as see in Fig. 3.4(a)*, a pair of diffraction gratings is used. The first grating angularly disperses the beam, while the first of the two lenses is used to collimate the dispersed frequencies. The purpose of the second lens is to focus the spatially dispersed frequency components onto the plane of a flat mirror. Upon reflecting off this element, the frequency components then travel along the same path, and the result at the exit of the stretcher is that the frequencies are concatenated, red exiting first and blue last. This delay with respect to the red and blue frequencies creates *positive* dispersion, and it is what accounts for the stretching.

We recall from Table 3.1 that the original pulse duration is 12 fs. After the stretcher, the pulse duration is stretched to roughly $\sim$ 100 ps, a difference of nearly four orders of magnitude. In this way, the pulse energy is kept constant, while the pulse duration is increased, resulting in a lower peak intensity. Now that the pulse is dispersed, we may proceed with amplification.

*We remark that Fig. 3.4(a) is only a conceptual rendition of the action of a generic stretcher on a femtosecond pulse. The actual stretcher used in KLS uses curved mirrors, rather than lenses. This reduces the amount of uncontrollable dispersion introduced to the beam. A CAD drawing representing the current configuration of the KLS stretcher can be seen in Fig. 3.5.

3.1.3 Multi-pass Amplifier

The pulse energy prior to the amplification stage is measured in nJ; the purpose of the amplifier is to raise the pulse energy to the order of mJ - a difference of six orders of magnitude. This sort of gain cannot be achieved on a single pass through the gain media; therefore, the pulse circulates the laser cavity many times in order to achieve these high energies. However, the energy that can be extracted from the gain medium is finite, so that after a certain number of passes through the crystal, the pulse energy will not increase any further. This effect is called *Gain Saturation*, and in some cases it is most desirable to have the amplifier optimized to work near saturation. This way, most of the pump power is extracted from the Ti:Sapph crystal, while at the same time the saturation has a stabilizing effect on the final pulse energy.

There are two main types of amplifiers used in CPA laser systems: the *regenerative* amplifier, and the *multi-pass* amplifier. The basic working principles of both systems is similar; a pulse circulates the amplifier cavity, passing through the Ti:Sapph gain media multiple times before exiting. The difference between these two in how the number of passes through the crystal is controlled. In a multi-pass amplifier, such as the one used in KLS as in Fig. 3.5, the number of passes through the crystal is controlled by an accumulated misalignment that the pulse picks on each pass through the crystal. The pulse from the first pass is spatially separated from the pulse on the next pass and so on, until the pulse escapes from the amplifier cavity.

For a regenerative amplifier, there is no spatial separation between the beams on different passes through the cavity. The number of passes is controlled by a *Pockels cell*, which is used to switch out the pulse after it circulates a set number of times through the crystal. The Pockels cell is an electro-optic device, in that it can change the optical properties of the nonlinear crystal by applying an electrical signal. It does this by changing the polarization of the incoming beam by introducing a electronically-controlled retardation phase between the low and fast axes of the crystal. When a Pockels cell is used in tandem with a polarizing beam-splitter (PBS)[†], the pair can be considered to act as an electrically-induced optical switch. Inside the amplification cavity, the seed pulse from the oscillator is trapped until the switch is turned over, switching the pulse out of the cavity [63].

[†]The action of a polarizing beam-splitter on an initially unpolarized beam is depicted in Fig. 3.12.

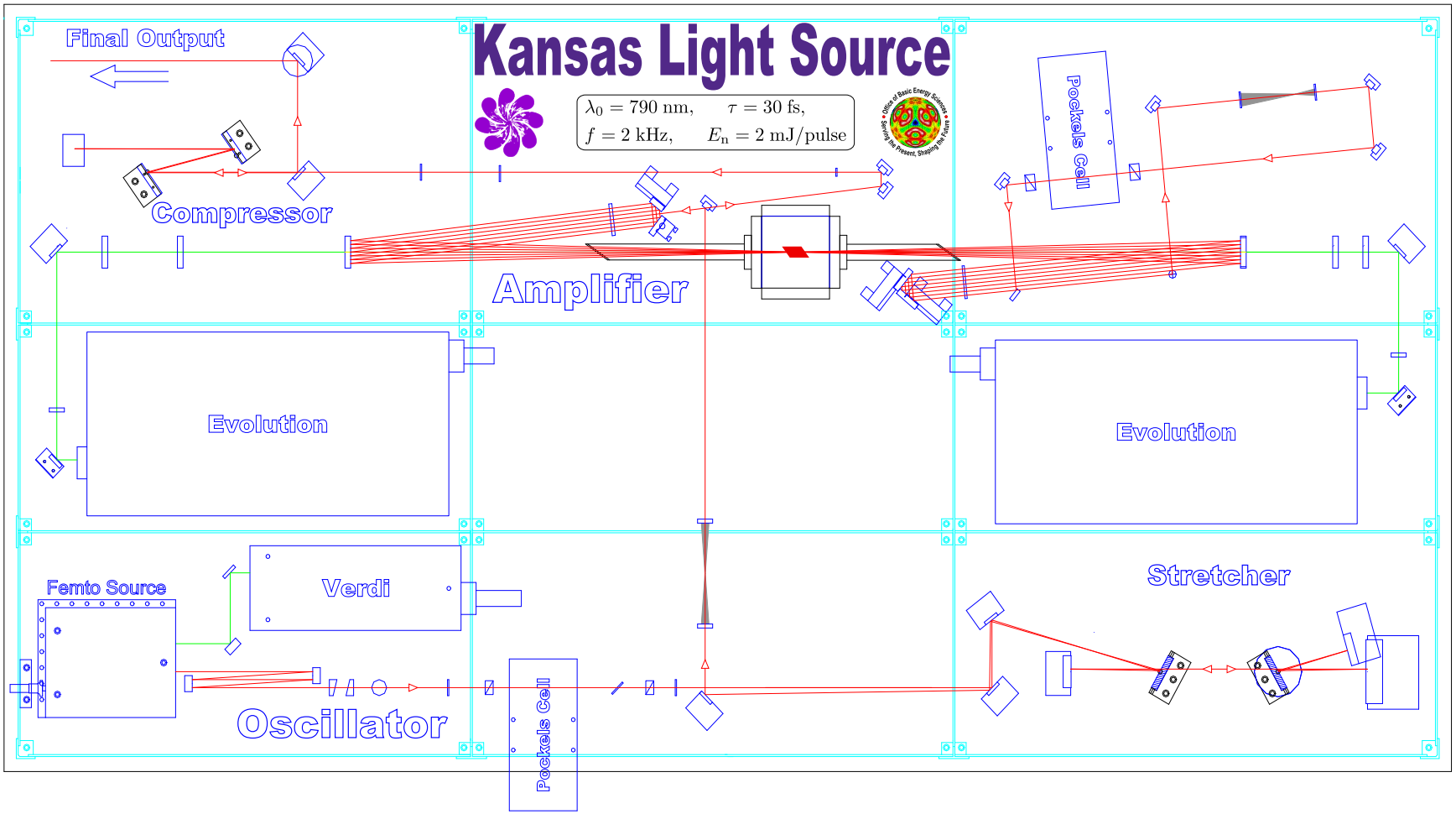

Figure 3.5: *The Kansas Light Source was an original design by Professor Zhengu Chang, who built the laser in 2001 in the JR. Macdonald Lab at Kansas State University. The unique multi-pass design was patented in 2006 by Chang* et al. *[62].*

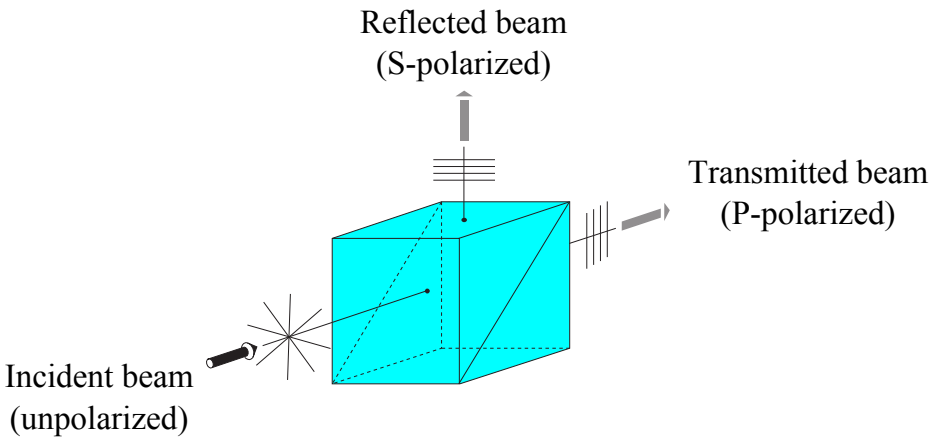

Figure 3.6: *The action of a polarizing beam-splitter on an initially unpolarized beam. The transmitted beam is vertically polarized according to the orientation shown.*

Both techniques have their advantages and disadvantages; the main advantage of the multi-pass design is that no extra dispersive materials are used in the cavity. This is preferred, since the presence of any additional dispersive elements will adversely affect the generation of short laser pulses by introducing extra dispersion to the pulse. However, due to the tight geometry required for a multi-pass amplifier, the number of passes is fixed, and this may result in a decreased conversion efficiency from the pump energy to the laser energy. On the other hand, in a regenerative amplifier the number of passes is electronically adjusted, so the optimal number of passes can be adjusted without making any changes to the beamline. A summary of the parameters achieved using the multi-pass amplifier KLS is listed in Table 3.1.

3.1.4 Compressor

Now that the pulse is amplified, the frequencies should be collimated in time so that there is no frequency-dependent delay with respect to each of the components by sending it to the compressor [48]. The compressor, as seen in Fig. 3.4(b), acts to remove the time delay between the different frequencies originally introduced by the stretcher. The compressor consists of two diffraction gratings, which are configured to impart a *negative* group velocity dispersion onto the pulse [64], canceling out the *positive* group velocity dispersion introduced by the stretcher. The final result is a high-energy, short pulse.

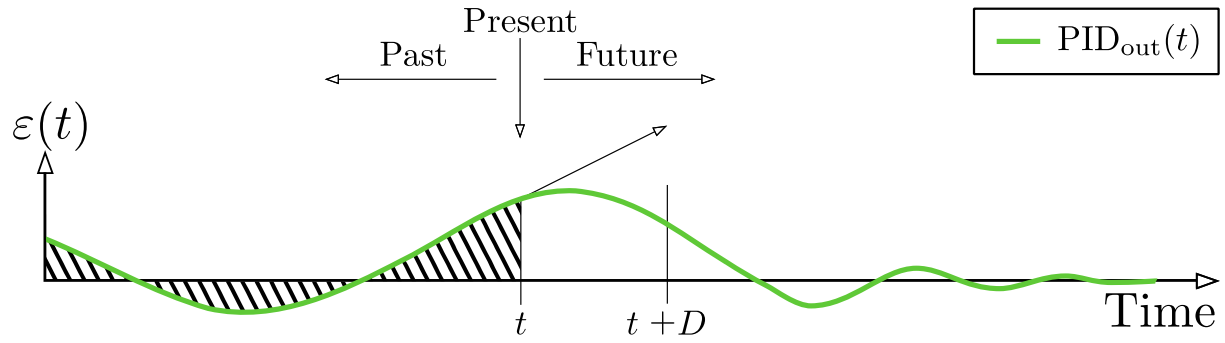

Figure 3.7: *The action of a PID controller on minimizing the error signal* $\varepsilon(t)$*, which is defined as the difference between the measured value and the set value. By considering the past fluctuations as well as the desired set point, the PID algorithm is able to respond to instantaneous time-varying fluctuations.*

3.2 Laser Control

In order to produce reliable data, it is crucial that the laser provides a reliable source of radiation to the experiment. Many factors work against this goal, in particular systematic errors produced from temperature fluctuations, mechanical vibrations as well as from electrical noise. This is often a difficult problem to solve, due to the vast number of individual contributions from so many sources inside the laser and the environment. However, certain measures can be taken to ensure a stable laser, in particular through power-locking.

3.2.1 Power-locking

power-locking refers to the process of *locking* the output *power* from the amplifier to a fixed value. This is achieved by using a closed loop feedback and control algorithm, which makes small adjustments in the laser cavity to compensate for a fluctuation in the final output. The device which performs this task is the Proportional-Integral-Derivative (PID) controller [`Stanford Research Systems SIM900`], which in essence acts like a thermostat, where temperature is analogous to the laser power. In this analogy, if the room becomes colder than a user-specified temperature value, then the thermostat will compensate by increasing the flux of heat going into the room. The PID loop in a power-locked amplifier acts the same way; if the power drops below a pre-set value, then

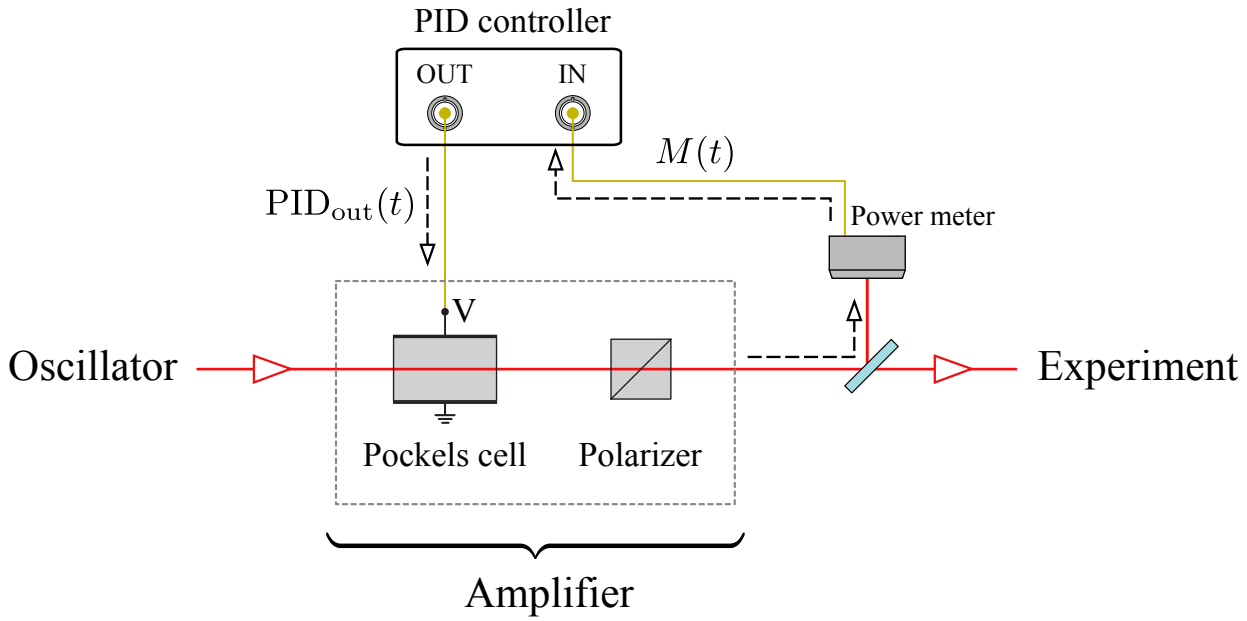

Figure 3.8: *A schematic illustration of how power-locking is implemented in our laser system. Power-locking is driven by a closed-loop feedback and control algorithm by way of a PID controller. The measured signal, $M(t)$, is read in from the output of the amplifier by a power meter; this value is then compared to a set power specified by the user, and sends an output signal, $PID_{out}(t)$, to the Pockels cell. This system allows for continuous adjustments to the laser power to compensate for instantaneous fluctuations in the laser power.*

the controller will increases the power to compensate. The mechanism which allows the controller to increase the power will be discussed below.

In reality, the PID controller is much more sophisticated than a thermostat - it works by calculating the error by taking the difference between a measured value and the desired setpoint. The controller attempts to minimize the value of this error by making adjustments that affect the measured value. Quantitatively, the output of a PID controller as a function of time can be expressed as [65],

$$\mathrm{PID_{out}}(t) = \overbrace{P\varepsilon(t)}^{\text{Present}} + \overbrace{I\int_0^t \varepsilon(\tau)\,\mathrm{d}\tau}^{\text{Past}} + \overbrace{D\frac{\mathrm{d}\varepsilon(t)}{\mathrm{d}t}}^{\text{Future}}, \qquad \text{where:} \quad \begin{aligned} &\varepsilon(t) = \mathrm{SP} - M(t) \\ &\mathrm{SP} - \text{Set point} \\ &M(t) - \text{Measured signal} \end{aligned}$$

where P is the proportional gain, I is the integral gain, and D is the derivative gain. The *present* time is expressed by t, while the variable of integration in the integral term is τ, signifying integrating

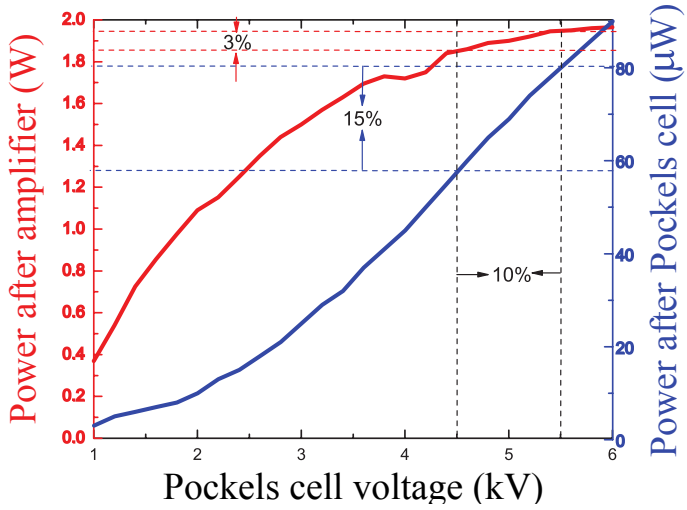

(a) Output power vs. voltage applied to the PC

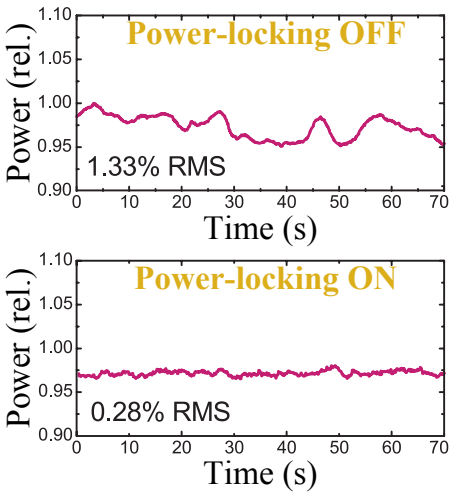

(b) The effect that power-locking has on KLS

Figure 3.9: *Data collected by Chang* et al. *on KLS for testing and optimizing power-locking. In (a), the output power as a function of voltage applied to the Pockels cell, which allows us to choose the working range of voltages sent to the PC from the PID controller. The effect that power-locking has on the output of a Ti:Sapph amplifier can be seen in (b), where we see the laser power fluctuating as a function of time when the PID controller is not engaged, while enabling it results in a much more stable laser. Adapted from [66].*

over the *past*. The quantity ε represents the error signal, which is the quantity that is minimized. A depiction of $\text{PID}_{\text{out}}(t)$ as a function of the error signal $\varepsilon(t)$ is shown in Fig. 3.7. A schematic illustration of this technique applied specifically to KLS can be seen in Fig. 3.8.

The PID controller modifies the measured value by way of changing the amplitude of the high voltage pulses applied to a Pockels cell in the amplifier cavity. In order to select a working voltage range for the PC, a series of measurements were taken of the laser output power versus the voltage applied to the electro-optic crystal in the PC. This data is shown in Fig. 3.9(a) was collected by Wang *et al.* on KLS in 2007 [66]. For an amplifier working in the *saturation regime*, they found that it is possible to make 10% voltage adjustments to compensate for a 3% power fluctuation.

This system is extremely effective in stabilizing the output power of KLS, as can be seen in Fig. 3.9(b). Without power-locking, the power fluctuation is 1.33%, whereas with power-locking engaged, this number falls to 0.28%. However, a caviat is that in order for this scheme to work, the setpoint for the output power must be less than the maximum output power. This ensures that the

PID controller has enough room to increase the power if the output falls below the expected value. Therefore, if an experiment requires the amplifier to work under full power, then power-locking cannot be used.

3.2.2 Power Selection & Discrimination

One of the central goals in this work is to provide data of sufficient quality to be used as a benchmark for existing molecular ionization models. One of the steps we took to meet this end was to restrict the influence of intensity fluctuations in our results by discarding erroneous data points, corresponding to large fluctuations in the laser power over time. We implemented this idea to our experiments as well as in the analysis. Prior to the chamber, 70% of the beam was dumped in the transmission through a beam-splitter which is sent into a power meter [`Newport 2935T-C/918D-SL-OD2`], which outputs an analogue signal, the magnitude of which is linearally proportional to the power read on the display of the unit. This analogue signal is connected to a data acquisition card [`Labjack U3-HV`], which connects to the computer running our acquisition software. Using this system, we are able to measure and record the instantaneous laser power at the time each data point is collected.

In the analysis stage, all the powers from all the data points collected in the scan are plotted as a function of instantaneous power, and a histogram is generated. The distribution is fit with a Gaussian function, which yields both the amplitude and standard deviation. Using a user-specified cutoff criteria, we can choose to disregard data points corresponding to instantaneous power fluctuations beyond this limit.

As an example of this methodology, we include apply this analysis to one of the scans used to produce the data in this work in Fig. 3.10. In this scan, a total of 484 points were collected over several hours, the fluctuations are centered around 13.7 mW. The fitted Gaussian distribution gives the standard deviation of the fluctuations, and here we choose that points only within $\pm 1\sigma$ of the centroid will be included in the final analysis. For this data set, we note that $\sigma = 0.13$ mW. The number of points that lie outside the valid interval are then rejected.

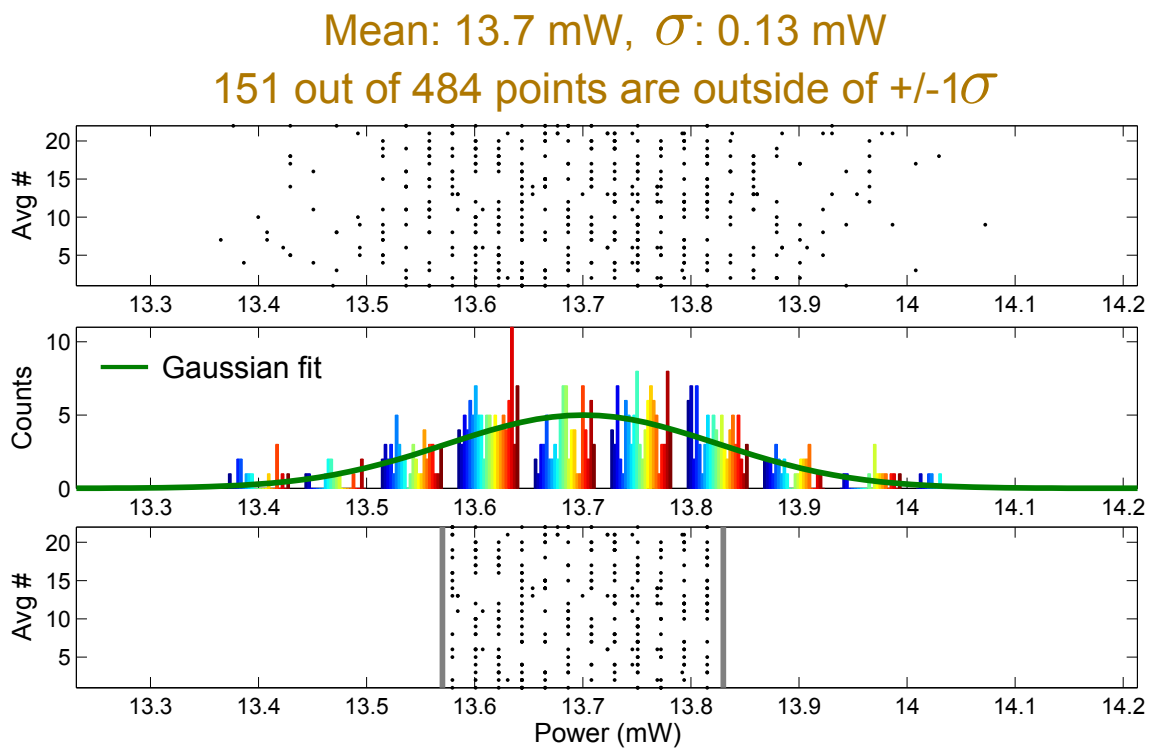

Figure 3.10: *The power discrimination scheme used in this work. The distribution of data points in the upper panel represents the spread of powers before the intensity control optics over an entire scan. The second panel is a histogram of all points, and the green curve is a Gaussian fit to the distribution. Using the criteria that we only want to select data points corresponding to a power deviating less than* ± 1 *standard deviation from the mean, we arrive at the final panel, which shows only the valid data points which will be included in the analysis. The vertical grey lines indicate the* $\pm 1\sigma$ *boundaries, where* σ *signifies the standard deviation.*

3.2.3 Intensity Control

As we are performing intensity-dependent studies on ionization yields, it is crucial that we have a scheme which allows for the continuous modulation of intensities. The method we chose involves using a Half-Wave Plate (HWP) [`CVI ACWP-700-1000-10-2`] mounted on a motorized rotational stage [`Micos DT-80`] followed by a Polarizing Beam-Splitter (PBS) [`Changchun Jiheng Optics 1″ FS-PBS`]. A CAD rendering of these elements as used in our experiment can be seen in Fig. 3.11. The HWP rotates the polarization of the incident beam by an angle θ, where our valid range of angles to be from θ_0 to θ_{max}, where θ_0 and θ_{max} indicate the minimum and maximum angles, respectively. The beam then passes through our PBS, which is oriented to only pass vertically

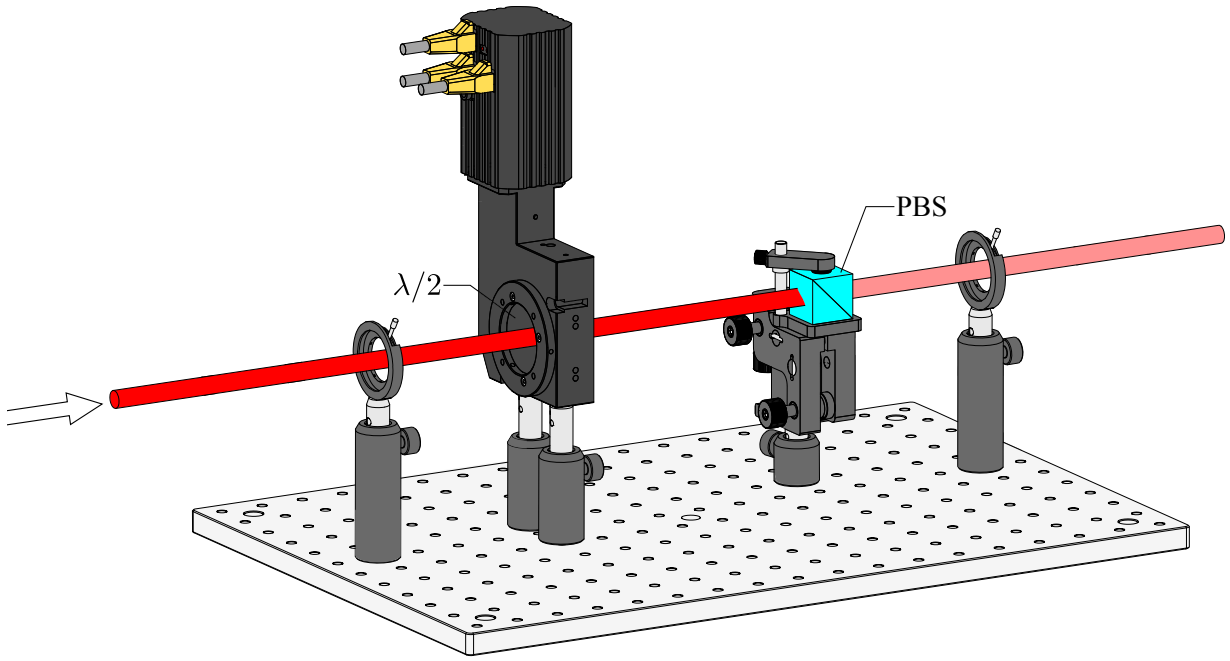

Figure 3.11: *Continuous intensity control system used in this work, with major components. The AR-coated half-wave plate is mounted in the motorized, LabVIEW controlled stage, which rotates the polarization of the incident beam, which is vertically polarized at the output of the amplifier. The resulting beam then passes through a polarizing beam-splitter, which is oriented to only allow the transmission of vertically polarized radiation. By rotating the HWP, we are therefore able to control the energy of the laser pulse entering our chamber.*

polarized radiation, as depicted in Fig. 3.12. As the polarization of our beam is vertical at the output of the amplifier, an angle of $\theta = 0^o$ therefore corresponds to *minimum* transmission through the polarizer. Conversely, *maximum* attenuation occurs when $\theta = 45^o$. This is quantified through Malus' Law [67, 68], which gives a proportionality between the transmission of a HWP-PBS pair as a function of the angle of the wave plate according to

$$I(\theta) = I_0 \sin^2(2\theta), \tag{3.2}$$

where I and I_0 are the transmitted and incident intensities, respectively, and θ signifies the angle of the HWP[‡]. The value of I_0 in (3.2) is to be presented in §3.3, and fully derived in Appendix B.

[‡]This is a special case of Malus' law, tailored to describe our intensity control system. Modifications include the use of sin instead of the standard cos, due to the fact that we wish $\theta = 0$ to correspond to the minimum transmission through the polarizer. We also included a factor of 2 in (3.2), reflecting the fact that our HWP-PBS pair are periodic over 180^o, rather than 360^o.

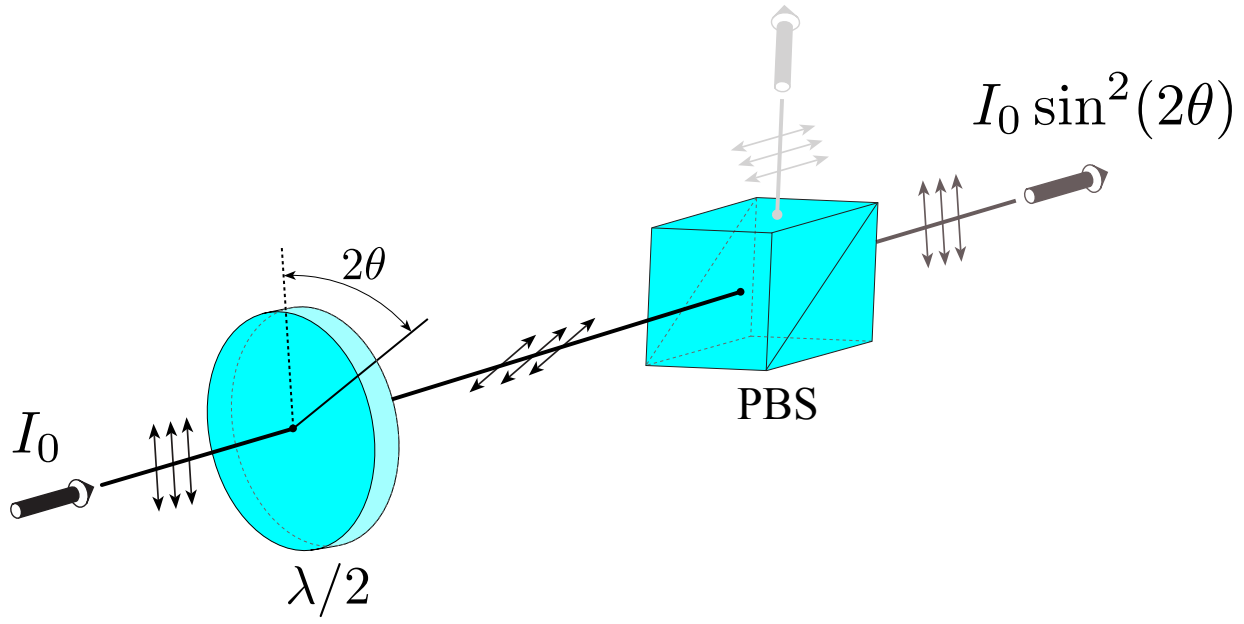

Figure 3.12: *The action of a half-wave plate followed by a polarizing beam-splitter is well-described by Malus' Law, where the intensity of the transmitted beam is proportional to* $I_0 \sin^2(2\theta)$*, where* θ *is the angle of the fast axis on the HWP. The transmitted beam after the HWP-PBS pair is vertically polarized according to the orientation shown.*

By using (3.2) above, as well as I_0 from (5.11) on pg. 115, we can map the angles on the HWP onto the corresponding intensity values. The stage for the HWP is controlled by our LabVIEW data-acquisition software, in which the intended intensity value corresponds to a specific angle sent to the wave plate. This technique allows us to have continuous intensity control without changing the alignment of the laser beam.

The polarizer we chose to fulfill this purpose is characterized by a large *extinction ratio*, which is defined as the ratio of the transmitted amplitudes of P to S polarization, respectively. Our PBS has an extinction ratio of $T_P : T_S > 1000$, which implies that it is able to separate the S and P polarizations effectively. A high extinction ratio is highly desirable for our purposes, as we have found that the polarization of the laser at the output of the amplifier is often not exactly vertical. The PBS acts to automatically attenuate the non-vertical components contained within the incident beam. This is important because the response of the target species at the interaction region is a sensitive function of the beam polarization [69]. However, a caveat to using this type of polarizer is

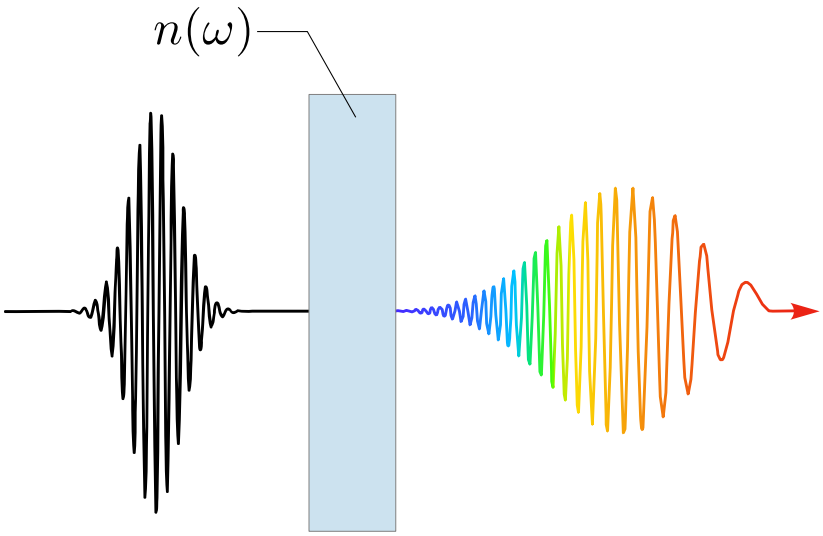

Figure 3.13: *A transform limited pulse passing through a dispersive medium becomes chirped, due to the frequency-dependent response of the material.*

the amount of dispersion introduced to the beam by passing through 1" of fused silica. However, we can correct for this dispersion by imparting a negative chirp at the stretcher, so that the pulse is transform-limited at the interaction region. This is discussed in more detail in the next section.

3.2.4 Dispersion Compensation

At the beginning of each data run, we take care to ensure that we have the shortest possible pulse at the interaction region. When this happens, the pulse is said to be Transform Limited (TL). An example of the field for a TL pulse can be seen in Fig. 3.14 for two pulse durations. A transform limited pulse is a pulse that is as short as the spectral bandwidth allows, corresponding to a minimum in the Time-Bandwidth Product (TBP), meaning that the peak power will be less than the maximum value. Within this context, the TBP is the product of the pulse duration and the spectral bandwidth. For a Gaussian pulse, this quantity is fixed at $\tau\Delta\omega = 0.441$. Any dispersion present in the laser pulse will increase the TBP from its minimum value, and manifest as a lengthening in pulse duration and a nonzero phase between the different modes. As an example, when an initially transform limited pulse passes through a transmissive medium, the exiting pulse is chirped, as depicted in Fig. 3.13.

Chirping occurs due to the transmissive medium having a frequency-dependent response $n(\omega)$,

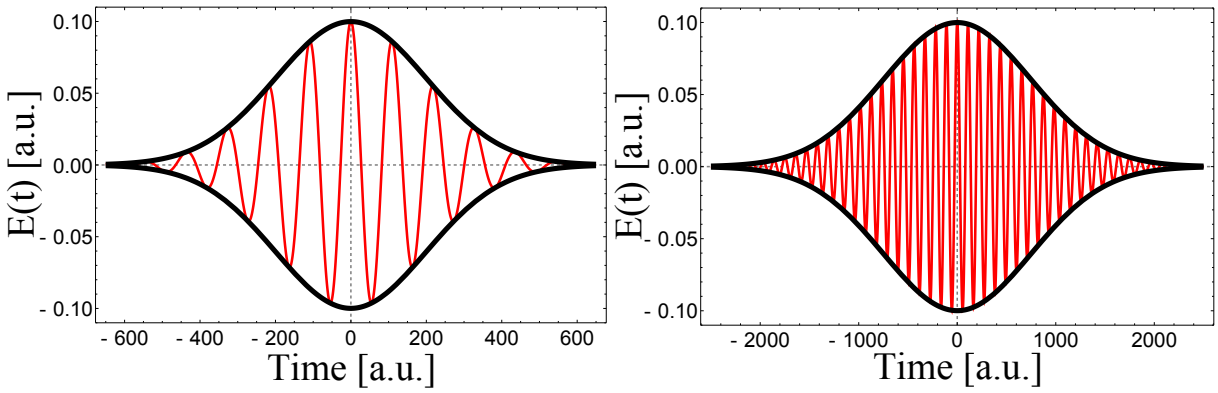

(a) Gaussian pulse with $\tau = 8$ fs

(b) Gaussian pulse with $\tau = 30$ fs

Figure 3.14: *Transform-limited Gaussian pulses calculated for a* 8 *fs pulse in (a), as well as for a* 30 *fs pulse in (b). Calculation performed in atomic units for a pulse centered around* $\lambda = 790$ *nm.*

which results in delay between frequencies due to the distribution of velocities inside the medium. This creates an offset in phase proportional to the frequency, resulting in a pulse having the same spectral bandwidth as it did before, but is stretched in time proportional to the delay between the slowest and fastest components. This is caused by the frequency dependence of the group velocity $v_g = \omega/k = c/n(\omega)$. The frequency-dependence of the group velocity is called the Group Velocity Dispersion (GVD), which is defined as the second order term in the expansion of the phase of the pulse.

Group velocity dispersion can be compensated for by changing the spacing between the diffraction gratings in the compressor by creating a *negatively* chirped pulse at the output of the amplifier, so that the pulse accumulates the exact amount of *positive* dispersion to result in a TL pulse at the interaction region. The compressor can only compensate for 2^{nd}-order dispersion; additional dispersion terms in the expansion from (3.1) may not be compensated for by this method. These higher-order dispersive terms may be introduced to the beam by the transmissive optical material in the line,

3.3 Intensity Calibration

The intensity of a Gaussian laser beam is quantified by

$$I(r,z,t) = I_0 \underbrace{\exp\left[-\frac{r^2}{w_0^2[1+(z/Z_\mathrm{R})^2]}\right]}_{\text{Space Part}} \times \underbrace{\exp\left[-\frac{4\ln 2\, t^2}{\tau^2}\right]}_{\text{Time Part}}, \tag{3.3}$$

where I_0 is the peak intensity, $w(z)$ is the e^{-2} beam waist, and τ is the FWHM pulse duration. We wish to derive a relationship between these quantities, which will allow us to calibrate the intensity. This equation will evaluate the intensity based on several independent measurements in the lab for the energy, pulse duration, and focal area. The full derivation of this equation is included in Appendix B on pg. 143, the main result is presented here,

$$I_0 = \frac{4E_\mathrm{n}}{\pi w_0^2 \tau}\sqrt{\frac{\ln 2}{\pi}}, \tag{3.4}$$

in which E_n is the pulse energy, w_0 is the minimum e^{-2} waist size of the beam, and τ is the FWHM pulse duration. We can substitute (5.11) into (3.3),

$$I(r,z,t) = \frac{4E_\mathrm{n}}{\pi w_0^2 \tau}\sqrt{\frac{\ln 2}{\pi}} \times \exp\left[-\frac{r^2}{w_0^2[1+(z/Z_\mathrm{R})^2]} - \frac{4\ln 2\, t^2}{\tau^2}\right], \tag{3.5}$$

where we recall that Z_R is the Rayleigh range, in which $Z_\mathrm{R} = \frac{\pi w_0^2}{\lambda}$. We can further tailor our result from (3.5) to our experiment by incorporating the explicit θ-dependence of the pulse energy on the angle of the HWP from §3.2.3,

$$I(r,z,t) = \frac{4TP_\mathrm{avg}}{\pi w_0^2 \tau}\sqrt{\frac{\ln 2}{\pi}} \times \sin^2(2\theta) \times \exp\left[-\frac{r^2}{w_0^2[1+(z/Z_\mathrm{R})^2]} - \frac{4\ln 2\, t^2}{\tau^2}\right], \tag{3.6}$$

where T is the repetition period of the laser, P_avg is the average power, and θ is the angle of the HWP. We see from (3.6) that there are three parameters which must be measured precisely: The energy, pulse duration, and beam waist. The measurement of each of these quantities will be discussed individually in the following sections.

3.3.1 Measuring the Pulse Energy E_{n}

The pulse energy is measured using a thermal power meter [`Coherent FieldMate/PowerMax PM30`], which provides a time-averaged power. Dividing this quantity by the known repetition rate of the laser allows us to find the pulse energy: $E_{\mathrm{n}} = P_{\mathrm{avg}}/T$. This assumes that the energy emitted between pulses is negligible, *i.e.* the excess Amplified Stimulated Emission (ASE) is suppressed. Excess ASE presents in Ti:Sapph amplifiers by producing incoherent radiation which competes with coherent radiative transitions [70]. This has the effect of creating "useless power," in the sense that ASE photons are not emitted in phase with the normally radiated photon. As power meters measure the *average* power over long times, the timing of the photons is undescernable; the temporal resolution of power meters is fundamentally limited by the response time of the material element, which is significantly slower than the repetition times of the pulse. In a multi-pass amplifier, we approximate that the contribution of ASE in the total measured power is < 5 % [71, 72].

3.3.2 Measuring the Minimum Beam Waist w_0

The minimum beam waist is determined by imaging the minimum focal area on a CMOS camera [`Mightex SME-B050-U`]. The camera is placed on a motorized translational stage [`Micos LS-65`], which was scanned through the focus, taking in image of the transverse beam at each step. This scheme is depicted in a ZEMAX simulation of our measuring apparatus in Fig. 3.15.

The set of images taken by the camera are then analyzed, where the radius can be measured directly. Due to the small focal area of focused lasers, the beam often only registers a handful of pixels on the sensor. For example, if the length of any sensor pixel size is 5 μm across and if six pixels are illuminated with a precision of ± 1 pixel, then the beam diameter is $30\,\mu\mathrm{m} \pm 5\,\mu\mathrm{m}$. This signifies a significant uncertainty in intensity. We circumvent these uncertainties by quantifying the beam propagation over long distances, typically measured in millimeters; a precision easily reached with motorized translational stages. From a theoretical point of view, the divergence of the beam as a function of position along the propagation direction can be quantified as

$$w(z) = w_0\sqrt{1+\left(\frac{z}{Z_{\mathrm{R}}}\right)^2}, \qquad \text{where} \quad Z_{\mathrm{R}} = \frac{\pi w_0^2}{\lambda}, \tag{3.7}$$

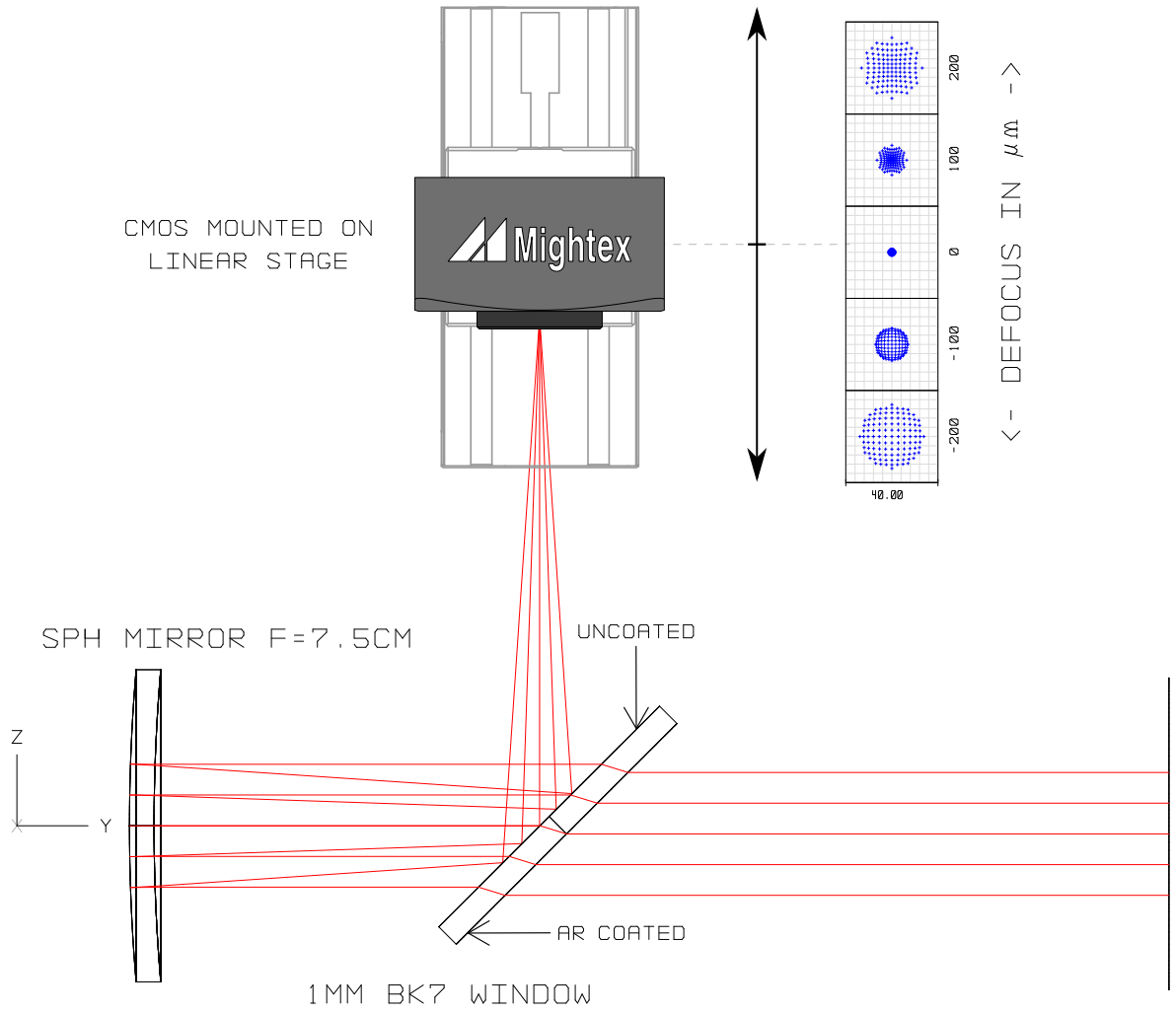

Figure 3.15: *ZEMAX simulation of our spot size experiment. The beam enters the apparatus from the right, where it passes through a thin window and hits a concave spherical mirror. The returned beam is reflected off the window, where it is focused onto a CMOS camera mounted on a motorized linear translational stage. The stage moves through the focus and takes images at each step, which will be analyzed using our LabVIEW program.*

where w_0 is the minimum beam waist, λ is the wavelength, and Z_R is the Rayleigh range, while z is the propagation axis. For our measurement, each position of the motorized stage is a step in the z-direction, while the beam waist is the width of the beam profile from the image on the camera. The functional form of the beam divergence, $w(z)$, is found by fitting the distributed experimental data points to the function from (3.7). The minimum of *this* distribution is taken as the minimum waist radius, w_0. This scheme is well explained by our analysis program in Fig. 5.13 on pg. 120 of

this document.

This value was procured for our experimental arrangement, the result was an astigmatic beam, having different waist size along the major and minor axes: $w_{0x} = 12.2\,\mu$m, and $w_{0y} = 11.2\,\mu$m. Given that we have an astigmatic beam, we may appropriately modify our intensity calibration equation from (5.11) to accommodate this abnormality,

$$I_0 = \frac{4E_{\mathrm{n}}}{\pi(w_{0x}w_{0y})\tau}\sqrt{\frac{\ln 2}{\pi}}. \tag{3.8}$$

The experiment that produced w_{0x} and w_{0y} is presented in detail in §5.2 on pg. 115.

3.3.3 Measuring the Pulse Duration τ

The pulse duration is measured using a Second Harmonic Frequency-Resolved Optical Gating (SH-FROG) autocorrelator [73–75]. The SH-FROG works by splitting the incident beam and recombining them on a nonlinear media, in our case a Barium Borate crystal (BBO). The resultant second harmonic signal is separated from the two initial beams, and sent into a spectrometer. The FROG algorithm [76] retrieves the temporal properties of the beam by completing a multitude of iterations. The primary result from this procedure is the temporal width of the pulse, τ, measured as a FWHM, which can be used in (3.8).

In a typical FROG, the incident laser pulse is split into two beams, where one is delayed in time with respect to the other. The experimental arrangement of the FROG used for our measurement can be seen in Fig. 3.16. The two beams are crossed at the BBO crystal, the time delay changing as a function of position along the BBO, which is measured using an imaging spectrometer. The resultant frequency-resolved signal produces a two-dimensional FROG trace, where the two axes represent the time delay and wavelength, respectively. Using an advanced retrieval algorithms, it is possible to reconstruct the pulse shape and phase from this trace: $\mathrm{G}(t+\tau) = \mathscr{E}(t+\tau)$. The second

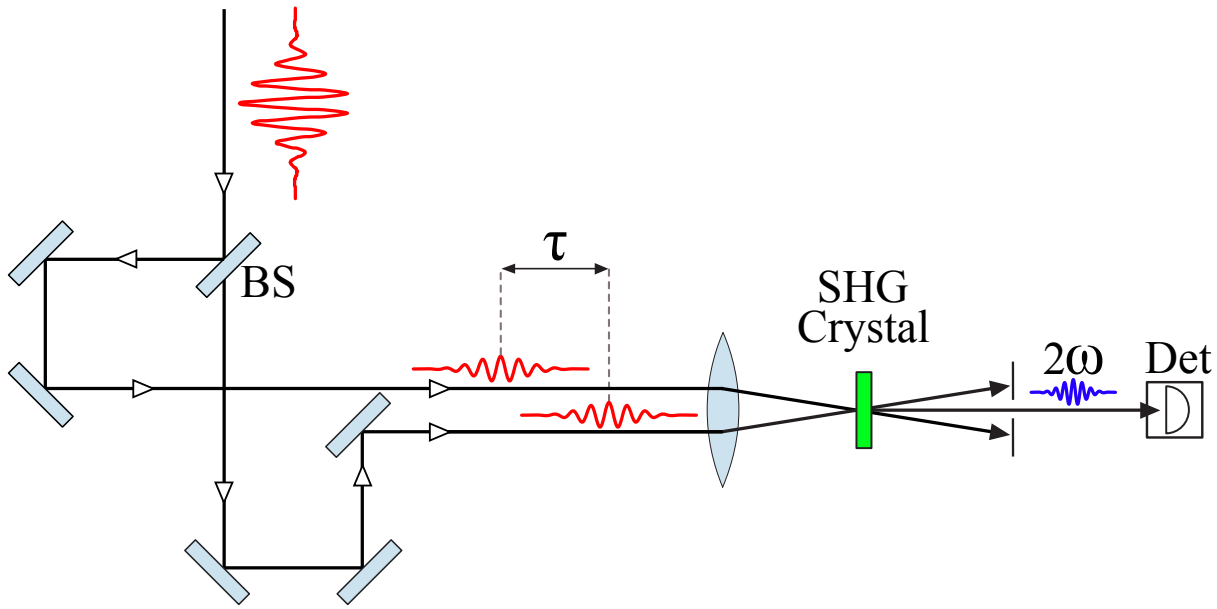

Figure 3.16: *Experimental arrangement for the Frequency Resolved Optical Gating Technique [73]. The beam to be measured is split into two arms, where the time delay between the two pulses* τ *is proportional to the path difference between the different paths each pulse takes. The beams are focused onto a BBO crystal, which generates the second harmonic signal* 2ω*, which is sent into the detector.*

harmonic signal can be expressed as [73]

$$\begin{aligned} S(\omega,\tau) &= \left| \int_{-\infty}^{\infty} \mathscr{E}(t) G(t+\tau) e^{-i\omega t}\, \mathrm{d}t \right|^2 \\ &= \left| \int_{-\infty}^{\infty} E(t) e^{i\phi(t)} \mathscr{E}(t+\tau) e^{-i(\omega-\omega_0)}\, \mathrm{d}t \right|^2, \end{aligned} \tag{3.9}$$

where $\mathscr{E}(t) = E(t)e^{i\phi(t)}e^{i\omega_0 t}$ is the complex laser field that is measured, $E(t)$ is the field envelope, $\phi(t)$ is the temporal phase, and $G(t)$ is the gating function, which equals $\mathscr{E}(t)$ for autocorrelation measurements. The fact that (3.9) is taken as the mod squared reflects the fact that the imaging spectrometer measured *intensity*, which behaves like $I \sim |\mathscr{E}|^2$. The retrieval algorithm works by first making an initial guess for $\mathscr{E}(t)$ to generate a trace from (3.9). During each iteration, the value of $S(\omega,\tau)$ is replaced by the square root of the experimentally measured FROG trace. On the next iteration, the algorithm guesses the amplitude and phase of $\mathscr{E}(t)$ by minimizing the difference between the measured and calculated trace. The program continues until the error is reduced to an

acceptable value [77].

Our pulse duration measurement was performed by placing our optical components from Fig. 3.11 before the FROG. The retrieval algorithm determined that the pulse duration was $\tau = 30$ fs, with a constant phase.

3.4 Detection System

The detection system used in this work is a Velocity Map Imaging (VMI) spectrometer operated in Time-Of-Flight (TOF) mode[§]. This technique is very powerful, and it serves as an invaluable tool in the study of atoms and molecules in strong laser fields [78–80]. The general working principle of our VMI-TOFMS is presented in Fig. 3.17, where we see that it creates an electric field at the interaction region which accelerates newly-created ions towards the detector. Each ion will be accelerated by the field to a certain velocity, the value of which depends on the accelerating voltage provided by the spectrometer, the initial kinetic energy of the ion, as well as its mass and charge of the ion. The interaction between the charged ion and the field produced by the spectrometer is well explained by Newtonian physics, under the assumption that the ions are non-relativistic. This can be quantified by $\mathbf{F} = q\mathbf{E}$ as well as Newton's 2$^{\text{nd}}$ law $\mathbf{F} = m\mathbf{a}$, where $\mathbf{F}$ is the force, $\mathbf{a}$ is the acceleration, and $\mathbf{E}$ is the electric field [81]. A quantitative analysis of time-of-flight mass spectroscopy is presented in the next section.

The measured quantity from our VMI-TOFMS is a TOF trace, which consists of all the ion peaks registered at the detector. The zero-time is measured using a photodiode at the entrance to our chamber; the time that it takes the particle to reach the detector is specific to the experimental apparatus used as well as the voltages applied to the spectrometer. Furthermore, since the geometry of the spectrometer is known, it is possible to extrapolate critical information about the ion created at the interaction region.

In this section, we will discuss all topics relevant to the apparatus used in this work. The general working principle behind our apparatus is first presented, followed by details specific to the design

[§]Combining the two acronyms, we often refer to our apparatus as a Velocity Map Imaging Time-Of-Flight Mass Spectrometer (VMI-TOFMS).

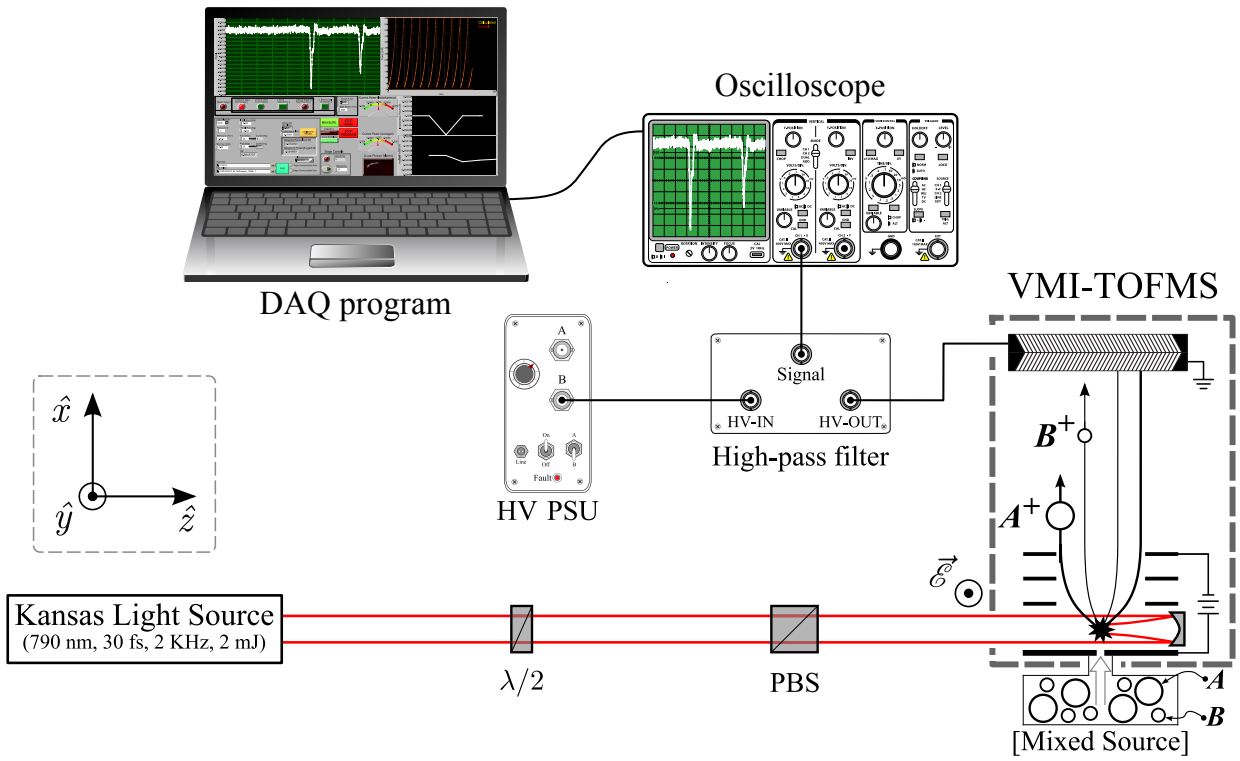

Figure 3.17: *The general principle behind the ion detection scheme for our apparatus is demonstrated using the generic species "A" and "B," where $m_A > m_B$. The polarizer is oriented to only pass vertically polarized radiation, and the half-wave plate is mounted on a DAQ-controlled motorized rotational stage. The half-wave plate/polarizer pair allows for continuous intensity control.*

used in our device. In addition, we will go over the alignment and optimization procedure applied to this device, both from a theoretical and a practical point of view.

3.4.1 Overview of Time-Of-Flight Mass Spectroscopy (TOFMS)

The purpose of the apparatus is to create a separation between different ions in time, so that they can be investigated individually. The interaction region, where the laser beam interacts with the neutral target atoms, is located between the repeller and the first extraction plate, as in Fig. 3.17. The gas is introduced to the interaction region by way of an effusive gas jet, located at the center of the repeller. The neutral molecules expand into the vacuum, and after some distance the perpendicularly oriented laser beam interacts with the distribution of neutral species, producing ions which are

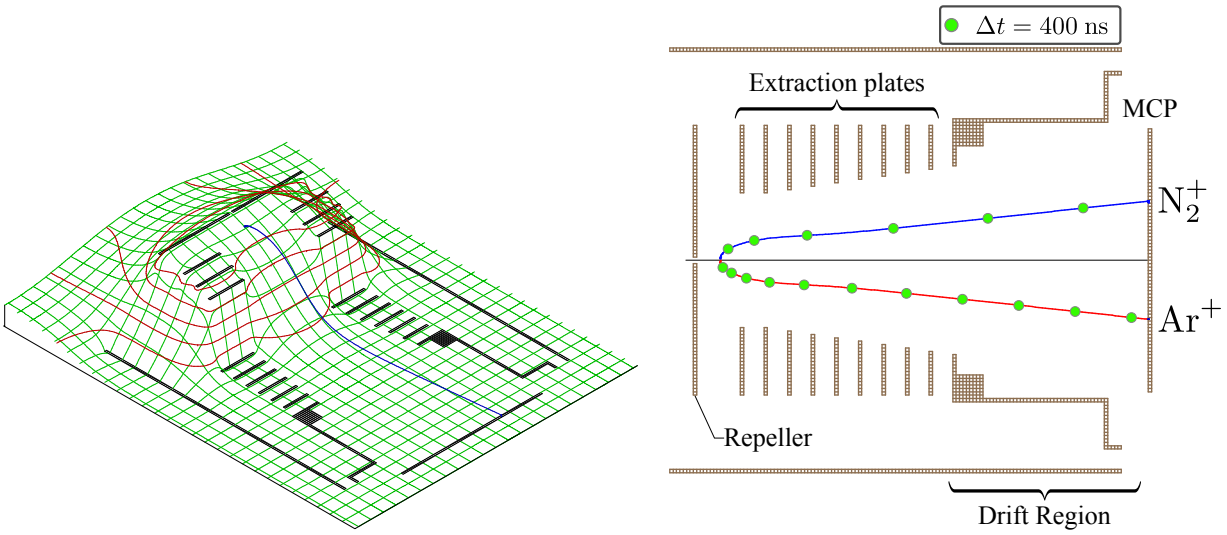

(a) Potential gradient across interaction region

(b) Simulated ion trajectories

Figure 3.18: *SIMION calculation of the VMI used in this work. Figure 3.18(a) illustrates the iso-potential surfaces created by our choice of spectrometer voltages. Figure 3.18(b) is a simulation of ion trajectories using N_2^+ and Ar^+. Each green blip represents $\Delta t = 400$ ns.*

pushed towards the detector.

The spectrometer produces the electrostatic force by applying a potential gradient across the detector plates, as seen in Fig. 3.18. The voltages applied to all the plates must be linearlly proportional to its neighbors in order to produce a linear gradient across the interaction region. While our spectrometer has *nine* plates (plus the repeller), for our purposes we only had to engage the first *three*, and grounded the rest. The actual voltages used are summarized in Table 3.2, which are reflected in Fig. 3.18.

We now provide a quantitative analysis of our VMI-TOFMS, linking the arrival time of an

Table 3.2: *Voltages applied to our spectrometer in the VMI-TOFMS.*

Spect. Plate	Applied Voltage (V)
Repeller	1000
Extractor 1	933
Extractor 2	866
Extractor 3	800
Extractor 4-9	0

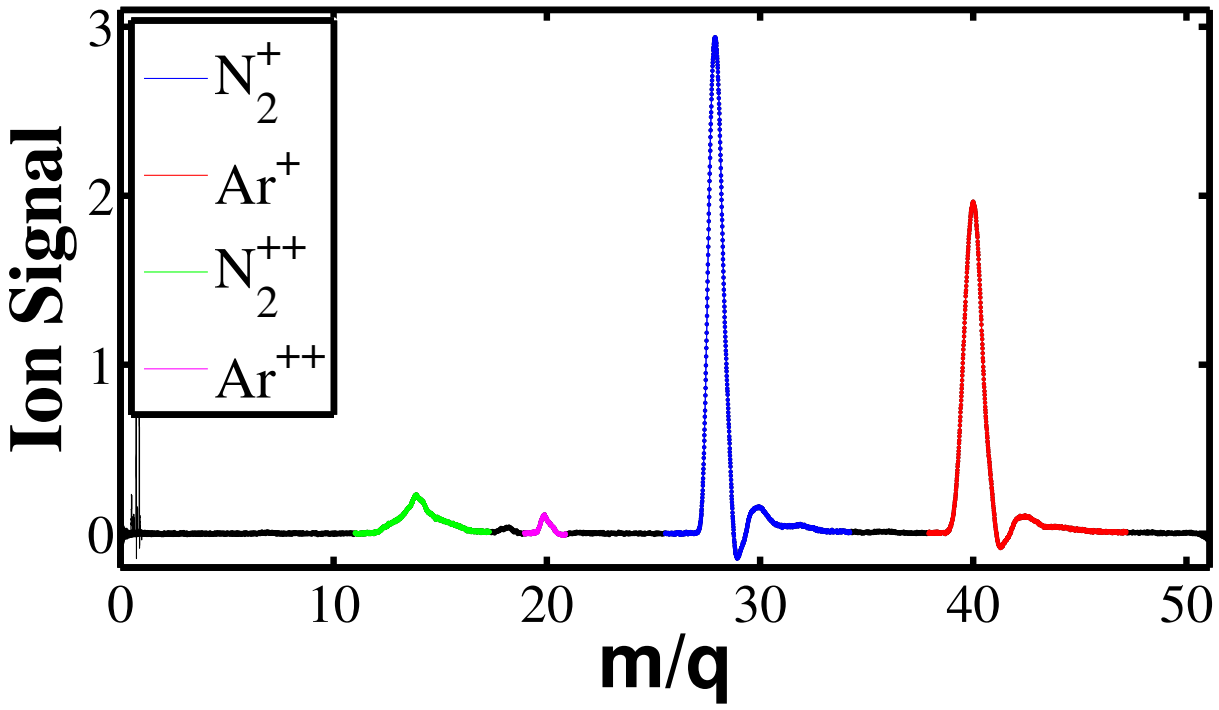

Figure 3.19: *TOF trace obtained from our N_2/Ar gas mixture, indicating the presence of both singly and doubly charged states for each species.*

arbitrary ion to the initial conditions and experimental arrangement. We begin by recognizing that a TOF apparatus consists of an *acceleration region*, and a *drift region*. The acceleration region is described by the section of the spectrometer in which the field provided by the charged plates provides a force on the ion which results in acceleration. The drift region is field-free, and does not provide any force on the ions, and therefore there is no change in the velocity. The purpose of the drift region is to allow the unique ions (traveling at different velocities) to accumulate a difference in arrival times at the detector, allowing them to be distinguished in the resultant signal. The analysis of the these two sections in our spectrometer will be discussed separately, and the results will be combined to provide a total time of flight of ions at the detector. We begin by studying the acceleration region, where the acceleration is found according to:

$$\mathbf{F} = q\mathbf{E} = m\mathbf{a} \longrightarrow \mathbf{a} = \frac{q\mathbf{E}}{m}. \tag{3.10}$$

The time and velocity of the ion subjected to the acceleration from (3.10) can be found straightfor-

wardly as

$$\begin{aligned}\mathbf{a} = \frac{\mathrm{d}\mathbf{v}_{\mathrm{acc}}}{\mathrm{d}t} \longrightarrow \mathbf{v}_{\mathrm{acc}}(t) =& \mathbf{a}\,\mathrm{d}t \\ =& \frac{q}{m}\int \mathbf{a}(t)\,\mathrm{d}t \\ =& \frac{q\mathbf{E}}{m}t + v_0 \end{aligned} \tag{3.11}$$

where v_0 is the initial velocity of the ion. The time it takes to reach the velocity we found in (3.11) is easily found,

$$t_{\mathrm{acc}} = \frac{m(\mathbf{v}_{\mathrm{acc}} - \mathbf{v_0})}{q\mathbf{E}}. \tag{3.12}$$

The position of the particle after this period of time can be found as well,

$$\mathbf{v}_{\mathrm{acc}}(t) = \frac{\mathrm{d}\mathbf{x}_{\mathrm{acc}}}{\mathrm{d}t} \longrightarrow \mathbf{x}_{\mathrm{acc}}(t) = \mathbf{v}_{\mathrm{acc}}(t)\,\mathrm{d}t \Rightarrow \frac{q\mathbf{E}}{2m}t_{\mathrm{acc}}^2 + v_0 t_{\mathrm{acc}} + x_0, \tag{3.13}$$

where x_0 is the initial position of the ion. We now analyze the drift region,

$$qV = q\mathbf{E}\cdot\mathbf{x}_{\mathrm{acc}}(t) \longrightarrow q\mathbf{E}\cdot\mathbf{x}_{\mathrm{acc}} = 1/2m{\mathbf{v}_{\mathrm{D}}}^2 \longrightarrow |v_{\mathrm{D}}| = \sqrt{\frac{2q\mathbf{E}\cdot\mathbf{x}_{\mathrm{acc}}}{m}}. \tag{3.14}$$

The drift time t_{D} is then

$$|v_{\mathrm{D}}| = \frac{\mathrm{D}}{t_{\mathrm{D}}} \rightarrow t_{\mathrm{D}} = \mathrm{D}\sqrt{\frac{m}{2q\mathbf{E}\cdot\mathbf{x}_{\mathrm{acc}}}} \Rightarrow \mathrm{D}\sqrt{\frac{m}{2qV}}, \tag{3.15}$$

where D is the length of the drift region. The total flight time of an ion is then a sum of (3.12) and (3.15):

$$\mathrm{TOF} = t_0 + t_{\mathrm{acc}} + t_{\mathrm{D}} \Rightarrow t_0 + \frac{m(\mathbf{v}_{\mathrm{acc}} - \mathbf{v_0})}{q\mathbf{E}} + \mathrm{D}\sqrt{\frac{m}{2qV}}. \tag{3.16}$$

This equation represents the *total* time it takes for an arbitrary ion to reach the detector. We can use a reduced form of (3.16) to identify peaks in a TOF spectrometer in a 0^{th}-order order approximation by letting $\mathrm{TOF} \propto C\sqrt{m/q}$, where C is some constant.

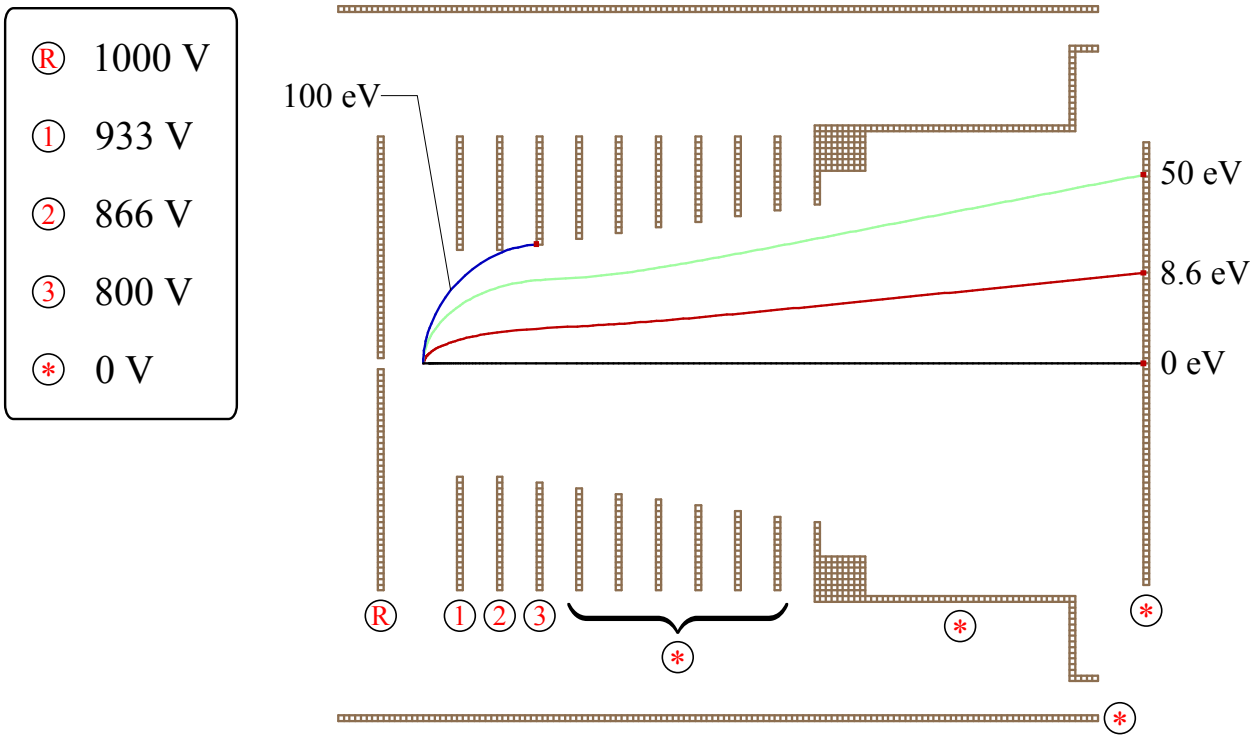

Figure 3.20: *SIMION calculation of the distribution of kinetic energies for the N^+ ion in our detector, where the most energetic fragment cannot be focused by the extraction plates and does not reach the detector. The simulation is performed for four different initial kinetic energies:* 0 *eV,* 8.6 *eV,* 50 *eV, and* 100 *eV. The kinetic energy release of a neutral Nitrogen molecule into two singly charged ions is given by* 8.6 *eV [82], which we note is far less than the upper limit of our spectrometer, at* 100 *eV. The initial kinetic energy of the fragments is parallel to the detector.*

To do this, we must recognize that in a typical TOF trace for a mixed molecular and atomic target (as in Fig. 3.19), that (3.16) does not hold true across all ions and fragments created in the interaction region. Specifically, this equation assumes that the initial conditions for all ions are the same, which is an invalid assumption. In particular, when considering the dissociation of molecular Nitrogen, we recognize that there is an initial kinetic energy of the fragments due to the kinetic energy release associated with the breakup. The equation from (3.16) assumes that the ion initially has a null initial kinetic energy; for the production of the singly charged Nitrogen *atom* (N^+) produced from the dissociation of the Nitrogen *molecule*, this is not the case. While the kinetic energy release for N^+ is 8.6 eV [82], this is not enough to cause a *significant* time difference detected at the MCP. Using SIMION using the same spectrometer voltages used to collect our data, we find that the addition of this kinetic energy results in a increase in the time taken for the ion to

reach the detector by only 1.39 ns, well *below* the temporal resolution of our oscilloscope.

Using TOF $\propto C\sqrt{m/q}$, we can find the approximate peak positions given the known location of the *heaviest*, *least charged* ion (*i.e.* the value of the largest m/q). This is performed on the raw scope trace, which are provided as a function of time delay from the scope trigger, which is engaged as the pulse registers a signal on a photodiode [`Thorlabs DET36A`], which marks the zero-time. Signals from the ion detector are registered on the oscilloscope as a function of delay from this initial trigger.

As an example, in the TOF spectra of molecular Nitrogen, the last ion detected will always be N_2^+, corresponding to $m = 28$ and $q = 1$. Therefore, we can find C straightforwardly by solving for the constant as $C \propto t\sqrt{q/m}$. We then apply this constant to the approximate expression for the ion flight time to the other ions in the TOF spectra. An example of this ion calibration being performed on one of the gas pairs studied in this work, namely N_2/Ar, can be seen in Fig. 3.19, we calculated $C = 0.46$.

As a final comment, we remark that there is an upper limit to the initial kinetic energy that our spectrometer is capable of sending to the detector. Fortunately, our apparatus was designed to accommodate fragments having an initial kinetic energy up to 100 eV, as depicted in Fig. 3.20.

3.4.2 Design and Construction

Our experimental apparatus, including the optical elements is shown in Fig. 3.21. The chamber itself is the "T," which contains the spectrometer and detector. The VMI-TOFMS used in this work was designed and constructed by Johnson and De *et al.* [83], and has provided data for a multitude of seminal publications across many groups [83–85]. The vacuum flanges used in the construction are Conflat [86], which utilizes a knife edge which cuts into the soft copper metal gasket. This provides an extremely leak-tight seal, allowing us to reach ultrahigh vacuum, on the order of 10^{-9} Torr.

The detection system is summarized in Fig. 3.24, where we see the major components critical to its operation. The entrance window to the chamber is a 1 mm thick fused silica window, and the focusing system is comprised of an externally mounted 3-axis translational stage, which actuates

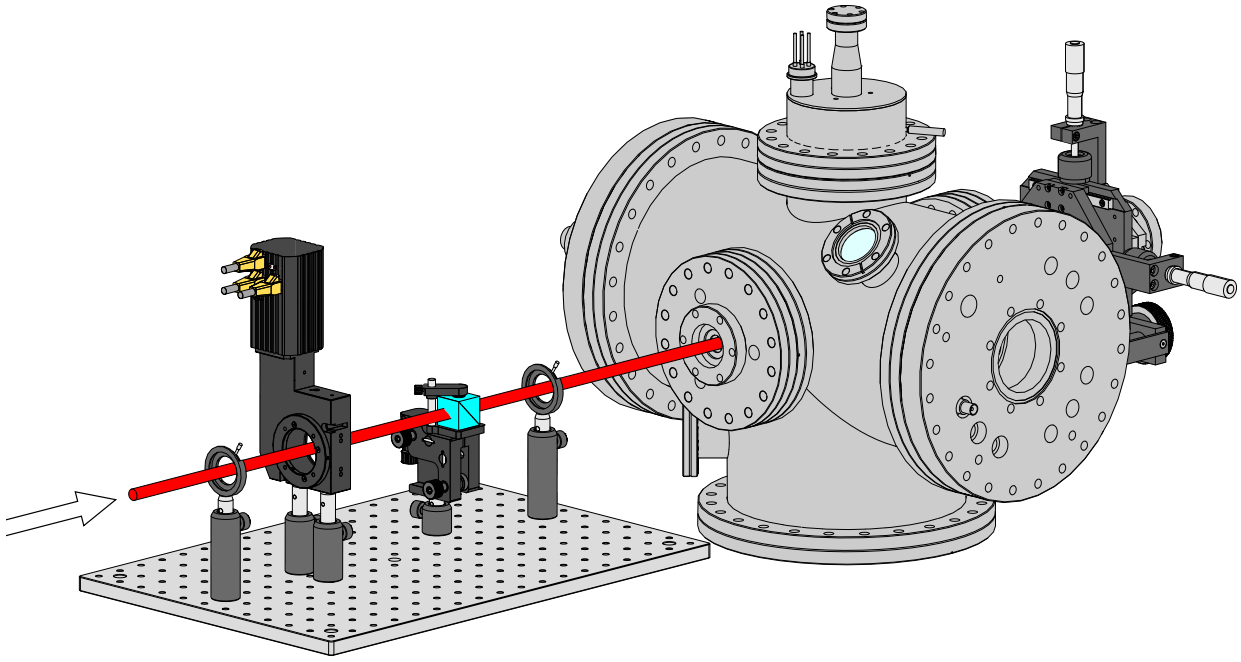

Figure 3.21: *The experimental arrangement of the ionization studies presented in this work. The optics on the breadboard constitute our intensity control system, while the spectrometer is located inside the chamber.*

the focusing mirror on the interior of the chamber through a Conflat bellows. The effusive gas jet is located at the center of the first spectrometer plate oriented along the spectrometer axis. The major components can be associated with one of two categories: the spectrometer, and the focusing system.

Spectrometer

The CAD drawings used to design the VMI-TOFMS are presented in Fig. 3.22, where in (a) the dimensions are imperial. We choose the voltages that we apply to the spectrometer by SIMulating the ION trajectories in a computer program called SIMION. This program calculates the trajectory by creating an array of user-specified potential fields, and an algorithm minimizes the action of the electrostatic force [87] on a charged particle. The results from this simulation for our apparatus can be seen in Fig. 3.18. From Fig. 3.18(a), we see a three dimensional representation of the potential gradient across the interaction region, along with several potential contours. In Fig. 3.18(b), we

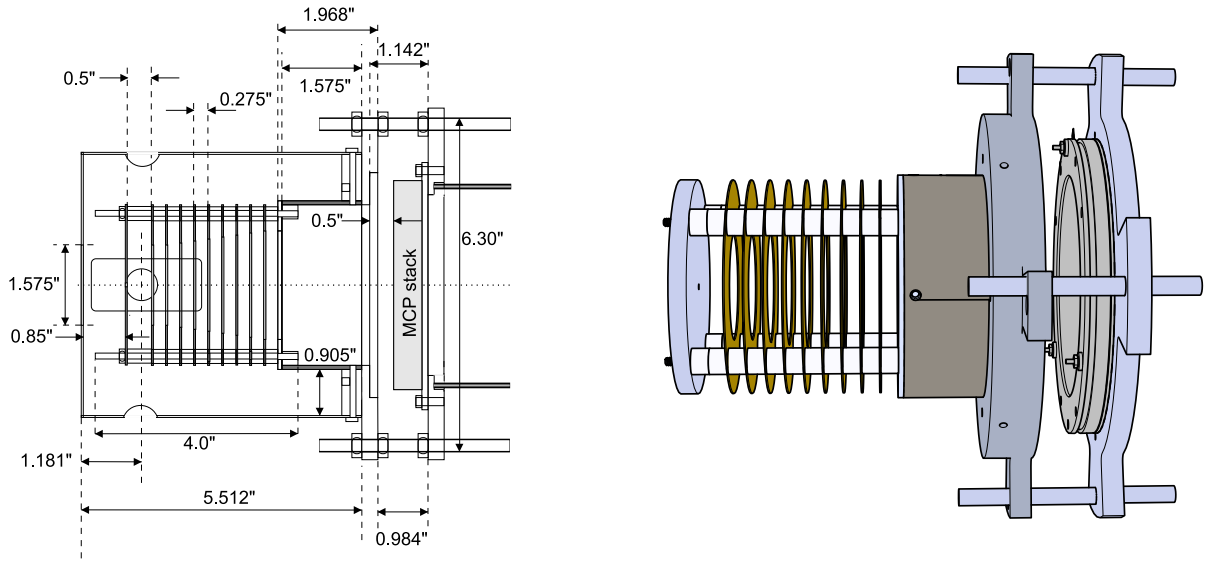

(a) Dimensional drawing

(b) 3D rendering

Figure 3.22: *CAD drawings used to design the spectrometer used in this work.*

show a simulation produced with our experimental arrangement for N_2^+ and Ar^+. The values for the voltages applied to the spectrometer plates are presented in Table 3.2 on pg. 55.

The green dots along the simulated ion trajectories represent a 400 ns time increment. We see that the density of green dots is much higher for the Ar^+ trajectory, which is due to the increased mass of Ar over N_2. The amount that the ion is accelerated by the force applied by the spectrometer

Table 3.3: *SIMION simulation for the gases used in this work, where the flight times for each respective ion to the detector in our apparatus is denoted as $t(\Lambda^{q+})$, where q is the charge of the ion fragment.*

Species	Mass (amu)	I_p (eV)	$t(\Lambda^{1+})$	$t(\Lambda^{2+})$	$t(\Lambda^{3+})$
C	12.011	11.260	1.5472	1.0946	0.8939
N	14.007	14.534	1.6709	1.1821	0.9653
O	15.999	13.618	1.7857	1.2633	1.0317
CO	28.010	14.014	2.3628	1.6716	1.3651
N_2	28.013	15.581	2.3629	1.6717	1.3652
O_2	31.999	12.070	2.5254	1.7866	1.4590
Ar	39.948	15.760	2.8217	1.9963	1.6302
Kr	83.798	14.000	4.0868	2.8913	2.3611
Xe	131.29	12.130	5.1155	3.6190	2.9554

is proportional to the mass, according to Newton's 2nd law. Therefore, it is natural that the heavier of the two particles (Ar) will arrive later than the lighter molecule (N_2). A summary of the time it takes for the ions studied in this work to reach the detector is summarized in Table 3.3. This table provides information for both the first ion trajectories Λ^{1+} as well as for the trajectories of the second ion, Λ^{2+} according to the design used in this work.

Focusing System

The focusing is provided by an on-axis concave spherical mirror with a focal length of $f = 7.5$ cm [`ThorLabs CM254-075-P01`]. The mirror is located on the interior of our vacuum chamber, between the repeller and first extraction plate. The mirror is adjusted via adjustments on the exterior of the apparatus, which allow for movement along the three orthogonal axes, as shown in Fig. 3.24. The x and y adjustments are made through two identical micrometers [`Starrett 63L`], while the z movement is achieved through a rail system controlled by a knob adjustment.

3.4.3 Ion Detection

The signal produced by the ions at the detector must be amplified before they can be measured. The device which serves this purpose is a Micro-Channel Plate (MCP) detector. The MCP consists of a dense array of thin capillaries, each of which can be considered to act like a miniature photomultiplier tube. An artist's rendition of MCPs can be seen in Fig. 3.23, the capillaries are semiconductor channels, which are biased with a linear voltage gradient applied to both ends of the MCP, as in Fig. 3.23(a). When an ion hits the channel wall of a capillary, it produces a secondary emission of *electrons*, which inevitably collides with the channel again, which yields a tertiary emission of electrons. This process continues a number of times until a cascade of electrons exit the back of the MCP plate, which can be seen in Fig. 3.23(c). The number of electrons produced is directly proportional to the number of ions hitting the detector. This way, we have an amplified signal which can be measured and is an accurate representation of our actual ion yield.

It is important that the gain of the MCP be consistent; damage to the MCP will lead to a reduced gain, producing a systematic bias to the data. Unfortunately, MCPs damage very easily, as saturating

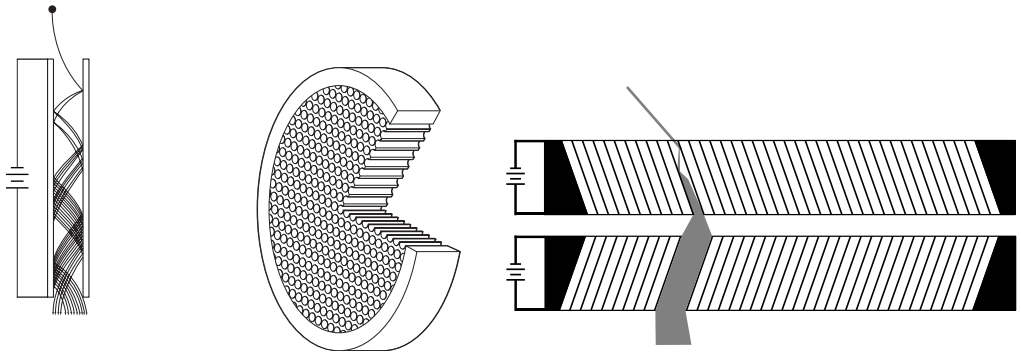

(a) Individual Channel (b) Microchannel plate (c) Microchannel plates in Chevron configuration

Figure 3.23: *Component view of the detection method used in this work. The individual channels from (a) make up any single MCP, as in (b) When two such plates are combined as in (c), the system is said to be in the Chevron configuration.*

the detector leads to a flux of cascaded electrons that is high enough to cause material damage to the channel walls. However, this is much more likely to happen when studying electrons, rather than ions. Generally, damaging MCPs can be avoided limiting the current through the detector.

In order to create a sufficiently high gain, two MCPs are commonly placed in series. A single plate has a gain on the order of $\sim 10^3$ electrons, whereas two MCPs placed in series will increase the gain to $\sim 10^7$. This configuration is very common, and when this arrangement is used, the MCPs are said to be in the *Chevron* configuration, as used in this work and can be seen in Fig. 3.23(c). We also note that the channels are angled slightly, ensuring that an incident particle (as well as the resulting cascaded electrons) hits the channel wall. Other configurations exist, such as a z-stack configuration, where three MCP plates are placed in series. The set of MCPs used in this work [`Photonis MCP 75/32/25/8 D 60:1 NR, MS`] is a detection-grade matched set, the details of which can be seen in Table 3.4.

The detection efficiency of an MCP depends on the mass, charge, and kinetic energy of the ion fragment. It has been postulated that this efficiency for ions follows functional form [9, 88, 89],

$$\varepsilon \sim \frac{Z}{\sqrt{m}},$$

where Z is the charge of the ion, and m is the corresponding mass. However, the actual function for the detection sensitivity of MCPs is not an analytic function. Furthermore, the sensitivity also has to do with the history of the MCP, or how it was mounted [90]. This correction has been applied to our data.

3.5 Gas Preparation

It is advantageous to take our ionization measurement simultaneously, as all the independent ionization features induced by the experimental arrangement are factored out, and what remains is a pure indication of the fundamental physical mechanism responsible for the discrepancy between the atom and the molecule. Simultaneous measurements reduces the amount of systematic uncertainty arising from fluctuations in laser intensity or alignment [10]. The simultaneously measured molecule/atom pairs are pre-mixed in a lecture bottle prior to leaking them into the chamber.

The optimal mixture ratio in the gas bottle is *not* 50/50, since the ionization rates are not constant across both molecular and atomic species. Experimentally, at a given intensity this results in a larger peak for the species which ionizes easier, while the other is much smaller. At low intensities, this results in the former being detected, while the latter producing no signal at all. This is not ideal – we want an ion signal from both species across the entire intensity range so that a ratio can be taken between the yields. In order to circumvent this issue, we offset the gas ratio in our lecture bottle to optimize the signal for both atomic and molecular signals at low intensities.

The ideal ratio was experimentally determined by making many adjustments to the 50/50 ratio and inspected at the TOF trace at the low intensities to check to see if the gas ratio was optimized.

Table 3.4: *Characteristics of the MCP used in this work.*

Plate diameter:	75 mm
Pitch:	32 μm
Pore size:	25 μm
Bias angle:	8^{o}
Aspect ratio:	60:1
Gain:	$> 10^{7}$

This was done many times for all pairs of gases used in this study. We remark here that this ratio, the relative partial pressures of each gas within the gas mixture, is crucial in order to have an accurate ratio. Typically, the device used to achieve this is an RGA.

3.6 Experimental Procedure

3.6.1 Preparing the Chamber

As our VMI-TOFMS is a shared apparatus, it is important that we take the appropriate action to reduce the presence of contaminants in the chamber introduced from a previous run. Furthermore, some of the molecules used in different gas mixtures overlap with the TOF signal produced from a different mixture. A key example of this is CO and N_2, both of which have the same mass at $m = 28$ amu. Therefore, the first ion signal for both CO^+ and N_2^+ would overlap if both are present in the chamber at the same time. This is avoided by properly venting and cleaning the chamber between runs from different gas mixtures. This is done by first evacuating the chamber, and then leaking the gas from the next mixture into the chamber. The chamber is evacuated again, and this process is repeated until no contaminants are present in the TOF spectra.

We control the amount of gas introduced into the apparatus by way of actuating a needle valve, and checking the current pressure by using an ion gauge [`Granville-Phillips Series 330`]. After the desired gas pressure is obtained, the pressure will continue to fluctuate over time before finally reaches an equilibrium value. It is crucial that the scan is not started until this equilibrium is reached; otherwise a changing ion signal will be a product of not only the ionization process, but also on the number of neutral particles in the interaction region. Generally, we waited approximately 30 minutes after reaching our desired pressure to begin a scan.

3.6.2 Alignment Procedure

Due to the fact that the VMI-TOFMS is a shared apparatus, all optical components must be installed and aligned at the beginning of each run. It is crucial to remain consistency on data collected on different runs, and so a very careful alignment procedure must be followed. In particular, it is of the

utmost importance that the beam entering the chamber is hitting the center of the on-axis spherical mirror inside the chamber. This is important because if a beam is coming in at an angle or not hitting the mirror in the center, focusing errors will occur in the focused beam. In fact, any aberrations will result in a *larger* focal region than one would have with perfect alignment, and so the intensity calibration will not reflect the actual experimental conditions. When the chamber was originally aligned, it was done so with respect to two irises exterior to the chamber. The position of these irises is absolute and must never be adjusted. Therefore, all that is needed is to do is make sure that the laser is coming in straight through theses irises, and then the alignment onto the mirror is automatic. The first step in aligning the experiment is always to bring the beamline to be aligned through these two irises with no elements present.

The next step is to place the Polarizing Beam-Splitter (PBS) in the beamline. The mount for our PBS [`CVI Melles Griot 1800`] allows for three degrees of freedom . The positioner actuating the tilt of the polarizer (rotation around beam propagation axis) is achieved by optimizing the width of the highest charged ion in the TOF spectra to be as narrow as possible. The reason for this is based in the physical principles of how the polarizer works, which is summarized in Fig. 3.12 on pg. 45.

Vertical polarization is necessary for the TOF detection scheme, since the spectrometer axis is perpendicular to the incident beam, then ions will be pushed in the direction of the laser polarization. For a vertically polarized beam, the ions will be produced *parallel* to the plane of the detector. On the other hand, a horizontally polarized beam will eject ions *perpendicular* to the plane of the detector. The latter results in ions of the same m/q arriving at different times at the detector, resulting in a wider signal than one would have with a vertically polarized beam. The effect that a horizontally polarized beam has on a TOF spectra can be seen in Fig. 3.25. Therefore, the tilt of the PBS, which controls the transmitted polarization, can be optimized to yield the narrowest ion signal.

The two other degrees of freedom on the PBS are aligned using the common technique of overlapping the back-reflected beam onto the incident beam. Since the polarizer is uncoated, it reflects about 4% of the incident beam; if the face of the cube is perfectly perpendicular to the beam axis, then the reflected beam will go back along the beam axis.

If the beam is perpendicular to the cube face, then there will be no path length difference than if there was no cube and hence no adjustment of the beamline is necessary center around the mirror.

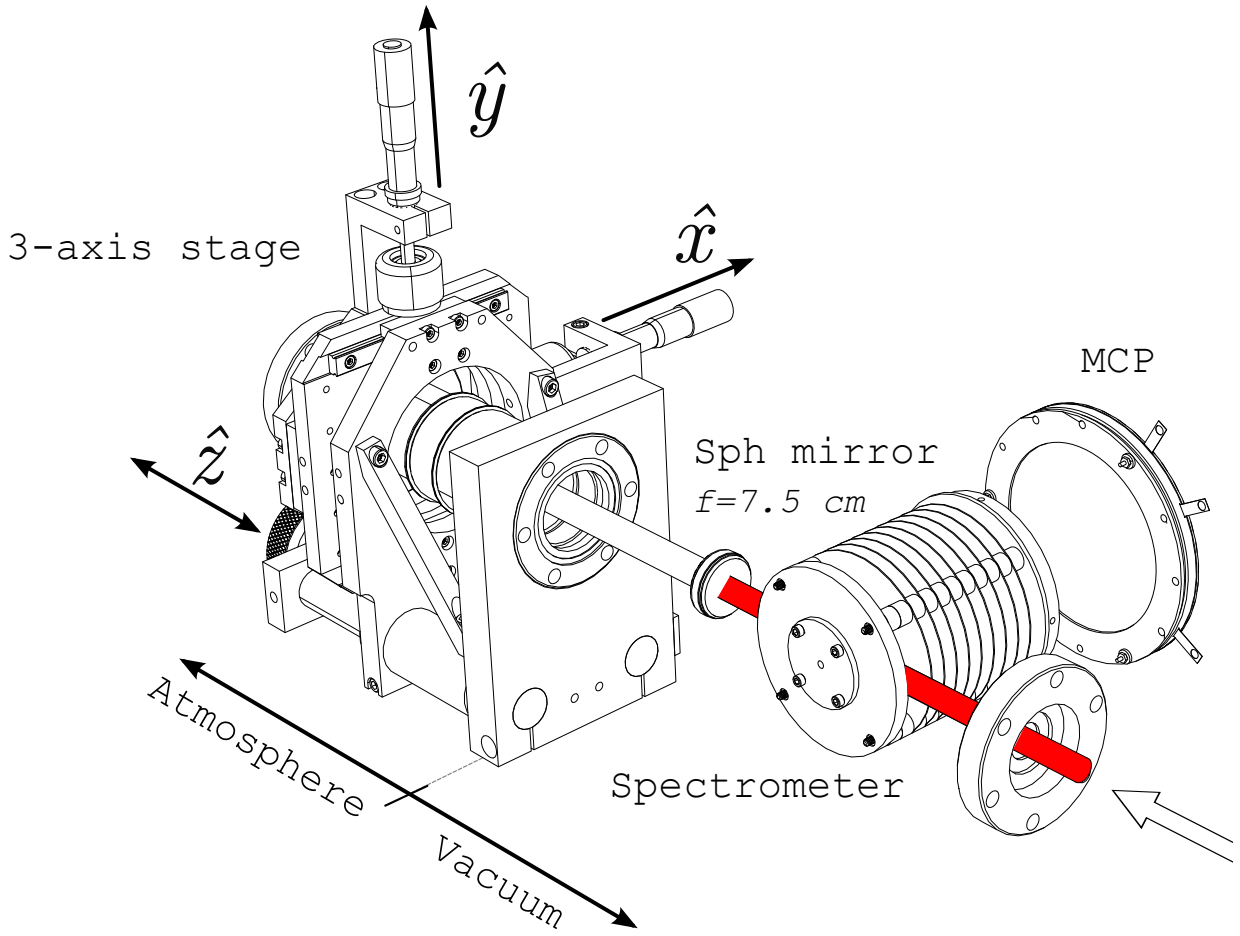

Figure 3.24: *Major components and positioning mechanisms used to align our apparatus. The positioning mechanisms lie on the exterior of the vacuum chamber, and control the focusing mirror on the interior of the chamber.*

The alignment is verified by checking that the beam is still aligned through the two outer irises. If the alignment of the polarizer is incorrect, the outer irises will be misaligned, and if so the beamline is adjusted until it is brought back. The Half-Wave Plate (HWP) mounted on a motorized stage is then placed before the PBS and aligned. An advantage of using a PBS over a thin film polarizer is that cube polarizers have large contrast ratios, any beam containing any sort of ellipticity will be decomposed such that the the horizontal and vertical components go along different paths. Therefore, an elliptical beam being sent through this system will result in a loss of power at the exit, as it only passes linear polarization. This is not a problem unless power loss is unacceptable, which was not the case in our experiment. Nevertheless, the experimenter did not pretend to be immune

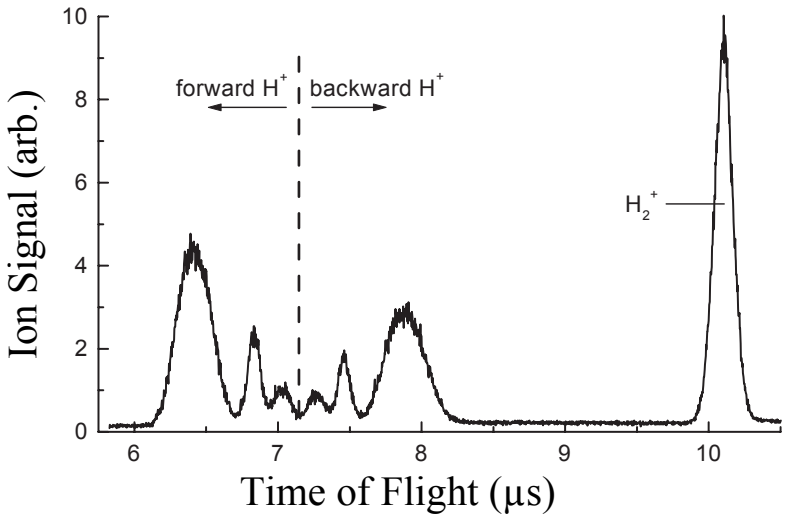

Figure 3.25: *Experimental TOF spectra for H_2, showing the effect of a horizontally polarized beam on our experimental arrangement. Each ion is split into two peaks instead of one. Figure adapted from [91].*

to faults in logic, so the following procedure was followed in order to align the half-wave plate appropriately. Misalignment is again detected via back-reflection, as was previously done with the polarizer. The HWP is AR coated, so the magnitude of the reflected beam was miniscule. By using a punched-out IR card as before, misalignment is detected as an illuminated spot on the card. The alignment of the beamline is once again checked through the outer two irises, and adjustments to the beamline are made if necessary.

We now optimize the on-axis focusing mirror on the interior of the chamber can be adjusted via actuators mounted on the exterior of the chamber connected via feedthroughs. The voltages applied to the spectrometer are slowly ramped up to their predesignated values (see Table 3.2 on pg. 55), corresponding to the values used in the SIMION simulation. At this point, the voltages on the detector are slowly ramped up, until the desired gain is achieved.

Now that we have a live TOF trace, we proceed in optimizing the position of the focusing mirror. We define our coordinate system for this as follows: the x and y-directions represent the perpendicular components with respect to the initial beam, while the z-axis is defined as the propagation direction of the beam. A depiction of these coordinates with respect to the major components can be seen in Fig. 3.24. If we are looking at the mirror from the perspective of

the laser, then The y-axis is up/down, while the x-axis is left/right. Both the y and z-axes are aligned by optimizing the ion signal, meaning that the largest signal produced corresponds to a larger intensity, and hence a better alignment. Therefore, both these directions may be adjusted straightforwardly by finding the maximum signal from the highest ion present (higher ions have a stronger intensity-dependence than the first ions). The x-axis, which controls the distance between the mirror and the repeller, is a little more difficult to optimize. Moving the mirror towards the repeller will always result in higher ion signal, as the density of the gas jet increases closer to the repeller. This is optimized from the central position only slightly (if at all) to avoid this confusion.

Now that the chamber and all elements are aligned, we need to optimize the compressor to yield a transform-limited pulse at the interaction region. The chirp is controlled at the compressor, where the distance between the two gratings is changed to yield a *negatively* chirped pulse at the output of the amplifier. This is optimized until the accumulated chirp to the apparatus from free space and transmissive optics equals the amount of chirp induced by the compressor, yielding a transform limited pulse inside the chamber.

In order to find the TL pulse, two steps are necessary. The first is to find the rough position for the grating, and the second is to fine tune the position. The rough position is found by creating a supercontinuum from a plasma of the focused beam at the entrance to the chamber. The supercontinuum, a highly nonlinear process, is an intensity-dependent process, in which a wider spectrum is generated with a shorter pulse. This can be quantified either optically by looking for the grating position that yields the brightest possible plasma, or by maximizing the noise generated by the plasma. This sound represents a single pulse creating a plasma, making a popping sound. The frequency of these pops correspond to the repetition rate of the laser used; in the case of KLS, which has a frequency of $f = 2$ kHz, which is a frequency well within the normal audible range of humans [92]. By optimizing the grating to correspond to the loudness pops, one can find the shortest possible pulse. However, this procedure only gets us into the correct ball park; fine adjustments are necessary before the pulse can be said to be transform limited. The second stage is achieved by looking at the TOF spectrum and optimizing the height of the highest charged peak at low energies to avoid saturation.

3.6.3 Setting up and Continuing Scans

The resolution of our detection system is limited by the minimum measurable signal at low intensities, and by saturated at high intensities. The *dynamic range*, or more generally the signal/noise ratio, is determined by these limits. We circumvent this limitation by making three independent scans over different intensity ranges, and joining the scans at the overlaping regions. This technique has proved invaluable in the collection of ion yields ranging continuously from the MPI regime to the tunneling regime. Each of these scans has a different fill pressure in the chamber, for the following argument. . We note that higher pressures could only be used at low intensities, since a lower number of ions are produced. Therefore, space charge effects and detector saturation can be avoided. When changing pressures, it is important to preserve linearity between the scans, otherwise they cannot be combined. The two possible sources of these nonlinearities are from space charge, and MCP saturation. Space charge occurs when the potential created by the residual ions affects neighboring ions. This induces a broadening of the energy spectra produced from any particular ion. In a TOF apparatus, this results in a spread-out ion spectrum.

One way of detecting space-charge is by a noticing a reduction in resolution in detecting isotopes from an ion signal. For example, the three most naturally occurring stable isotopes of Xenon are $^{129}Xe^{+}$ at 26%, $^{131}Xe^{+}$ at 21%, and $^{132}Xe^{+}$ at 27%. Since $t \sim m/q$, the arrival times for each of these ions will be different, the heavier isotopes arriving later. If space-charge is not present, then each of these peaks will be easily resolved. If the pressure is increased to produce space-charge, the effect is to "smooth out" the three individual Xe^{+} peaks, making it appear as a single (wide) peak.

The extent to which space charge becomes appreciable can be quantified by estimating each of the ions as an ensemble of spheres of charge. When two spheres come within one diameter from of one another, the spheres (representing the potential field of each ion) breach one another, implying that the field of neighboring ions is affecting others. The effect that space charge has on the energy of ejected ions is proportional the number of spheres that are contained within the focal volume. If the actual number is more than enough for each sphere to breach the surface of its neighbors, then space charge occurs. Space-charge acts to create a spread in the arrival times of the ions by altering the potential applied by the spectrometer with the presence of a plasma due to the density

of ionization events in the interaction region. This change in effective potential experienced by the ions alters the rate of acceleration along the detector, resulting in a wider distribution of arrival times.

A more realistic approach to quantifying space charge is by careful choice of the intensities and pressures for each scan. Prior to each scan, the pressure is adjusted to the approximate value needed for the intensity range of that scan. The HWP is rotated for maximum attenuation, and the beam is sent in and the TOF spectra is monitored live. The angle of the HWP is increased slowly, until a signal becomes visible on the oscilloscope. This marks the lowest intensity with a detectable signal, *e.g.* the start point of the low intensity scan. The HWP angle is then increased to the maximum intensity for that particular scan (usually about a decade), and the presence of space charge evaluated. If no space charge is present, the current intensity value is set as a maximum for that scan. In the case that space charge is present, the issue can be solved either by decreasing the intensity, or adjusting the pressure.

If the flux of ions at the detector is too large, the MCP will saturate. After MCP saturation, an increase in the flux of the actual ions will not be reflected in the MCP signal. We avoided MCP saturation by carefully controlling the flux of ions sent towards the MCP, ensuring that the signal was reasonable. Once the voltages on the MCP were set, they were not adjusted for the remaining scans in the data set.

It is important that nothing is changed in the alignment of the laser as well; even slight adjustments can be detrimental, whether by a user or by natural causes as each set of scans takes $16-24$ hours to complete. However, the laser must be shut down every 8 hours to refill the liquid N_2 cooling the Ti:Sapph gain medium in the amplifier. While the oscillator remains untouched by this process, both pumps on the amplifier are shut down. If the start-up process for the laser is not done correctly, we found that the alignment of the beam will shift. We found that this problem could be avoided by *slowly* increasing the current to both pumps to the maximum value over a period of 15 minutes, rather than straight away. Doing this slowly has the advantage of allowing the LBO pump controllers to slowly acclimate to the increasing temperature on the laser diodes. The efficacy of this methodology is checked by verifying the alignment through the same irises used to do the initial alignment.

The half-wave plate and polarizer are also checked to verify the calibration is correct. At the beginning of each data set, the angle of the HWP is calibrated such that 0^o corresponds to the maximum attenuation. Then, by rotating the HWP by 45^o the polarizer has maximum transmission. This calibration remains unchanged unless the polarization of the incident beam changes. While this is unlikely to occur between scans in the same set, the experimenter does not admit to being immune to fallacies, and so the calibration is checked for consistency.

The power that is read in is calibrated at the beginning of each scan. This is done in our data-acquisition software from Fig. 3.26, and is performed by reading in the instantaneous analogue signal from the power meter and making a simultaneous measurement of the power using a hand-held power meter [`Coherent Fieldmate/PS19`]. Our software calibrates the raw analogue voltage to the manual measurement. The calibration constant is found by taking two simultaneous measurements. The first is from manually measuring the power at the entrance to our chamber, while the second is the analogue signal at that same moment. By taking both values simultaneously and dividing the two, we define our power calibration constant: $C_{\text{pwr}} = P_{\text{man}}/P_{\text{anlg}}$. By multiplying the raw analogue signal by C_{pwr}, the result is a calibrated signal. Therefore, referring to this signal is akin to referring to the instantaneous power at the location of the measurement. This calibration must be performed at the beginning of each scan.

These calibrated power values are stored for each data point taken. In the analysis, we use these power values to quantify how the instantaneous power changes away from the central position. The final data points used in the analysis lie within a certain deviation from this central position. The data points corresponding to power fluctuations outside of this range are discarded in the final analysis. The procedure used to discriminate data points based on these measurements were discussed in §3.2.2 on pg. 42 of this document.

3.7 Data Acquisition System

Our Data Acquisition (DAQ) system consists of a high-pass filter, an oscilloscope, and the acquisition program on a laptop computer. The purpose of the high-pass filter is to block the low-frequency, high voltage DC signal, while passing the high-frequency AC signals. Our high-pass filter consists

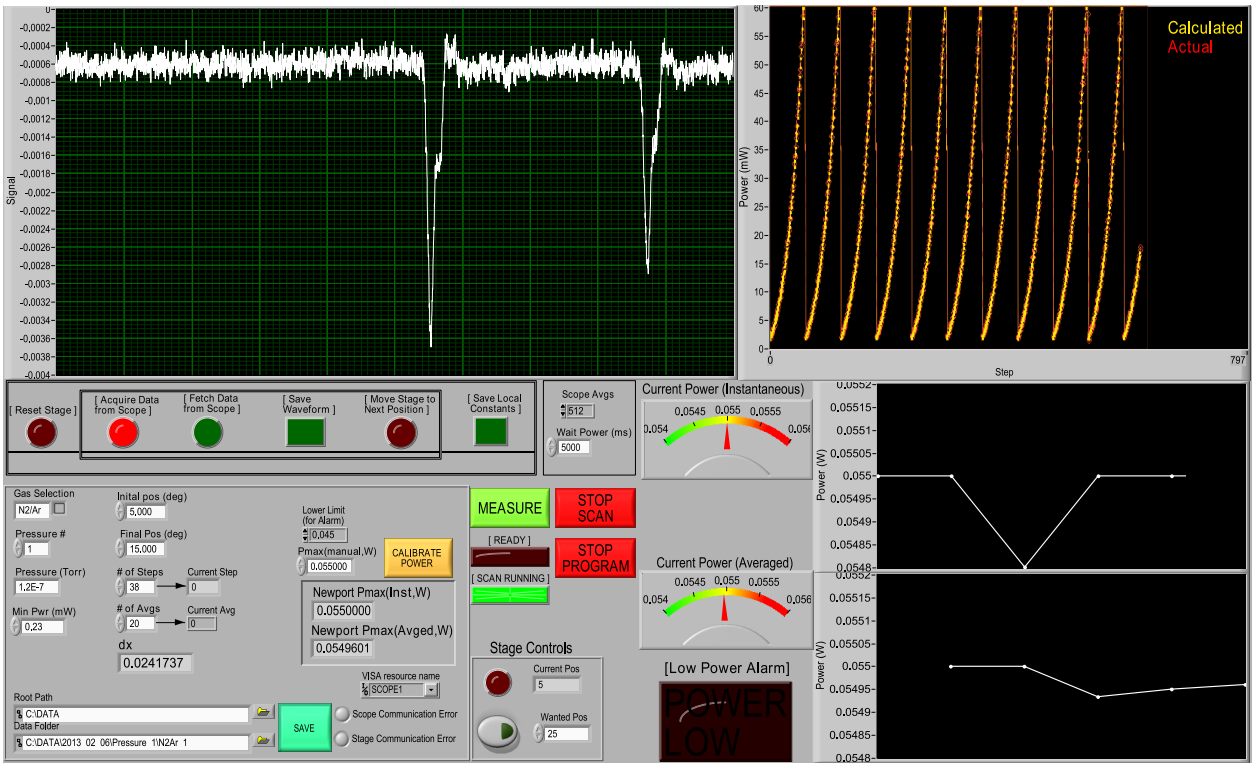

Figure 3.26: *LabVIEW Front panel of our data acquisition program created specifically for this measurement. The raw scope trace can be seen in the top left, immediately blow which are a row of LEDs, which indicate the current operation being procured by the program. The right-half of the panels are for power monitoring; the upper right indicator plots the power after the intensity control optics for all data points collected over all steps and averages of the scan. The pair of charts on the bottom left indicate the instantaneous (top) and the running-averaged power over the acquisition of the corresponding data point.*

of resistors and capacitors, hence its nickname of an RC filter. The implementation of our high-pass filter can be seen in Fig. 3.27. In this figure, the HV-in signal is provided by the high-voltage power supply, while HV-out represents the voltage applied to the detector, which is typically set at 1.8 KV. Using Kirchoff's laws for solving circuits, we can quantify how the HV-out signal is related by the HV-in signal,

$$V_{\text{out}} = \frac{Z_2}{Z_1 + Z_2} V_{\text{in}}, \tag{3.17}$$

which is the voltage divider equation for a simple circuit in terms of arbitrary impedances. In our case, Z_1 is the impedance of the capacitor C, while Z_2 is the impedance of R_{eq}. We recall that the

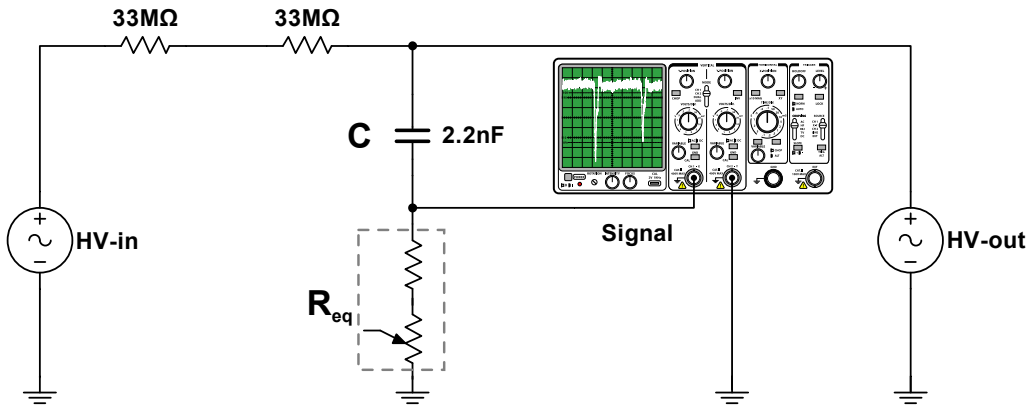

Figure 3.27: *Circuit diagram of the high-pass filter used in our data acquisition system. The value of the capacitor* ***C*** *and equivalent resistor* $\boldsymbol{R_{eq}}$ *are chosen to block the low-frequency signals from the total detected signal on the oscilloscope.*

impedance of a resistor and capacitor is given by $Z_R = R, Z_C = (i\omega c)^{-1}$, and so (3.17) becomes

$$V_{out} = \frac{1}{1 + (\omega R_{eq} C)^{-2}} V_{in}. \tag{3.18}$$

We can take the limit of the gain in (3.18) as $\omega \to 0$ (the low-frequency limit) and also as $\omega \to \infty$ (the high-frequency limit), where we find that $V_{out}(\omega \to 0) = 0$ and $V_{out}(\omega \to \infty) = V_{in}$. In other words, this circuit attenuates the low-frequency signals, and passes the high-frequency signals. The potentiometer contained in R_{eq} is adjusted to match the impedance of MCP detectors, which is usually on the order of 20 MΩ.

The oscilloscope [`Tektronix TDS-3054B`] used to receive the signal in this work is also shown in Fig. 3.27. This is used to interpret the analogue signal from the RC filter into a digital signal. The waveforms are extracted from the scope via an RJ-45 patch cable[¶], which is connected to the laptop computer used for acquisition [`Sony VAIO VGN-690z`]. The waveform is digitally transferred, where it is saved by our DAQ program from Fig. 3.26

[¶]A patch cable is an ethernet cable which allows for direct communication between two devices directly, without the need for a router or a switch. This is done by switching the send/receive cables on one end of the ethernet cable.

3.7.1 Interpreting the Signal

We also make comments on the data which is collected using our DAQ system. Our ion signal is evaluated by integrating the ion peak in the TOF spectra, and we subtract the background of each ion signal separately, which is discussed in detail in §4.1 on pg. 78 of this document. We control the linearity of this method by carefully adjusting the pressure of the target species in the interaction chamber, which acts to control the density of particles in the focal volume. The voltages applied to our spectrometer are able to collimate a broad range of initial kinetic energies on the detector, as discussed in §3.4 on pg. 53.

[This page intentionally left blank]

Chapter 4

Experimental Results

Currently, molecular ionization models do not agree well with experiment, and the difference between the two is very large [9, 10, 93].

The primary motivation for the work presented in this thesis is to provide a comprehensive data set which can be used to improve existing models for the strong-field ionization of molecules. Our approach is to simultaneously measure the singly-charged ion yield of a diatomic molecule paired with a noble gas atom, both having commensurate ionization potentials. In this work, we study three such molecule/atom pairs: N_2/Ar, O_2/Xe, and CO/Kr. Our measurements are taken as a function of the laser intensity, typically spanning two orders of magnitude ($10^{13} - 10^{15}$ W/cm^2). By taking the ratio of the *molecular* to *atomic* yields as a function of laser intensity, it is possible to "cancel out" systematic errors which are common to both species, *e.g.* from laser instability, or temperature fluctuations. This technique is very powerful in our ionization studies, as it alludes to the distinct mechanisms leading to the ionization of both molecular and atomic species at the same intensity which are not a direct consequence of the experimental conditions. By using the accurate treatments of atomic ionization in tandem with existing molecular ionization models as a benchmark, we can use our experimental ratios to modify existing molecular ionization theories.

In this chapter, we directly compare our experimental results to theory performed using our experimentally determined focusing conditions. This analysis is performed for two of the molecule/atom pairs we studied in this work: N_2/Ar, and O_2/Xe. We are currently awaiting theoretical results for the CO/Kr pair. We begin by discussing the relevant details used to perform the analysis on our raw

data, with special attention on our absolute intensity calibration. We then introduce our analyzed data in the form of intensity-dependent yield plots for both the molecular and atomic species in each pair, followed by the ratio of the singly-charged yields. Our results are then discussed, and compared to similar works from the literature.

4.1 Analysis & Data Preparation

Our intensity-dependent ion yields are generated by numerically integrating the TOF signal for each ion. An example TOF spectra for each molecule/atom pair studied in this work can be seen in Fig. 4.1, where the first ion for both molecule and atom are highlighted to indicate the region of interest. In inspecting these TOF spectra, we notice that there is a rather large amount of noise present in the ambient TOF signal. This noise originates from a variety of sources, which appeared to be consistent throughout the entire measurement process. We postulate that the majority of this noise comes from ambient electrical background, even though isolation techniques were utilized in an attempt to reduce the magnitude of this noise. In particular, the power source used by all sensitive electronics in our experiment was sourced from an isolated transformer (called "clean power"), which is not shared with the power mains of the building. Not doing so would introduce a systematic error to our data, as fluctuations caused by mechanical electrical components would influence the power supplied to our sensitive electronics. For example, vacuum pumps are not connected to the clean power line, since they produce a time-dependent impedance which effects the voltage of all potentials in the circuit in accordance with Ohm's law. We can quantify the efficacy that this system has on isolating noise by taking the Fast-Fourier Transform (FFT) of the TOF spectrum. In particular, we found that no noise contributions matching the rotational frequency of the turbo were found, indicating that it was not the major contributing factor to the noise in our TOF spectra.

A large amount of noise in the TOF spectrum limits the effective dynamic range of the acquisition system, and acts to mask the ionization features in low-signal areas of the TOF spectra. Since a large amount of this noise is *random*, it is possible to eradicate much of the noise by taking a multitude of averages. The oscilloscope used in our data collection [`Tektronix TDS-3054B`] has the ability to average signals on-board, the maximum number of averages being limited to 512. Since we only

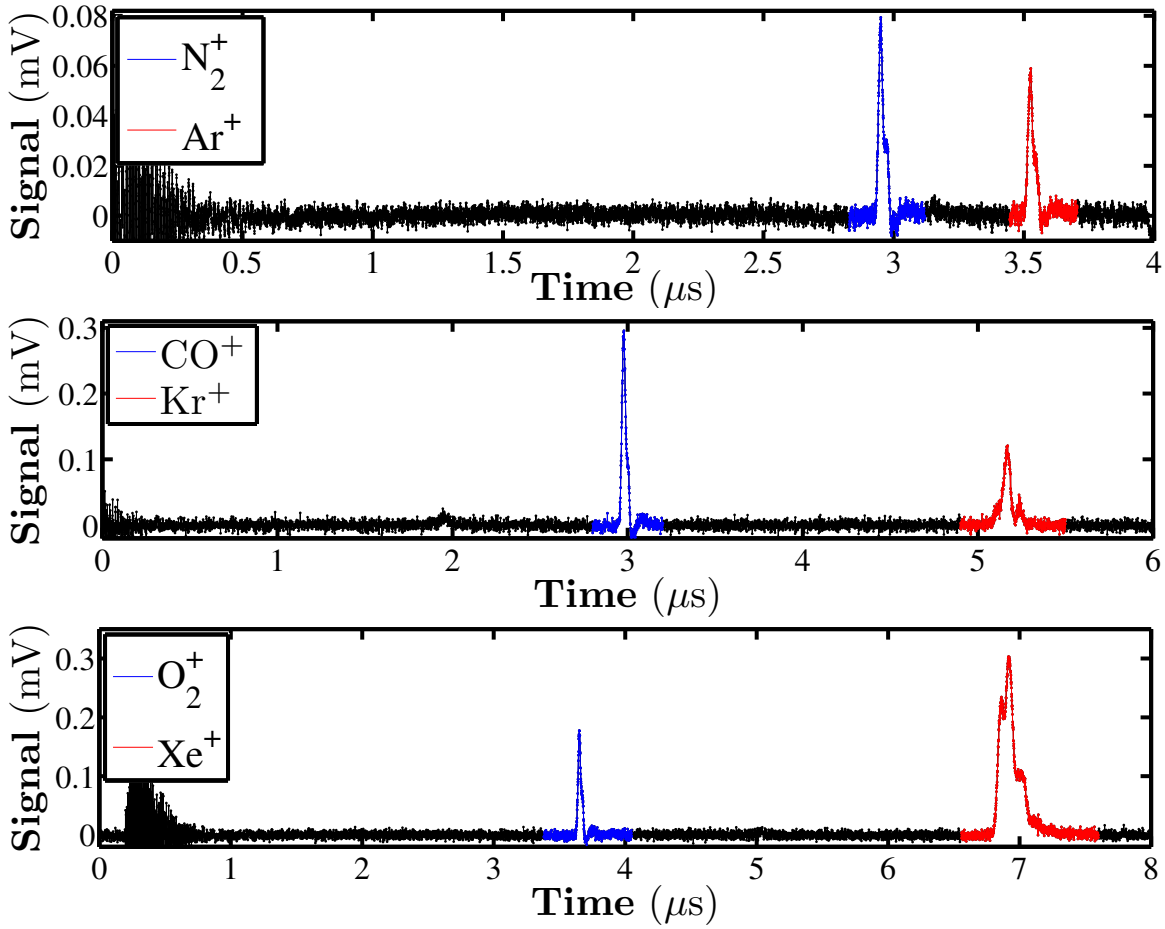

Figure 4.1: *TOF spectra for all three pair studied in this work. The highlighted regions indicate the area of interest for each molecule/atom pair in this study.*

obtain the final averaged value of any given scope-averaged TOF spectrum, the fluctuations from shot-to-shot can not be deconvoluted from the total averaged signal received by the scope. However, this is only a problem if we wish to include the statistics of each shot in the final calculation of error in the final analysis. For this reason, the error bars in our measurements do not take into account the individual fluctuations within the scope averages, but are derived from the final scope traces provided by the scope. In the low-intensity region for all scans, on the order of 20 averaged traces from the scope are taken for any given intensity, meaning that approximately 10^4 total points are taken for each data point seen in our intensity-dependent yields. This high number of averages is necessary in order to obtain sufficient statistics in order to draw meaningful conclusions from our data at the lowest intensities. However, we remark that the cost of accumulating such a large

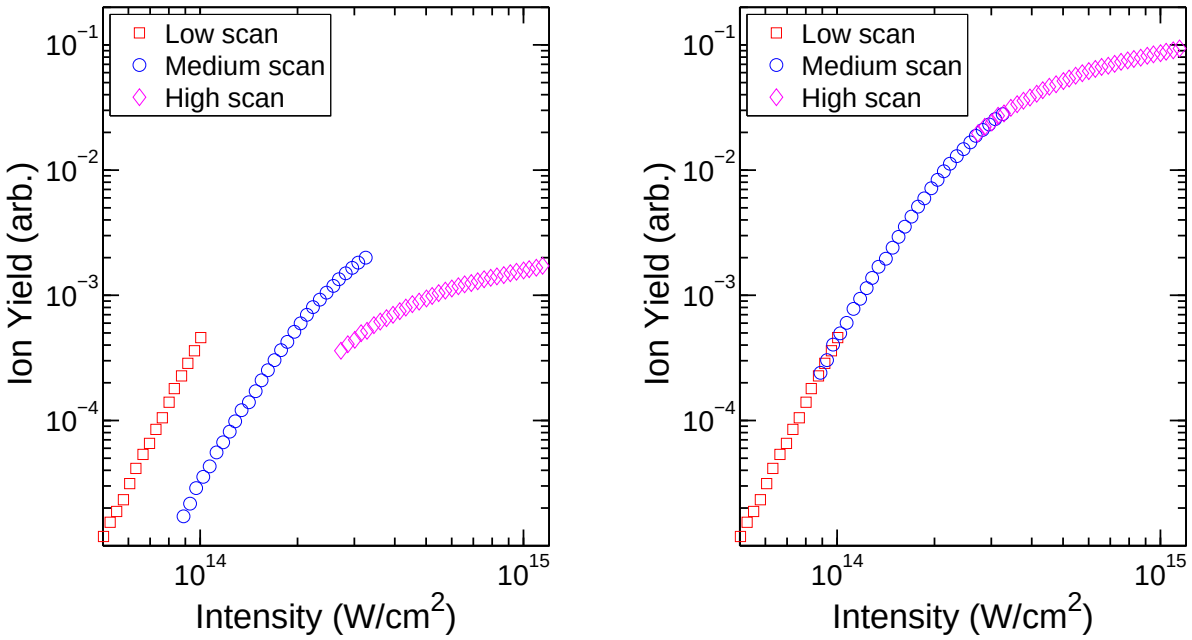

(a) Unstitched scans

(b) Stitched scans

Figure 4.2: *An example of how we combined, or "stitch" several independent scans together for the Ar^+ scan. In (b), we have the independent scans which have not been normalized. By matching the overlapping data points in the interstitial region between any two scans, we can match the ion yields and connect the curves, as in (b). A summary of the individual and total intensity ranges, as well as the different fill pressures used in each scan, can be seen in Table 4.1.*

number of averages are long scan times. In order to take a full scan (consisting of three individual scans, corresponding to the low, medium, and high-intensity scans, see Fig. 4.2), the amount of time needed to gather the data is on the order of 20 hours. This presents other issues, which must be addressed, in particular with the stability of the laser source being used. Laser instabilities over the data collection were minimized by utilizing *power-locking*, as discussed in §3.2.1 as well as by implementing a power selection and discrimination scheme, entailed in §3.2.2.

Background subtraction is also a critical component of our data analysis scheme. We implemented several methods of background subtraction, with varying degrees of success. We eventually landed on performing an individual background subtraction for each ion signal *individually*, rather than performing a single background subtraction and applying it to the entire TOF spectra. This is achieved by first selecting the region of interest containing the desired ion signal (as indicated in

Table 4.1: *Intensity ranges and dynamic range of three individual Ar^+ scans.*

Scan	Intensity Range (W/cm^2)	Dynamic Range	Pressure (Torr)
Low	5.0E13 – 1.0E14	1.6	1.1E-5
Medium	8.8E13 – 3.3E14	2.1	3.2E-7
High	2.7E14 – 1.1E15	0.7	4.9E-8
$\sum$	5.0E13 – 1.1E15	3.9	-

Fig. 4.1), and normalizing the endpoints to zero. The integration is then performed by numerically summing the spectrum.

Unfortunately, the time-dependent noise present is something that we were not able to entirely eliminate from our scans in the analysis stage, and so this provides a source of error in our data. In particular, the *dynamic range* of our detected yields is fundamentally limited by the magnitude of these fluctuations. We were able to increase the effective dynamic range in our data by combining, or "stitching" several separate scans together, as discussed in §3.6.3 on pg. 70, and is also exemplified in Fig. 4.2 for our Ar^+ data. Each of these scans constitute three different intensity regions, where each data set consists of three different scans, each with a different fill pressure. The low-intensity scan is performed with very high chamber pressures, typically on the order of 10^{-6} Torr. The amount of power sent into the chamber at such high pressures must not exceed a critical value, above which space-charge occurs and damage to the detector becomes much more likely. In the low-intensity scans, typically a maximum power of $\sim$ 15 mW was sent into the chamber, ensuring that space-charge and detector saturation do not occur. The medium-intensity scan was performed by *decreasing* the pressure in the chamber to approximately 10^{-7} Torr, while increasing the power sent into the chamber. Finally, a high-intensity scan is performed at roughly 10^{-8} Torr, with much higher intensities in the interaction region. By combining the data from all three scans, we exceed the effective dynamic range of our detection system. The intensity ranges and fill pressures corresponding to Fig. 4.2 are summarized in Table 4.1. We remark that in order for our method of stitching scans to be viable, there must be continuity between the separate scans. We preserve linearity between separate scans by keeping all experimental parameters identical across all three scans, aside from the fill pressure. Therefore, the only physical difference between the separate

scans are the number of neutrals in the interaction region. As long as nonlinearities are not present, the resulting signal will scale linearally with respect to the number of neutrals present inside the focal volume.

We avoid space-charge in our scans by checking for broadening in the ion signals in the TOF spectra at both extreme points of each separate scan. This is done before each scan is started by checking the TOF signal at the lowest and highest intensities of each individual scan. If space-charge occurs, it is seen as a broadening in the ion signal in the TOF spectra. When this happens, the pressure in the chamber is adjusted until space-charge does not occur at the highest intensities. More information on how the scans were stitched together are discussed in §3.6.3 on pg. 70 of this document.

4.2 Absolute Intensity Calibration

Absolute intensity calibrations were performed on each data set by fitting the experimental ion yield curve to overlap with the corresponding PPT calculation for the same ion. This calibration can only be extended to scans taken at the same time as the intensity calibration was performed; additional scans of different species must be calibrated according to the corresponding PPT calculation of the noble gas atom present in the pair being studied. This is an improvement over what has been done in the past [9, 10], where the intensity calibration was performed on Ar^+ using ADK, which was applied to all the other scans presented (O_2^+/Xe^+, CO^+/Kr^+ for instance). As discussed in §2.2.3, we recall that ADK is a simplified version of PPT, in which static rates are derived in the *tunneling* regime. While ADK is far less complicated to implement into calculations, the price paid is inaccurate rates in the MPI regime at low intensities. By fitting our experimental yields to theory which is more accurate over the entire range of intensities, we are able to perform a much more accurate intensity calibration.

We also remark that it is not possible to calibrate our Ar^+ to theory and apply this calibration factor across all data collected in this work. The reason for this is because each data set was taken weeks apart, where the experimental conditions are certain to have changed. To quantify this, we recall that the intensity depends critically on three independent variables according to $I_0 \sim \frac{E_n}{\tau \cdot w_0^2}$. The

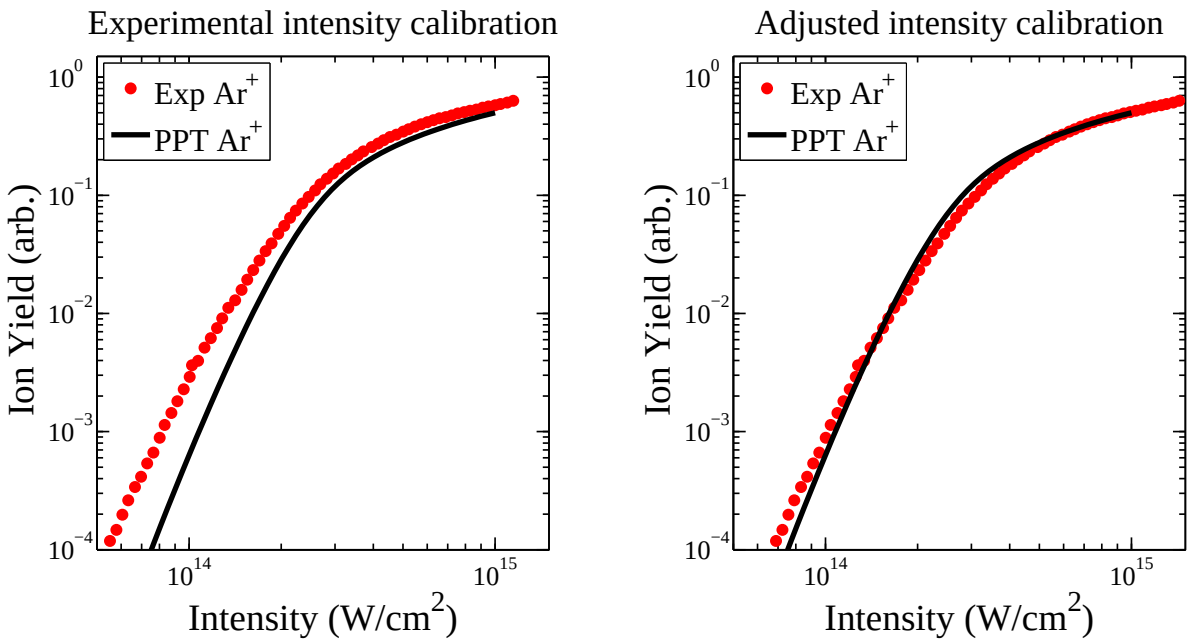

(a) Without absolute intensity calibration

(b) With absolute intensity calibration

Figure 4.3: *An example of how the absolute intensity calibration is performed in this work for the Ar^+ ion curve. In (a), we have the experimentally determined intensity calibration plotted against a PPT calculation for the same ion. We shift our experimental ion yields to coincide with the theoretical curve by multiplying the peak intensity I_0 by a constant shift factor (in this case we multiplied our I_0 by a factor of* 1.25*). Our calibrated data points then coincide with the theory in the intensity scale, as seen in (b).*

pulse energy and pulse duration (E_n and τ, respectively) is a function of the current laser conditions, which may change if the oscillator loses mode-locking, or if the amplifier is tuned, or the current status of the Ti:Sapph crystal in the amplifier (which suffers from damage on a regular basis). The focusing area, w_0^2, is a sensitive function of the focusing conditions. A major contributing factor influencing the focusing geometry lies in the fact that the alignment had to be readjusted from scratch at the beginning of each run, as our optics could not remain on the optical table due to the apparatus being shared across several groups. The consequence of this is that the focusing conditions for each run will vary, resulting in a slightly different intensity. For this reason, the absolute intensity calibration is performed by scaling the energy axis of the experimental data to the space-averaged theoretical yields for each atom.

The calibration factor is found by multiplying the experimentally determined intensity values by

a constant, the value of which is evaluated by minimizing the difference between the experimental and theoretical atomic ion curves in the vicinity of the change in slope that characterizes intensity scans taken over a large range of energies (see Fig. 4.3). This is in contrast with other works [9, 10], in which the absolute intensity calibration was performed by matching the last data point with the ADK calculations for the Ar^+ ion. Performing this sort of calibration is problematic for several reasons. First, we note that ADK is a tunneling theory, and therefore it is most accurate for intensity values corresponding values of $\gamma \ll 1$. Furthermore, in previous works [9, 10], saturation occurs near $\gamma \simeq 1$, which is far from the condition $\gamma \ll 1$. Even though $\gamma < 1$ at the highest intensities, it is not *significantly* less than 1, which is a requirement in order for a process to be considered as purely in the tunneling regime. Furthermore, the slope of ion curves asymptotically approaches a constant value of $I_0^{3/2}$ at the high intensity regions. This change in slope marks the onset of the saturation of the single-ionization process, which is a consequence of the experimental conditions, rather than the core physics. Therefore, performing an intensity calibration by matching the most intense data point to an ADK calculation is not ideal.

We conclude that an absolute intensity calibration is best performed using a theoretical calculation which is generally applicable over the entire intensity range, rather than just at high intensities. For this reason, we chose to do our calibration with PPT, rather than ADK. In fact, we see a rather consistent intensity shift present in the work of [9] when compared to our work, which will be presented in the following sections. In this work, we see that the intensities are up-shifted when compared to both our experimental and theoretical results. This is easily seen in the yield curves for each species, as well as the ratios. The implications of this will be discussed in the following sections.

4.3 Results

In order to compare our experimental results to theoretical calculations, we recall that the ionization yields are a sensitive function of spatial and temporal variations that the distribution of target species experiences at the interaction region. As long as we account for our experimental configuration in our theoretical models, we can minimize these differences. We also remark that our experimental

apparatus, a VMI-TOFMS, does *not* use an extraction pinhole, and so the detector "sees" ions being produced from a distribution of laser intensities. This effect can be minimized by using a looser focusing geometry, which can be provided by using a focusing element with a larger focal length. Unfortunately, this sort of modification was not possible in our VMI-TOFMS, due to the lack of control the experimenter had over the apparatus. However, it is also possible to account for the effects that spatial variations in the laser intensity has on our data by including intensity averaging into theoretical models, as performed in the theory presented in this chapter.

Specifically, the yield, or *signal*, can be expressed as $S = \iint N(I(r,z))\, r\mathrm{d}r\mathrm{d}z$, where $N(I)$ is the fraction of neutral atoms ionized, which is the key quantity which we want to obtain. Recovering this quantity is difficult, as $N(I)$ is inside the integral. We have taken steps to attempt to address this issue by making careful measurements of the parameters used to calibrate the intensity.

4.3.1 N_2/Ar Results

In comparing our experimentally determined N_2^+/Ar^+ yields to theory, the PPT calculation for Ar^+ matches quite well with our results, as can be seen in Fig. 4.4(a)*. In the high-intensity region, above saturation ($> 3 \times 10^{14}$ W/cm^2), the asymptotic limits for both experiment and theory are in good agreement. We also observe qualitative agreement in the low-intensity limit for the experimental Ar^+ curve versus the PPT calculation for the same ion. At the lowest intensities, our experimental data has a multi-photon order (See discussions on MPI in §1.2.1, specifically Fig. 1.4 on pg. 11) of $n = 5$, while for the accompanying theory over the same intensity range yields $n = 6$. However, we remark that even at the lowest intensities in our experimental data, we are not in the pure MPI regime, quantified by the criteria $\gamma \gg 1$. We cannot reach such low intensities, where the multi-photon order is equal to the minimum number of photons required to raise the bound electron to the continuum. Therefore, the slope in this region is not a true indicator of the multi-photon order in the MPI regime, which is reflected in the fact that the number of photons absorbed in our data is less than that expected for a pure MPI process, where $n = 11$ 790 nm photons are needed to ionize

*We recall that in performing our absolute intensity calibration, we shifted our experimental intensity scale to coincide with the theoretical calculations (see §4.2). Here, we are simply commenting on the *shape* of the yield curve, which is unaffected by our intensity calibration.

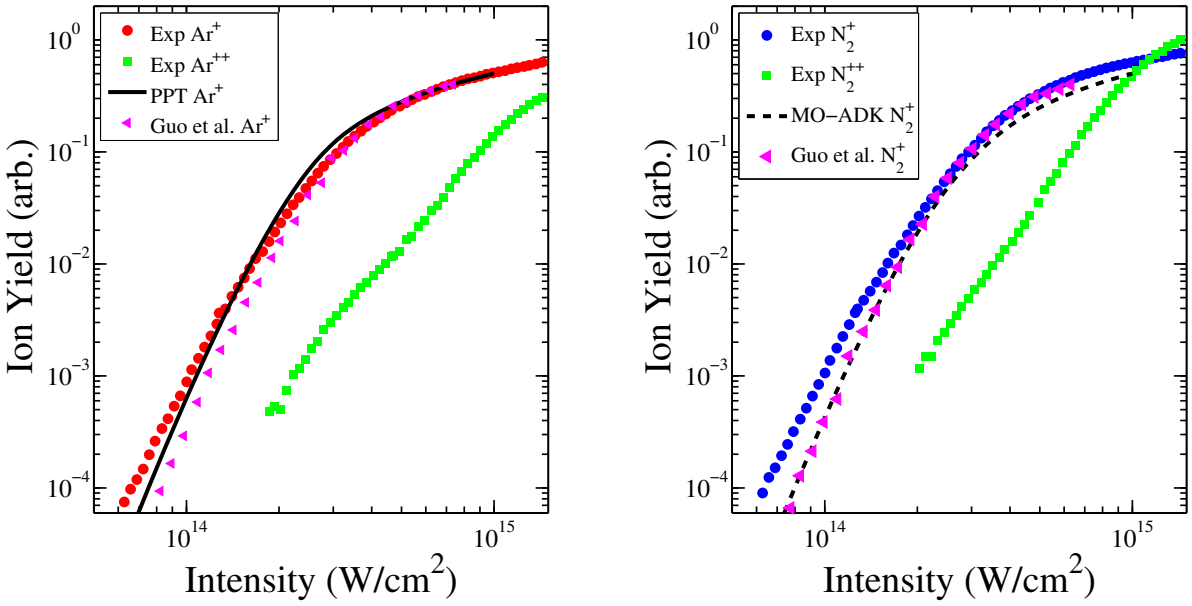

(a) Experimental $Ar^{+/++}$ curves with PPT

(b) Experimental $N_2^{+/++}$ curves with MO-ADK

Figure 4.4: *Intensity-dependent ion yield for $Ar^{+/++}$ and $N_2^{+/++}$ with PPT and MO-ADK theory, respectively. Referenced literature from Guo* et al. *[9]. All experimental and theoretical data corresponds to a pulse duration of $\tau = 30$ fs.*

for both N_2 and Ar. Nevertheless, our experimental data suggests that the ion yields reflect the ionization rate at the intensity where the data was taken.

In comparing our experimental N_2^+ yield to the MO-ADK calculation from Fig. 4.4(b), we see that the theory underestimates the experimentally determined yield across the entire intensity range, especially at intensities less than 2×10^{14} W/cm^2. This is not all that surprising, as others have had similar discrepancies with their N_2^+ yields being larger than the companion Ar^+ yield [9–11]. Furthermore, we recall that MO-ADK is a modified tunneling theory, meaning that it is most applicable at *higher* intensities where $\gamma < 1$. Therefore, it is not unexpected that when $\gamma > 1$, that MO-ADK will be less reliable.

In the yields for both N_2^{++} and Ar^{++} from Figs. 4.4(b) and 4.4(a), respectively, we see some interesting qualitative features deserving of some discussion. In Fig. 4.4(a), we see that for the Ar^{++} yield that there is a change in slope in the vicinity of 5×10^{14} W/cm^2, which is often called the "knee" (see discussions in §1.3, in particular Fig. 1.4 on pg. 11), which marks the transition

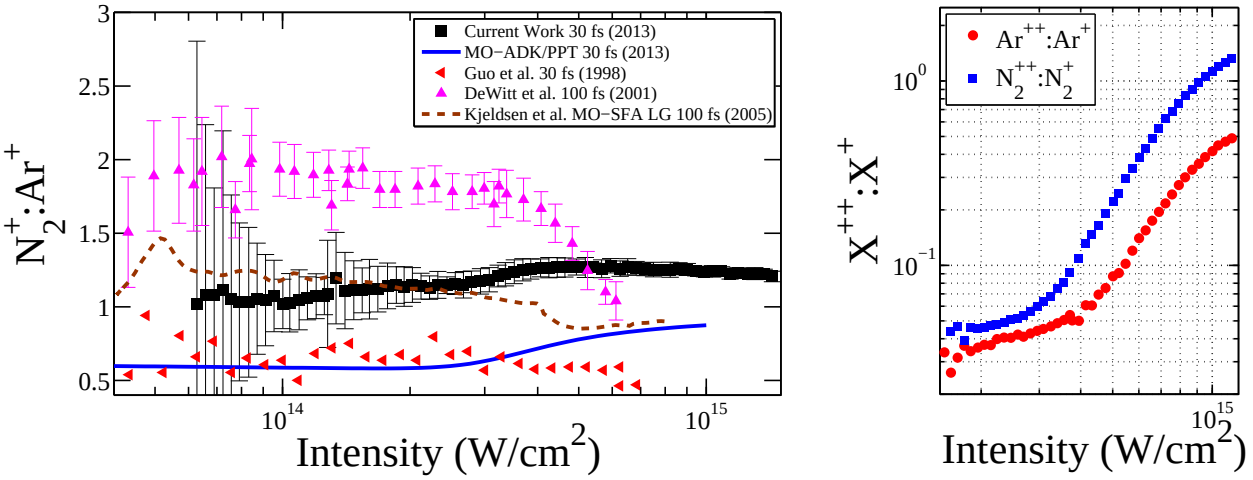

(a) Molecular/atomic ratio plot with literature

(b) Doubly to singly charged ion ratios

Figure 4.5: *Ratio plots for the N_2/Ar pair. Our ratio plot from (a) is plotted versus both experimental and theoretical results from the literature [9–11]. In (b) we have plotted the ratio of X^{++}:X^{+}, where X represents N_2 and Ar. The cut-off intensity from (b) is given by $I_x = 4 \times 10^{14}$ W/cm^2, which is derived from the N_2^{++}:N^{+} curve at the same intensity.*

from the NSDI to the SDI regime [18, 19]. In the N_2^{++} yield from Fig. 4.4(b), we see a similar behavior below the knee that we saw in the Ar^{++} yield, in that both ions appear to increase at approximately the same intensity. After 6×10^{14} W/cm^2, however we see some peculiar behavior in the doubly charged ion for molecular Nitrogen. In particular, we also see a knee-like structure similar to that which is present in the doubly charged Argon ion, however for N_2^{++}, it seems as though the yield in the SDI regime is increasing rapidly with intensity than with the atomic ion. We were particularly surprised to see find the N_2^{++} yield surpassing the N_2^{+} yield, occurring past 10^{15} W/cm^2 in Fig. 4.4(b). We postulate that this enhancement may have several contributing factors. Part of this may be explained by the limited resolution of our detection system. Our time-of-flight mass spectrometer separates ions of **different** values of m/q; however, in the case of molecular Nitrogen, at high intensities dissociation starts to play a non-negligible role in the total detected yield in the doubly charged N_2^{++} curve. Unfortunately, we are unable to separate N_2^{++} with N^{+}, since they share the same value of $m/q = 14$. Therefore, at large intensities (where dissociation plays a non-negligible role), the N_2^{++} signal overlaps with the N^{+} signal, and the detected yield is therefore a linear combination of the two yields. This is further complicated by the fact that

each fragment has a different detection sensitivity, where we recall that the efficiency scales like $\varepsilon \sim q/m^{1/2}$ (see discussions in §3.4.3 on pg. 62). While we do apply corrections for the relative detection sensitivity of each ion, we are unable to do so effectively if the ion signal is a convolution of two ion fragments, each associated with a different efficiency of ε. Furthermore, as we can see from Table 3.3 on pg. 61, in fact the third charge state of Argon has a similar flight time to both N_2^{++} and N^+, and in fact, the Ar^+ ion is also convoluted with the other ions. While the third charge state of Argon only occurs at high intensities (and only becomes appreciable when the first charge state is completely saturated), we recognize that the cutoff value evaluated from Fig. 4.5(b) to be $I_x = 4 \times 10^{14}$ W/cm^2 is appropriate, as at this intensity the N_2^{++} yield from Fig. 4.4(b) is well below the N_2^+ yield, which is what we expect.

We now make some comments about our N_2^+ :Ar^+ ratio. The fact that our experimental N_2^+ yields are *larger* than the the MO-ADK calculation, which is reflected in our ratios from Fig. 4.5(a), where the MO-ADK/PPT calculation for N_2^+/Ar^+ is *less* than unity over the entire intensity range, while our data is *over* unity. This is a regular inconsistency across all intensity ranges in our yields for N_2^+/Ar^+, and is discussed in §4.4 on pg. 94.

At the higher intensities for N_2^+:Ar^+ in Fig. 4.5(a) beyond saturation ($> 4 \times 10^{14}$ W/cm^2), our data tends to agree with the theoretical calculations, but diverges from previous experiments performed under similar conditions. In particular, Dewitt *et al.* [10] shows a reverse behavior above saturation when compared with our results. Specifically, the results from Dewitt *et al.* inflects *downwards*, while ours inflects *upwards*. This is not surprising, since for intensities beyond saturation, this experiment does not produce useful results for the singly charged ions. In fact, the ionization rate should increase past saturation at the same rate for both species, meaning that the slope of the ratio should approach a constant value. This feature is reflected in our data, but there seems to be a degree of divergence when inspecting the results from the literature. In particular, a downward inflecting ratio implies that the atomic ion continues to increase while the molecular ion saturates. This is *not* reflected in other experimental works presented in Fig. 4.5(a), but matches theory. The discrepancy between our results and experimental data from the literature may in part be attributed to our experimental arrangement, as we observe a similar behavior at extremely high intensities ($> 7 \times 10^{14}$ W/cm^2), although not to the same degree present in Dewitt *et al.* [10]. We

cannot make similar comparisons with the work of Guo *et al.* [9], as their data does not seem to clearly indicate any measurable change in slope in the higher intensity regions due to lack of convergence.

4.3.2 O_2/Xe Results

Our experimental Xe^+ yield curve agrees qualitatively with the theoretical calculations at both high and low intensities, as can be seen in Fig. 4.6(a). As we saw with the other noble gas species studied in this work, ion yields derived from PPT are in good agreement with experiment. However, as we saw in the other companion molecules, there is a clear departure between the MO-ADK yield and experiment for the O_2^+ molecular ion, as shown in Fig. 4.6(b). Specifically, we note that there is a discrepancy in the absolute yield of the molecular ion with respect to theory. In particular, we see that the shape of the MO-ADK O_2^+ curve appears to fit better with our data at the *higher* intensities than at the *lower* intensities. This suggests that the ionization rate calculated underestimates the molecular yield at the lowest intensities, as observed for our N_2/Ar data presented in the last section. However, we note that the slope of the ion yields at low intensities is in good agreement with our experimental results.

Our O_2^+/Xe^+ ratio agrees qualitatively with the literature, both in experiment and theory, as can be seen in Fig. 4.7(a) [9–11, 94]. The best agreement between our experimental results and experiments from the literature are from Guo *et al.* [9], where they also used a 30 fs pulse. However, as we remarked previously, it appears as though the intensity for both molecular and atomic species are up-shifted in intensity, which we partially attribute to the fact that they used ADK to provide absolute intensity calibration. If we shift Guo's yields to coincide with our intensity calibration, our O_2^+/Xe^+ is in qualitative agreement.

In addition, we also notice the magnitude of the ratio starts at 0.05, as opposed to a value of 1.2 in our N_2^+/Ar^+ plot from Fig. 4.5(a). This is a common feature in all results cited in the figure; this anomalous behavior is reflected in the study of *ionization suppression*, which will be discussed in detail in the next section. The presence of ionization suppression is verified in our measurements, which is an area of intense interest in the ultra-fast community [32, 94–97].

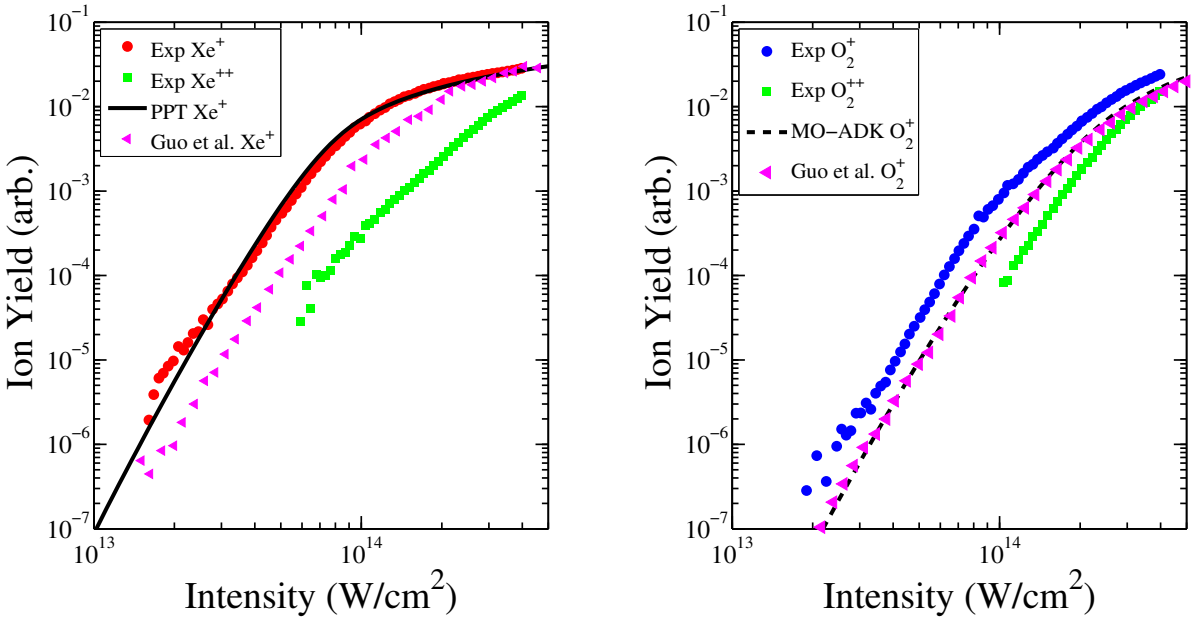

(a) Experimental $Xe^{+/++}$ curves with PPT

(b) Experimental $O_2^{+/++}$ curves with MO-ADK

Figure 4.6: *Intensity-dependent ion yield for $Xe^{+/++}$ and $O_2^{+/++}$ with PPT and MO-ADK theory, respectively. Referenced literature from Guo* et al. *[9]. All experimental and theoretical data corresponds to a pulse duration of $\tau = 30$ fs.*

Ionization Suppression

Ionization suppression occurs when the ionization rate of *molecules* is significantly lower than that of *atoms*, both having nearly the same ionization potential. This feature is present in our O_2^+:Xe^+ ratio plot from Fig. 4.7(a), and is consistent with the literature, while such effects are absent in our N_2^+:Ar^+ ratio from Fig. 4.5(a). According to quasi-static tunneling theories, ionization rates are dictated by the field and the ionization potential. Therefore, it is unsurprising that when N_2^+, with an I_p of 15.58 eV, was found to match the ionization of Ar^+, having an I_p of 15.76 eV. However, when comparing Xe^+ ($I_p = 12.13$ eV) with O_2^+ ($I_p = 12.06$ eV), the ion yield of O_2 was suppressed by about an order of magnitude [94]. This then begs the question: what causes ionization suppression to occur in O_2^+:Xe^+, but not N_2^+:Ar^+?

This question has been the subject of intense interest within the ultrafast community [32, 94–97], and the answer continues to evolve to this day. In 1996, Talebpour *et al.* [94] associates

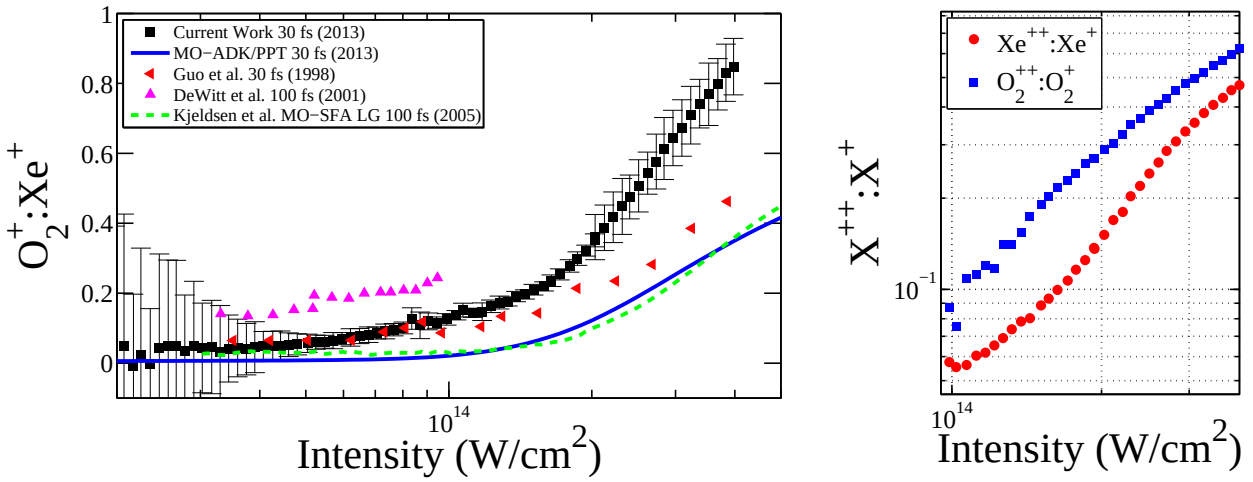

(a) Molecular/atomic ratio plot with literature

(b) Doubly to singly charged ion ratios

Figure 4.7: *Ratio plots for the O_2/Xe pair. Our ratio plot from (a) is plotted versus both experimental and theoretical results from the literature [9–11, 94]. In (b) we have plotted the ratio of X^{++}:X^+, where X represents O_2 and Xe. The cut-off intensity from (b) is given by $I_x = 1 \times 10^{14}$ W/cm^2, which is derived from the O_2^{++}:O^+ curve at the same intensity.*

the suppression in O_2^+ with respect to Xe^+ to be caused by dissociative recombination through rescattering. Dissociative recombination occurs when an excited O_2 molecule decays into two fragments (*e.g.* $O + O$, $O^+ + O$), causing a reduction in the total yield of the O_2^+ signal. He further asserts that the alternating electric field may produce an electron which is driven back to collide with the parent ion. In this context, dissociative recombination refers to the process where an electron collides with a molecular ion and forms a neutral neutral molecule in a doubly excited state [94]. A few years later, Guo *et al.* [9, 95] mentions that all rescattering phenomena exhibit a strong dependence of the polarization of the incident beam; he showed that by using an elliptically polarized beam, that suppression in the O_2^+ signal was still present, and therefore determined that dissociative recombination through rescattering was unlikely to be the cause of the reduced signal.

In 2000, Muth-Böhm *et al.* [32] suggested that the multi-core nature of diatomic molecules may explain the suppression of O_2^+ due to quantum interference. He attributes the effects which this phenomena have on the molecule, comparing it to the constructive/destructive action produced in a typical double-slit experiment, where the width of the slit is the internuclear axis. The simultaneous emission of electrons from both atomic centers produces interference, which is *constructive* when

Table 4.2: *Ground-state wave functions and Highest Occupied Molecular Orbital (HOMO) for all molecules studied in this work.*

Species	Ψ_{gs}	HOMO
N_2	$^1\Sigma_g^+$	σ_g
CO	$^1\Sigma^+$	σ_g
O_2	$^3\Sigma_g^-$	π_g

the electrons are emitted perfectly in phase, and *destructive* when they are exactly out of phase. The degree to which this affect becomes appreciable depends on the symmetry of the molecule being ionized. A listing of the groun-state wave functions for all molecules presented here can be seen in Table 4.2. In particular, with molecules with symmetric electronic ground-state wave functions, the interference is constructive, and the ionization occurs as though it were from a single atomic center. If, on the other hand, the molecule has an antisymmetric ground state electronic wave function, then the interference is destructive, which acts to suppress the ionization. This theory explains the suppression in O_2^+ and its absence in N_2^+.

Many groups have further studied this effect [98, 99], and the conclusion they reached was that this interference pattern behaves differently, the extent to which this occurs depends on the symmetry of the ground-state wave function for the molecule. The ground-state wave function of all molecules studied in this work can be seen in Table 4.2.

Finally, in 2008, Ren *et al.* [100] provided analysis which agrees with Muth-Böhm's results. Indeed, he concludes that ionization suppression in the O_2^+ signal is induced by destructive interference induced by the multi-core nature of the molecule. He also notes that the degree to which his SFA implementation of his theory depends on the gauge which is used in the calculation. In particular, he found that this interference picture is only valid in length-gauge formulations of the MO-SFA theory.

4.3.3 CO/Kr Results

Here we discuss the CO/Kr pair, which contains the only heteronuclear diatomic molecule studied in this work. The yield curves for both Kr^+ and CO^+ can be seen in Figs. 4.8(a) and 4.8(b),

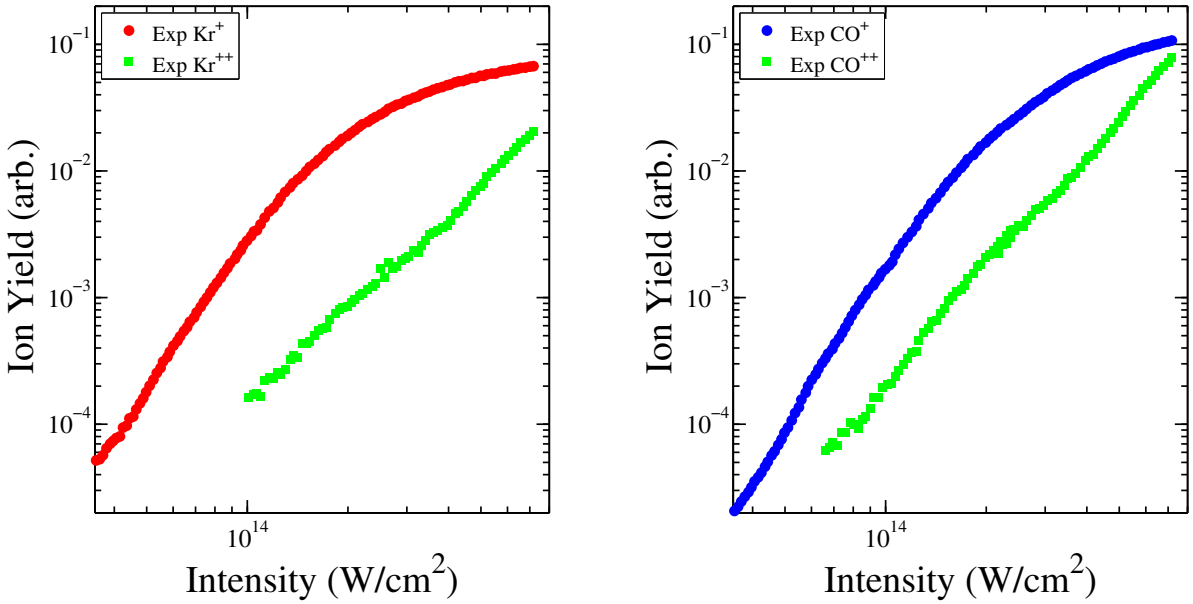

(a) Experimental $Kr^{+/++}$ yield curves

(b) Experimental $CO^{+/++}$ curves

Figure 4.8: *Intensity-dependent ion yield for $Kr^{+/++}$ and $CO^{+/++}$.*

respectively, which exhibit interesting behaviors at the low intensity regions. In particular, we notice that below saturation, both CO^+ and Kr^+ curves exhibit independent fluctuations in the yields, which are reflected in the CO^+:Kr^+ plot from Fig. 4.9(a). The result of the relative fluctuations between both curves results in wild fluctuations in the ratio. This is reflected in the literature [93], however there is currently a lack of experimental data which can further quantify this behavior. MO-SFA calculations performed in the velocity gauge [11] produce similar oscillatory effects, however there appears to be a phase offset between the respective peaks and valleys in the oscillatory features in the ratio plots. At this time, we are currently unable to definitely attribute these apparent affects to any specific mechanism.

We also remark that the cutoff intensity is found from 4.9(b) to be $I_x = 1 \times 10^{14}$ W/cm^2, meaning that at intensities greater than this value, the singly charged states for both the molecule and atom begin to become depleted. We also remark on the absence of theory for the CO/Kr pair, which was unavailable at the time of writing this thesis. Part of the reason for this is that since CO is a heteronuclear molecule, it poses a more difficult computational problem, and further time is needed

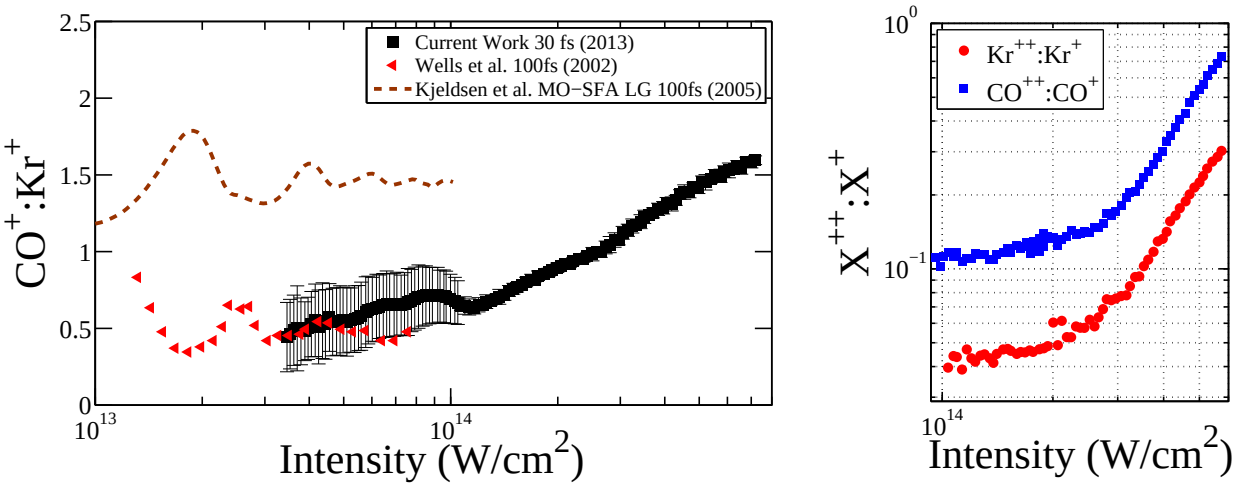

(a) Molecular/atomic ratio plot

(b) Doubly to singly charged ion ratios

Figure 4.9: *Ratio relevant to the CO/Kr pair. Our ratio plot from (a) is plotted versus both experimental [93] and theoretical [11] results from the literature. The cutoff intensity is found from (b) to be* $I_x = 1 \times 10^{14}$ *W/cm*^{2}.

for the theory to be generated. Accordingly, the theory for the Kr^+ ion is also absent, and in fact we were unable to perform an absolute intensity calibration on this pair with the corresponding PPT calculation. In the near future, we hope to obtain this theory.

4.4 Discussion

The work presented here represents an improvement over similar measurements in several respects; foremost is our implementation of power discrimination discussed in §3.2.2, which limits the the magnitude of systematic error present in our final analysis by excluding data points associated with fluctuations in laser intensity. While applying this system to our collected data results in a large amount of rejected data points, we were able to improve our statistics by increasing the number of data points collected during each scan. Additionally, we implemented absolute intensity calibrations based on the PPT model, while other sources in the literature [9, 10] performed calibrations based on the ADK model, which is only reliable at the highest intensities

The ion yields for the atomic species studied in this work are in excellent agreement with PPT calculations, implying that it is possible to use this atomic ionization model may be used as

a benchmark against our data. The ratios of the MO-ADK rates to the PPT rates indicates that MO-ADK is not reliable for the ionization of the molecules studied in this work, and by way of using the PPT rates as a metric against our experimental data points, we believe that our results may be used to improve existing molecular ionization theories.

We also remark on a common feature in comparing all of our yield plots with theoretical calculations, in that there is a slight departure at the lowest intensity range, which is a relatively common inconsistency in these types of scans when compared directly with theory. While our data was collected to maximize the amount of statistics present across the entire intensity range, at low intensities the magnitude of the ion signal is comparable to the background. Even though steps were taken to deconvolute the signal from the background, at the lowest intensities, the ion signal is especially prone to including random time-dependent fluctuations in the integrated area of the TOF spectra, which is responsible for this divergence. Perfect agreement between theory and experiment is unexpected, as theoretical calculations cannot accurately account for the complexity of the actual conditions in the lab. We do note, however, that the theoretical calculations we present in this work are with a localized gas jet, of the same width as used to collect our data. In addition, these calculations take into account the actual spot size at the interaction region, which was measured in a separate experiment, the results of which are discussed in §5.2 on pg. 115.

We also comment on the offset in magnitude that our ratios from Figs. 4.5(a), 4.9(a), and 4.7(a). The magnitude of the ratios determined in our experimental data are dependent on a factor we introduce to correct for the fact that our gas bottles are not mixed at a 50/50 distribution across both species. The value of this correction factor is proportional to the relative pressures of each species inside the gas bottle. This is an inaccurate method of measurement, and in the future we will subject our gas mixtures to a Residual Gas Analyzer (RGA), which will offer a much more accurate value for the partial pressures present in the gas bottles. However, all this will do is *shift* the yields relative to one another; the power of our ratiometric measurement technique is that each of the yields is self-consistent, in that the relative yields between the pair depends only on the relative amount of both species at the interaction region, which can be found via this partial pressure measurement. In fact, this measurement will only act to shift the ratio either up or down; the shape of the intensity-dependent ratio curve will not change. However, this measurement must occur

before meaningful conclusions can be drawn specifically in regards to the magnitude of the ratio with the literature, which in the case of N_2/Ar, ranges from 0.5 to 2, meaning that there is still a great deal of uncertainty in the magnitudes [9, 10, 101].

Chapter 5

Other Experimental Developments

5.1 Femtosecond Pulse-Shaping

A great deal of interest has been focused towards the development of systems which will allow for the generation of complicated optical waveforms. The motivation for pursuing this field is rooted in the fact that pulse shaping provides a very powerful tool for scientists. This section contains a brief introduction to the general concept of pulse shaping, followed by the design of our apparatus. This includes discussions specific to both the physical constraints and practical limitations of the approach we present. This section will end with a discussion of the possible applications of our completed design, as well as the current status of the project.

5.1.1 Introduction to Pulse Shaping

Shaping a pulse in the time domain does not provide a powerful tool for experimentalists; direct manipulation of a temporally dispersed laser pulse over the duration of the laser pulse is unrealistic, as response times of materials are on the order of *micro*seconds (10^{-6} s), while the temporal width of the pulse is measured in *femto*seconds (10^{-15} s). By spreading the information contained with the laser pulse over longer periods of time, it is possible to circumvent this issue; this is achieved by delaying the individual frequencies by way of introducing controlled dispersion to the system from a diffraction grating. When a laser pulse is incident upon such a diffraction grating, the diffracted angle being inversely proportional to the wavelength, as seen in Fig. 5.1. The first diffraction grating,

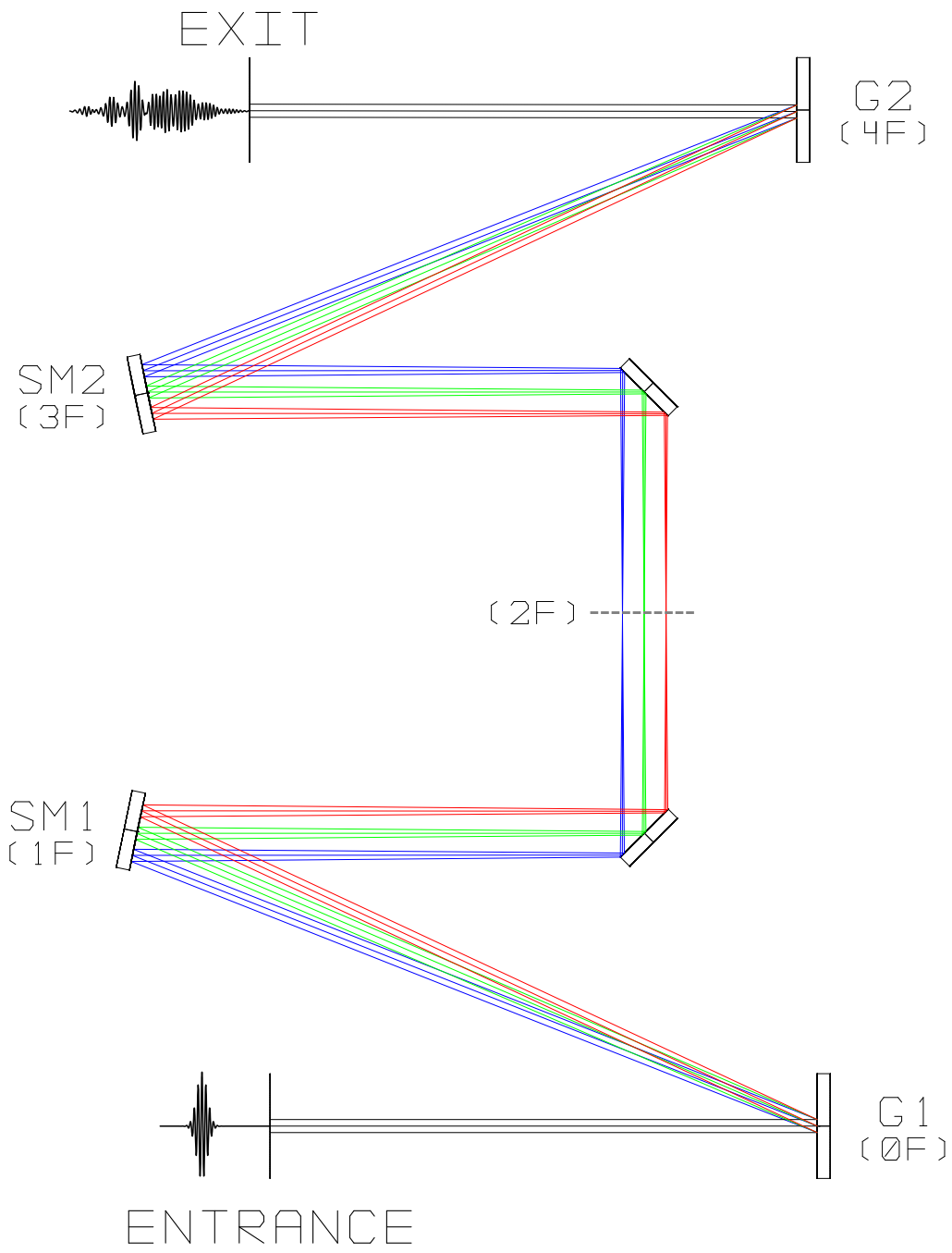

Figure 5.1: *General scheme behind Fourier-plane pulse shaping. The coloring of the dispersed waves represents the corresponding wavelengths. We see that the incident (unshaped) pulse enters the system and hits the first diffraction grating, where the first order diffraction pattern disperses frequencies. The first spherical mirror, SM1, both collimates and focuses the spatially separated frequencies at the Fourier-plane. The active pulse shaping element is placed here, where the frequencies are accessible. The purpose of the rest of the shaper is to recombine the frequencies, resulting in a shaped output pulse at the exit of the apparatus.*

G1, is located at $0f$, where f is the focal length of the focusing element; this also signifies the origin of the shaper. After the first grating, the frequencies are all divergent; the frequencies are then collimated by a focusing element, in our case a spherical mirror (SM1), which is located at $1f$. This element focuses the diverging beam, and converts the angular dispersion from the grating into a spatial separation at the second focal plane. At $2f$, the frequencies are focused separately down to the smallest spot. The active pulse shaping element is always placed at this position (referred to as the *Fourier plane*) so that the individual frequencies can be manipulated, which are both spatially and temporally dispersed. The purpose of the remainder of the optical elements is to recombine the frequency components exactly the same way that they were dispersed. This is done by placing a second *identical* focusing element at $3f$, and a second matched grating finally at $4f$. The final output then contains a femtosecond shaped laser pulse.

It is important to point out that if the active pulse shaping element is removed, that the output pulse must be identical to the input pulse. In this scenario, the pulse shaper will act like a stretcher and compressor pair. The $4f$ condition must be met in order to meet this criteria. For this reason, it is important that the gratings and focusing elements are chosen to minimize the dispersion in the system. It is for this reason that a mirror is preferential to a lens as the focusing element in a pulse shaper. A lens is made of a transmissive optical material, which has a frequency-dependent index of refraction. When a wide-bandwidth laser is used as the source in such a pulse shaper, each frequency component will exhibit a longitudinal defocusing proportional to the wavelength, as depicted in Fig. 5.12(a) on pg. 119. This introduces undesirable dispersion into the final output, reducing the efficacy of the design.

Many methods are available to act as the active element in pulse shapers. In particular methods based on the use of a Liquid-Crystal Mask (LCM) [102, 103] or a Deformable Mirror (DM) [104] are common. Another method involves the use of an Acousto-Optic Modulator (AOM) [105–108]. In AOM based pulse shaping, an oscillating electric signal drives a transducer at one end of the acousto-optic crystal, which acts to convert the time-dependent electrical signal into an acoustic wave (see Fig. 5.2). The sound wave travels across the device, and light passing transversely through the medium is diffracted by the resulting acoustic pattern. The AOM essentially acts as a transmissive grating, in which the acoustic waves produce regions of varying index of refraction that

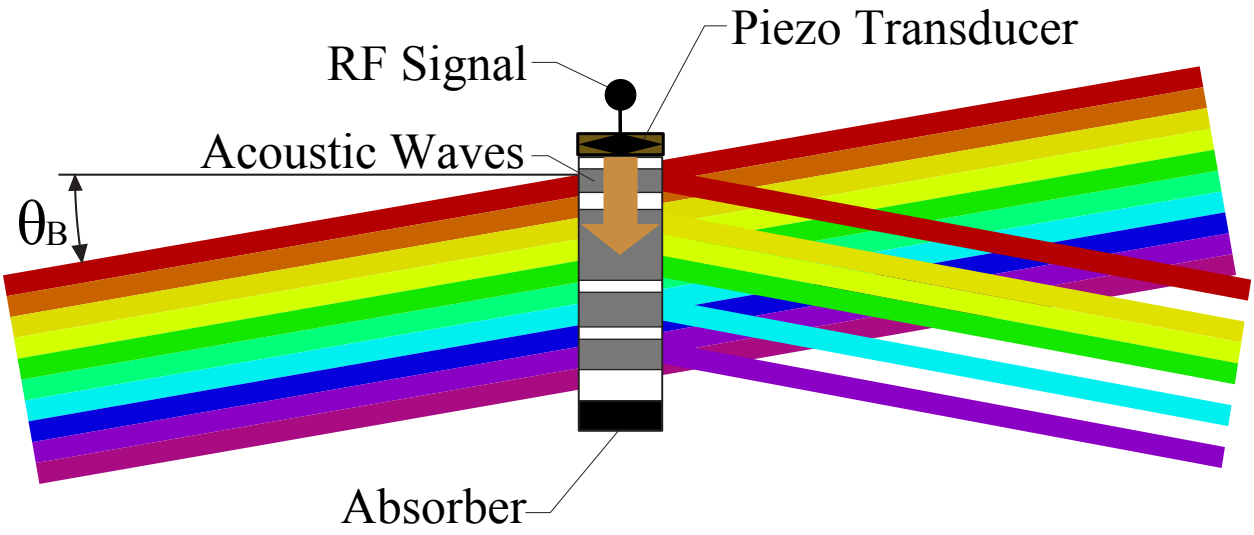

Figure 5.2: *The action of the pulse shaper in producing shaped pulses, demonstrating the basic working principles of our AOM in our pulse shaper. An RF signal is sent to an electro-mechanical actuator, producing acoustic waves through the AOM crystal. The spatially separated frequencies enter the device at the Fourier plane from the left at the Bragg angle* θ_B*, where the diffracted components are selected to constitute the shaped pulse.*

are analogous to the grooves of the conventional grating. Furthermore, as light travels significantly faster than the speed of the acoustic wave in the crystal. Our AOM is comprised by a Tellurium Dioxide (TeO_2) crystal, which has a characteristic acoustic velocity of $v = 4.2 \times 10^3$ m/s [109]. The TeO_2 is chosen due to its material properties, which are characterized by high transmission, low response times, and a large diffraction angle [110], all of which are critical in the optimal operation of our proposed pulse shaper design. Furthermore, the speed of the acoustic wave traveling across the AOM is roughly six orders of magnitude slower than the speed of the light transversing the crystal aperture. Therefore, the frequency components contained within the dispersed laser pulse "see" the stationary waveform created by the acoustic wave.

There are many reasons why an experimenter would choose one method over another. We first remark that AOMs have the ability to simultaneously encode both amplitude and phase information onto a laser pulse. LC arrays have this same ability, provided that they are of the *dual mask* variety; a single mask can only provide phase modulation. On the other hand, LC arrays only have the ability to provide amplitude modulation. However, this lack of versatility is circumvented by the use of a dual-mask LCM. This way, the LCM method of pulse shaping has the same shaping abilities as

an AOM based apparatus.

Because a LCM uses a discrete number of pixels to shape laser pulses, diffraction effects in the final pulse are often present, due to the finite size of the pixels. On the other hand, since AOM devices are not discretized, they lack this affliction. However, even though the acoustic waveform can, in theory, be thought of as a continuously adjustable entity, it too suffers from diffraction. The reason for this has to do with a fundamental limit imposed on the focusing of light waves. In particular, we recall that no beam can be focused down to a size smaller than its wavelength, also known as the diffraction limit. This limit acts to restrict the smallest acoustic feature in the crystal, which is often referred to as an *effective pixel size*. This quantity is defined in terms of the length of the crystal aperture and the minimum acoustic feature size by the following relation [108]:

$$N_p \sim \left(\frac{L_0}{\lambda_0}\right)^{2/3} \Rightarrow \left(\frac{34\times 10^{-3}\ \mathrm{m}}{790\times 10^{-9}\ \mathrm{m}}\right) \sim 1228, \tag{5.1}$$

where N_p is the number of effective pixels, L_0 is the length of the aperture, and λ_0 is the central wavelength of the incident pulse. We see that N_p represents the total resolution of the system, and the quantity evaluated from (5.1) can be used to directly compare the capabilities of AOM shaping versus LCM shaping.

Acousto-optic deflectors also offer much faster programming times compared to with LC arrays. The time required for AOM waveform synthesis is measured in microseconds, whereas the same quantity for LCMs is on the order of milliseconds. On the other hand, a problem with AOM shapers is that the efficiency is small, which is due to the action of the AOM has on the incident pulse. The crystal selectively diffracts the frequencies that are to be contained within the final (shaped) pulse.

We also recognize that in AOM pulse shaping, the action of the AOM is transient, as the acoustic wave changes as a function of time. This implies that the timing of the wave with respect to the repetition rate of the laser must be precisely controlled. Therefore, the desired acoustic waveform to produce a shaped pulse must be repeated at the appropriate intervals. This adds a degree of complexity to the implementation of the design, but does not affect the efficacy of the apparatus [111]. The main benefit is that the action is linear, as discussed in the following section.

5.1.2 Theory

As mentioned in section 5.1.1, the action of the $4f$ pulse shaper on an incident laser pulse is done in the frequency domain, whereas the initial and final pulses are physically realized in the time-domain. It is straightforward to recognize that the first half of the pulse shaper effectively performs a Fourier Transform (FT) on the pulse. The elements that perform the transform consist of a grating/mirror pair. The first pair (G1, SM1 in Fig. 5.1) perform the forward FT, while the second pair performs the reverse FT. We can quantify the action of each grating/mirror pair in the traditional way,

$$\widetilde{E}(\omega) = \frac{1}{\sqrt{2\pi}} \int E(t) e^{-i\omega t}\, \mathrm{d}t$$
$$E(t) = \frac{1}{\sqrt{2\pi}} \int \widetilde{E}(\omega) e^{i\omega t}\, \mathrm{d}\omega.$$

To find the output waveform, we must consider the effect that an AOM has on the incident laser pulse in the frequency domain:

$$\widetilde{E}_{\mathrm{out}} = \widetilde{E}_{\mathrm{in}}(\omega) M(\omega) e^{i\varphi(\omega)}, \tag{5.2}$$

where ϕ is the phase of the acoustic wave, $M(\omega)$ is the frequency dependent mask function, while $E_{\mathrm{out}}(\omega)$ and $E_{\mathrm{in}}(\omega)$ represent the complex amplitude of the output and input fields, respectively. The mask function, $M(\omega)$, is a convolution of the spatial waveform of the laser pulse and the acoustic waveform of the sound wave inside the crystal.

The spectral phase, $\varphi(\omega)$, is modified by manipulating the phase of the acoustic wave about the central RF frequency. The amplitude of the diffracted spectral components is controlled by varying the amplitude of the acoustic wave inside the crystal. The transfer function can be evaluated by mapping the optical spectra of the incident pulse onto the position-space coordinate system of the AOM. The spatial profile of a monochromatic frequency component is assumed to be Gaussian in nature:

$$\mathrm{G}(x - x') = \exp\left[-\frac{2(x-x')^2}{w_0'^2}\right], \tag{5.3}$$

where w_0' is the beam diameter across the crystal. The transfer function is a spatial convolution of the complex acoustic wave $S_{\text{ac}}(x_{\text{ac}})$ and the spatial profile of the frequency component from (5.3):

$$M(x') = \int_{-\infty}^{\infty} S_{\text{ac}}(x) \cdot \text{G}(x - x')\, \text{d}x. \tag{5.4}$$

5.1.3 Design Considerations

To maximize the efficacy of our AOM, we require that the frequency components of the laser beam span the entire length of the crystal aperture. The consequence for not doing so is a reduction in the effective resolution of the AOM. The absolute resolution of the AOM is determined from the relative size of the beam profile with respect to the minimum feature size on the crystal. Therefore, our design must have the most extreme frequencies components are spatially dispersed along the entire length of the crystal (see Fig. 5.3(b)).

Additionally, due to the low damage threshold of the AOM, we must choose our optics and incident beam diameter to have the largest focus spot on the crystal as possible. Recalling that damage thresholds are typically measured in flux/area, for the same amount of flux but for a larger area, the damage threshold will not be reached. To solve this problem, we performed theoretical calculations and simulations to ensure that we can send as much light through the pulse shaper as possible.

At this point we remark that many parts of the design process were evaluated using ZEMAX, a optical design program. ZEMAX performs geometric ray tracing based on the optical properties of the elements within the design. The physical components (mirrors, windows, diffraction gratings, lenses etc) are available in databases within ZEMAX, where the individual parts are provided directly from the respective manufacturer (*e.g.* ThorLabs, CVI, Newport and so on). The program also allows for manufacturer-specific coatings to be applied to all optics available from that particular company.

In addition, ZEMAX provides a wealth of design tools, in particular with respect to tolerancing and optimization. Based on the user-specified constraints of the design, the program iteratively modifies the controllable parameters until an optimal solution is met. ZEMAX also provides many sophisticated analysis features, such as spot diagrams, phase front maps, and Seidel diagrams. This

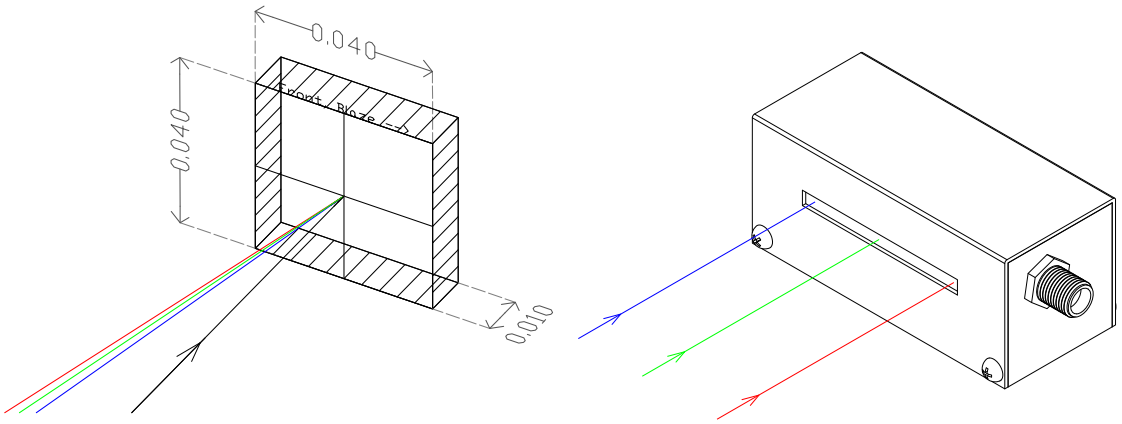

(a) Diffraction Grating (b) Acousto-Optic Modulator

Figure 5.3: *Diffraction Grating and Acousto-Optic Modulator. The diffraction grating from (a) demonstrates the frequency-dependent angular dispersion with respect to the blaze direction (dimensions are in meters). The Acousto-Optic Modulator from (b) is placed at the Fourier plane. The aperture is* 34 *mm wide and* 2 *mm high. The spatially dispersed frequencies span the entire length of the crystal.*

allows the user to keep track of various aberrations throughout the design, such as longitudinal focal shifting and chromatic separations. ZEMAX proved to be particularly useful in the design of our pulse shaper, as it allows for the inclusion of user-specified wavelengths and fields. This way, we can see how various design changes will impact the efficacy of our pulse shaper. The designs created in the program can be directly exported to CAD formats, allowing for direct implementation of optimized designs.

5.1.4 Final Design

Before the design process began, we had already decided upon the use of an AOM as the active pulse shaping element, so this was considered fixed. The manufacturer we purchased the deflector from was the Brimrose, the characteristics of the particular AOM used in our design are listed in Table 5.1. These quantities serve as the basis of the design process for our pulse shaper. For instance, the width of the aperture (34 mm) determines the spatial separation of the outermost frequencies.

Other practical aspects include limited availability of specialized parts. Foremost, diffraction gratings are manufactured in discrete line densities from a single master grating. Going outside this

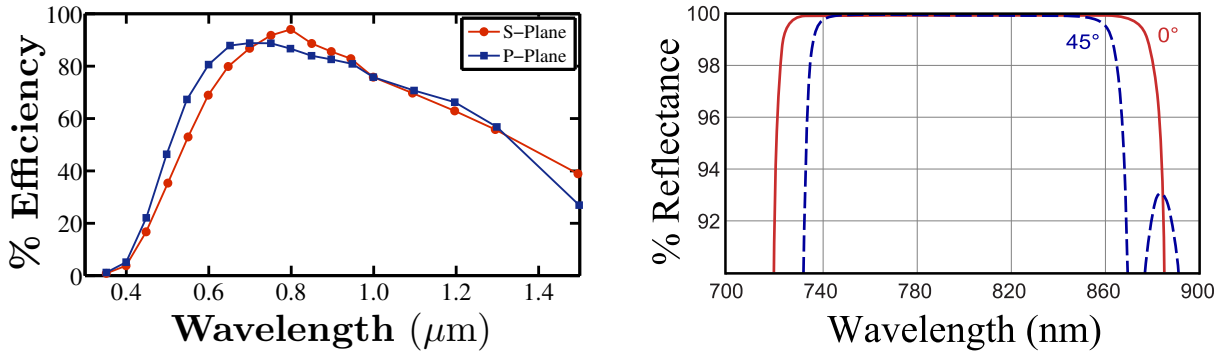

(a) Richardson grating 53-*-790R

(b) TLMB coating from CVI

Figure 5.4: *Efficiency curves for two major components in our final pulse shaper design. (a) is the efficiency curve for the diffraction grating we chose [*`Richardson grating 53-*-790R`*], while (b) is the efficiency for the TLMB coating applied to our spherical mirrors provideds by CVI Melles Griot.*

catalogue would involve getting a new master cast, which is prohibitively expensive. Therefore, it is natural to start our design on the limited availability of gratings that are suitable for our applications. We chose several such gratings to serve as starting points for our design. The better choice, and the one we ended up with in our final design, was the `Newport Richardson 53-*-790R`, which is characterized by $G = 235$ g/mm and is blazed at 5.06° at $\lambda = 750$ nm. All subsequent calculations will use these values, since they are the ones we ended up with in our final design. The efficiency curves for this grating can be seen in Fig. 5.4(a).

A further restriction that we must consider is the limited availability of odd-focal length mirrors. They are offered in discrete focal lengths, *e.g.* $f = 0.5$ m, $f = 1.0$ m, $f = 1.5$ m, $f = 2.0$ m, etc. The reason why we can only get certain focal lengths stems from the fact that we require a special wide-bandwidth coating on the mirrors used in the design. This coating offers uniform reflection across all frequencies used in our design. Not using such a coating in a pulse-shaper design has the consequence of introducing a frequency-dependent discrimination to the reflected beam. The coating that is most suitable for these purposes is the `CVI Melles Griot TLMB ultra-broadband coating`, which was developed especially for these applications in ultrashort laser systems. This all-dielectric coating, centered at 800 nm, minimizes pulse broadening in wide-bandwidth applications. This coating is superior to protected and enhanced metallic coatings

because of its ability to handle higher powers. The efficiency curves for this coating can be seen in Fig. 5.4(b).

So, given that we have only a few suitable diffraction gratings, we start with one grating and evaluate the ideal focal length for a large spot at the Fourier plane for that particular grating. How close this focal length is to those available is our criteria for what set of components we choose in our final design. This procedure begins from the grating equation [112],

$$Gn\lambda = \sin\alpha + \sin\beta, \qquad \text{where} \qquad \begin{aligned} n &= \text{Diffraction Order} \\ G &= \text{Groove density } (10^{-3}\text{ m}) \\ \alpha &= \text{Incident radiation angle} \\ \beta &= \text{Diffracted radiation angle,} \end{aligned}$$

in which positive angles are clockwise of normal incidence (vertical) and negative angles are counter-clockwise. In our case, the diffracted beam β is *negative*, and therefore $n = -1$. The grating equation then becomes

$$G\lambda = \sin\beta - \sin\alpha. \tag{5.5}$$

The grating we chose has a groove density of $\mathbf{G = 235\ g/mm}$ and is blazed at $\mathbf{5.06}^{\circ}$ at a wavelength of **750 nm**. The laser being used has the following characteristics:

$$\begin{aligned} \lambda_0 &= 790\text{ nm} \\ \text{FWHM}(t) &= 30\text{ fs} \\ \text{FWHM}(\lambda) &= 43.3\text{ nm} \\ \sigma_\lambda &= 18.4\text{ nm}. \end{aligned}$$

where σ_λ is the standard deviation of the spectral bandwidth of the laser. We designed the pulse shaper to be capable of accessing frequencies $\pm 3\sigma_\lambda$ away from the central frequency λ_0. These represent an outer limit for the frequencies available to the AOM. Realistically, we will only be accessing frequencies $\pm 2\sigma_\lambda$ away from λ_0, however it has been found experimentally that extreme ends of the crystal have more undesirable shaping abilities than the central region. The wavelengths

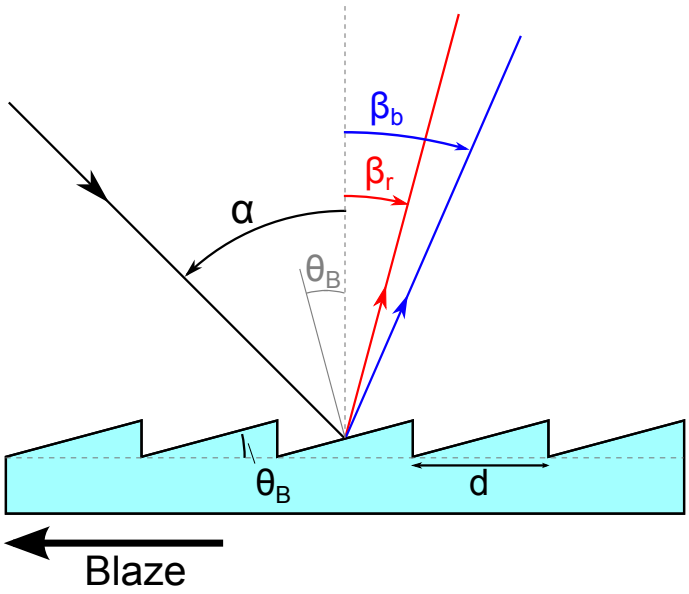

Figure 5.5: *The action of a diffraction grating in producing angularly dispersed diffraction orders. The groove spacing is given by d, while the blaze angle θ_B and direction are indicated, and α is the incident beam angle while β_r and β_b represent the diffracted angles for the red and blue components contained within the incident beam, respectively.*

of our outermost frequencies are evaluated by

$$\lambda_b = \lambda_0 - 3\sigma_\lambda = 734.8 \text{ nm}$$
$$\lambda_r = \lambda_0 + 3\sigma_\lambda = 845.2 \text{ nm},$$

where λ_b is the wavelength of the blue component, and λ_r is the wavelength of the red component. The green component represents the central wavelength λ_0, as depicted in Fig. 5.1. Taking the incident angle $\alpha = 0$, (5.5) becomes

$$G\lambda = \sin\beta \longrightarrow \beta = \sin^{-1}(G\lambda) \tag{5.6}$$

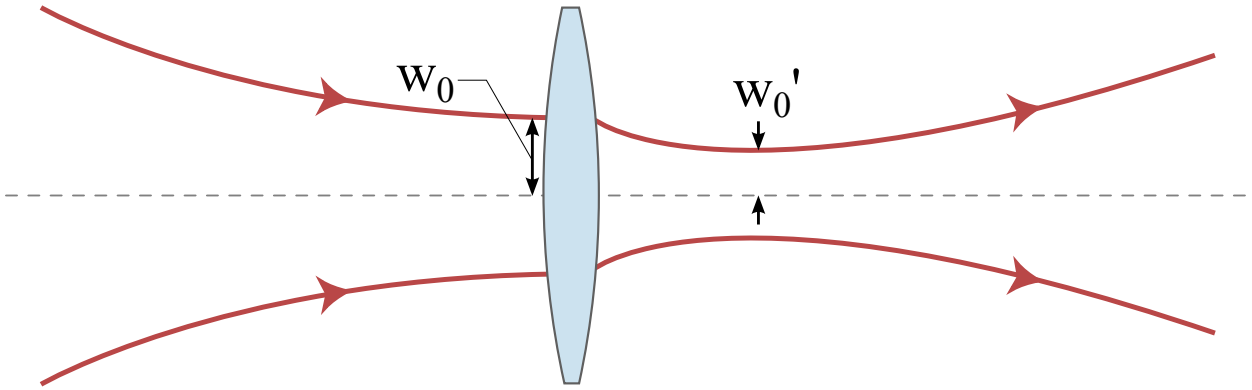

Figure 5.6: *An incident laser having a beam waist of w_0 after focused by a mirror is characterized by an exiting spot size of w_0'. The value of w_0' is related to w_0 by the focal length of the lens.*

To find the dispersion angles for λ_b and λ_r,

$$\begin{aligned}
\beta_b &= \sin^{-1}\left(734.8\text{nm}\cdot\frac{235\text{g}}{10^6\text{nm}}\right) = 9.94^o \\
\beta_0 &= \sin^{-1}\left(790.0\text{nm}\cdot\frac{235\text{g}}{10^6\text{nm}}\right) = 10.70^o \\
\beta_r &= \sin^{-1}\left(845.2\text{nm}\cdot\frac{235\text{g}}{10^6\text{nm}}\right) = 11.46^o \\
\delta &= \beta_r - \beta_b = 3.44^o
\end{aligned}$$

where δ signifies the difference between the two most extreme angles. The dimensions of the AOM used are 34×2 mm, so we wish to associate 34 mm with D the divergence. From this we can now solve for f,

$$D = 2\cdot f\cdot\tan\left(\frac{\delta}{2}\right) \longrightarrow f = \frac{D}{2}\cot\left(\frac{\delta}{2}\right). \tag{5.7}$$

Substituting in the appropriate values into (5.7), we have

$$f = \frac{D}{2}\cot\left(\frac{\delta}{2}\right) = \frac{34\text{ mm}}{2}\cot\left(\frac{0.7123}{2}\right) = 1.29\text{ m}.$$

The closest focal length that CVI offers to this result is $f = 1.5$ m, which is what we went with in our final design. Now that we have the focal length, we continue the design process by doing

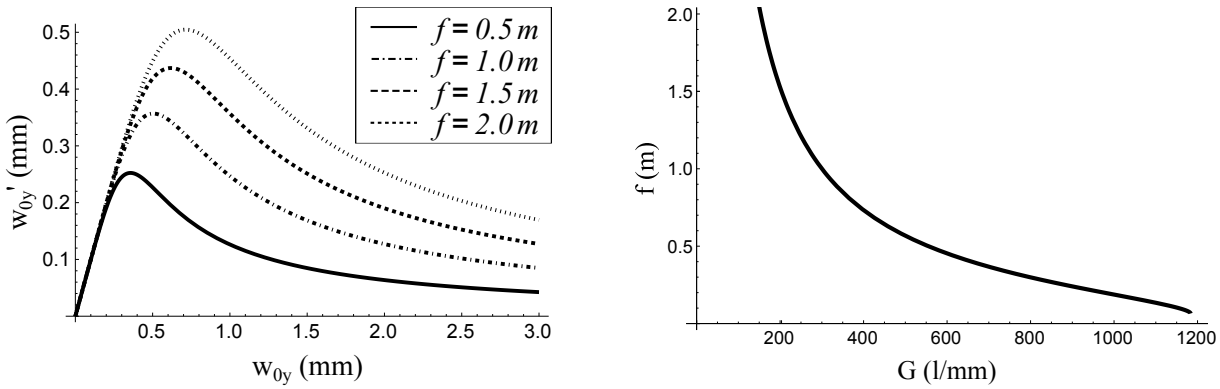

(a) spot size as a function of focal length

(b) Groove density of the diffraction grating as a function of focal length

Figure 5.7: *spot size as a function of focal length as well as the groove density of an arbitrary diffraction grating as a function of focal length. We also note that (a) is a symbolic plot of the function form of* (5.9).

some spot size calculations. We started by recognizing that the grating disperses the frequency components along a single axis, perpendicular to the groove lines in the grating, as can be seen in Fig. 5.3(a). A spherical mirror acts to stop the angular dispersion along this axis by collimating the spatially separated frequencies. The beam profile on the orthogonal axis (in/out of the page in Fig. 5.1) is not affecting by the grating and, therefore, is non-divergent.

As demonstrated in Fig. 5.6, when a divergent beam hits a spherical mirror, the beam tends to collimate; the degree to which this happens is proportional to the focal length of the optic used and is quantified in (5.8). On the other hand, when a beam that is already collimated hits the same mirror, it will focus down to its minimum waist size, w_0. These two processes occur simultaneously after the diffraction grating and before the Fourier plane; the spread axis of the angularly dispersed frequencies is collimated, while the orthogonal axis is focused. Furthermore, the reason why we use spherical mirror as opposed to a cylindrical mirror is because of the restricted dimensions of the aperture of the AOM crystal (See Fig. 5.3(b)); the beam must be focused to fit through the aperture.

We can quantify these arguments by making several calculations in Gaussian optics. We first

Table 5.1: *Summary of the critical parameters for our AOM.*

Wavelength of Operation:	800 ± 100 nm
Optical Power Density:	5 W/mm^2
Center Frequency:	150 MHz
Bandwidth (3 dB):	50 MHz
Active Aperture:	2×34 mm
Access Time:	8 μs
Time-Bandwidth Product:	800
Acoustic Velocity:	4.2×10^3 m/s
Maximum RF Power:	2 W
Optical Transmission:	95%
Peak Diffraction Efficiency:	$\sim 50\%$

recall that the spot size is quantitatively described as [61]

$$w_0' = \frac{\lambda f}{\pi w_0 \sqrt{1 + f^2/Z_R^2}}, \tag{5.8}$$

where f is the focal length of the spherical focusing element, Z_R is the Rayleigh range defined by $Z_R = \pi w_0^2/\lambda$, and w_0 and w_0' are the entrance and exit beam waist, respectively. Substituting Z_R into (5.8) and simplifying, we end up with

$$w_0' = \frac{\lambda f w_0}{\sqrt{(\pi w_0)^2 + (\lambda f)^2}}. \tag{5.9}$$

We can plot (5.9) as a function of focal length as in Fig. 5.7(a), and we see that the exit spot size (w_0') is larger for *longer* focal lengths, which is predicted by Gaussian optics. An interesting feature of this plot is that the exit spot size, w_0', reaches a local maxima as a function of the incident spot size, w_0. Remember that we are interested in creating a large spot size for the focused beam, so it is most preferable to choose the entrance spot size such that the exit spot size is maximized. This quantity can be evaluated for an arbitrary focal length f, by extremizing (5.9):

$$\frac{dw_0'}{dw_0} = 0 \longrightarrow w_0^{(\max)} = \sqrt{\frac{\lambda f}{\pi}}. \tag{5.10}$$

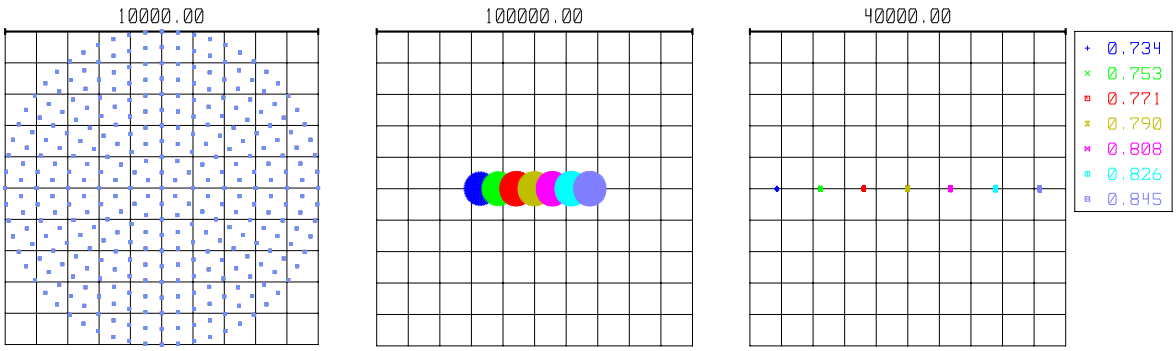

(a) Diffraction gratings at G1/G2

(b) Spherical mirrors at SM1/SM2

(c) AOM at $2f$

Figure 5.8: *A ZEMAX simulation of our pulse shaper design, showing a spot diagram at three critical locations in 5.1. At the surface of the diffraction gratings, the beam consists of all frequencies superimposed with no spatial separation, as is the case in (a). The grating imposes a frequency-dependent response to the initial beam, where each frequency is reflected along a slightly different path, as depicted in (b). At the Fourier plane, the individual frequency components are focused and separated as in (c), where they may be shaped by the AOM. All units are in microns.*

Using (5.10), it is possible to maximize the focusing area by shrinking the incident beam diameter. As we shall see in the next section, it is not realistic to use the optimal spot size by shrinking the beam by an amount equal to the calculated result from (5.10). The reason for this is that this value for w_0 results in an incident beam width of ~ 2 mm, which may result in damaging the diffraction gratings in the shaper since at this point the beam is not dispersed. In reality, a compromise must be reached between w_0 and w_0', which is generally not determined by (5.10).

A spot diagram generated by ZEMAX with our final design parameters in particular vindicates the efficacy of our design. In particular, by looking at the spot diagrams at each of the optical elements is provided in Fig. 5.8. Here we see the pulse shaper dispersing the frequency components, and focusing them finally at the Fourier plane.

A CAD drawing can be seen in Fig. 5.9. This figure shows the key dimensions relevant to the construction of the apparatus. The three different colored rays represent the corresponding frequency components referenced throughout this chapter (blue = λ_b, green = λ_0, and red = λ_r). Many of the physical parameters in our final design are summarized in Fig. 5.9.

The curved mirrors used in the final design [`CVI TLMB-800-0-2037-3.00CC-S25.0`] have a focal length of $f = 1.5$ m, and are coated with the TLMB ultra-high broadband dielectric coat-

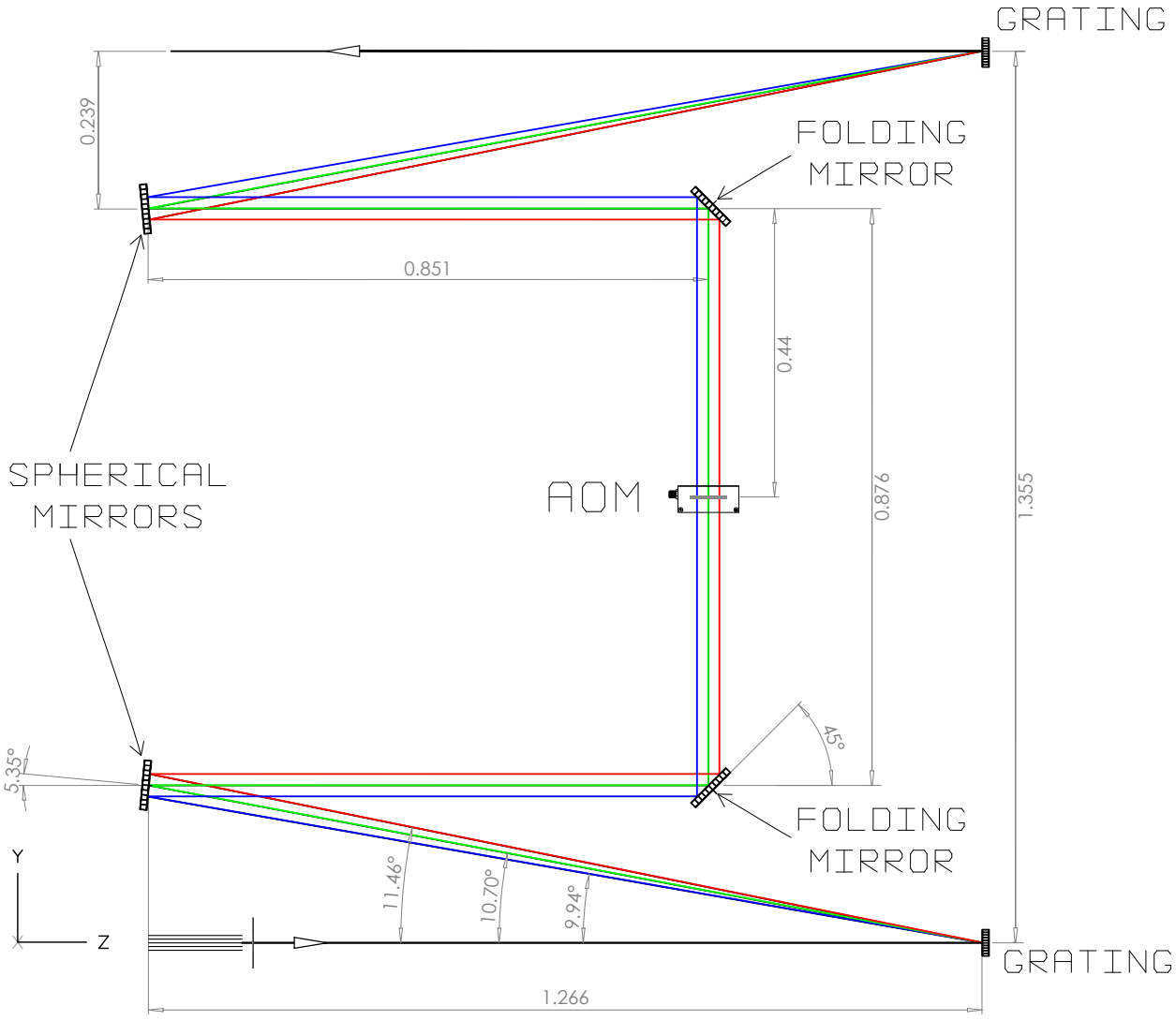

Figure 5.9: *Component layout / dimensional drawing of the pulse shaper. Different colors used to indicate respective frequency components. In this diagram there are three rays, each color corresponding to the respective wavelength they represent. They represent the most extreme frequencies the pulse shaper was designed for. Distances measured in meters.*

ing. The characteristics of the AOM used [`Brimrose TED8-150-50-800/2mm`] were summarized in Table 5.1 on pg. 110. The matched set of diffraction gratings used [`Newport Richardson 53009BK01-790R`] are characterized by a groove density 235 G/mm, and is blazed at 5.06^{o} at 750 nm.

5.1.5 Current Status & Outlook

As of Spring 2013, the device has been built, but further work is needed before it can be used in experiments. The next step is to create a genetic algorithm, which is interfaced to the acousto-optic deflector. After this is done, the final step is to test and calibrate the apparatus.

[This page intentionally left blank]

5.2 Laser Beam Characterization

The laser focus presents a considerable complication for studying high-intensity phenomena. Ideally, we would like to observe the effect of a single intensity, but we can only reach intensities of interest by focusing. Our target therefore sees a spatially-varying peak intensity, and our measured signal is then a sum of the ionization events occurring at all intensities present in the focus. However, intensity calibrations are performed based on the peak intensity, I_0. In particular,

$$I_0 = \frac{4E_n}{\pi w_0^2 \tau}\sqrt{\frac{\ln 2}{\pi}}, \tag{5.11}$$

where E_n is the pulse energy, w_0 is the minimum spot size, and τ represents the pulse duration. Therefore, in order to perform an accurate intensity calibration, it is crucial that the focal volume is characterized according to the minimum spot size w_0. The purpose of this section is to provide details on the measurements we took to estimate this value.

5.2.1 Introduction & Theory

The *Rayleigh range*, which is defined as the longitudinal distance over which the minimum waist size w_0 increases by a factor of $\sqrt{2}$ (see Fig. 5.11(a)), and is defined by:

$$Z_R = \frac{\pi w_0^2}{\lambda}. \tag{5.12}$$

According to (5.12), Z_R can be found if w_0 is known since λ is fixed. Furthermore, the beam waist at an arbitrary z is found by:

$$w(z) = w_0\sqrt{1 + z^2/Z_R^2}. \tag{5.13}$$

Substituting (5.12) into (5.13), we arrive at

$$w(z) = w_0\sqrt{1 + \left(\frac{z\lambda}{\pi w_0^2}\right)^2}. \tag{5.14}$$

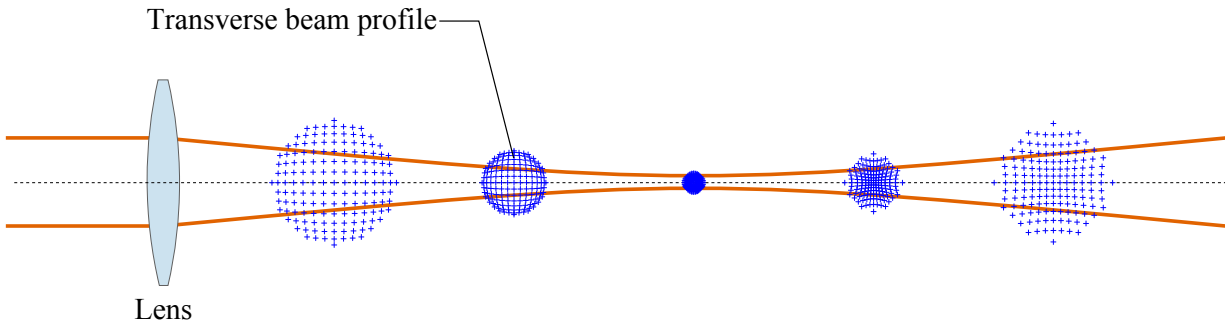

Figure 5.10: *The focusing of a Gaussian beam. This demonstrates the propagation of the beam and also the beam profile at various points after the lens.*

We note that (5.14) is a 2$^{\text{nd}}$-order polynomial; plotting this equation leads to the upper-half of the focused ray from Fig. 5.11(a).

The beam width has multiple definitions [113, 114], each of which depends on the statistical reference the measurement is taken with respect to. The diameter of a beam can be quantified by the Full-Width at Half Maximum (FWHM), which is defined as the full width of the beam at half of the maximum intensity. Another standard is with respect to the $1/e^2$ point, which is defined as 13.5% of the maximum intensity. Other definitions include the D4σ, also referred to as the second moment, and is 4 times the standard deviation of the spatial distribution. Some of the main quantities in Gaussian optics are summarized in Table 5.2.

We also remark that it is possible to make a theoretical calculation of the spot size of our focused beam. In particular [115],

$$w_0 = \frac{4M^2\lambda f}{\pi D} \tag{5.15}$$

Table 5.2: *Summary of some of the key results from Gaussian optics.*

Rayleigh Range:	$Z_{\text{R}} = \pi w_0^2/\lambda$
Beam Waist:	$w(z) = w_0\sqrt{1+z^2/Z_{\text{R}}^2}$
Radius of Curvature:	$R(z) = z(1+Z_{\text{R}}^2/z^2)$
Divergence Angle:	$\Theta = \lambda/\pi w_0$
Guoy Phase:	$\phi(z) = \tan^{-1}(z/Z_{\text{R}})$

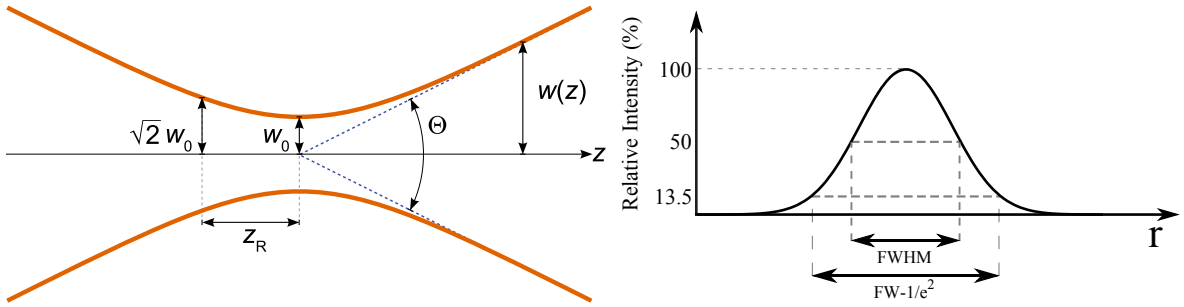

(a) Propagation of a Gaussian beam

(b) Beam width definitions

Figure 5.11: *(a) quantifies the propagation of Gaussian beams, showing the key parameters which determines the focusing of Gaussian laser beams. (b) shows a Gaussian profile with two common definitions of beam diameter.*

where f is the focal length, and D is the e^{-2} beam diameter. The propagation factor, M^2 also referred to as the *beam quality parameter* [116–118], is the ratio of the physical beam divergence to the diffraction-limited beam of the same waist diameter, where for a perfect measurement, $M^2 = 1$, This parameter is often used to assess the quality of beam propagation through an optical system. We can evaluate (5.15) for our experimental arrangement, in which $\lambda = 790$ nm, $f = 7.5$ cm, and $D = 1.0$ cm while letting M^2=1 yields $w_0 = 7.54\ \mu$m.

There are many reasons why we shouldn't use the value for w_0 predicted by theory from (5.15). This equation is for a single-mode Gaussian beam; therefore, any calculated value for w_0 represents a lower limit to the quantity to be measured in our experiment. In reality there are a myriad of experimental factors which will affect the quality of the focusing. Foremost are contributions due to an imperfect beam profile, as well as general misalignment. The beam profile out of the KLS amplifier is asymmetric; the beam is taller than it is wide. According to (5.14) and (5.15), the size of the minimum waist size is dependent upon the incident beam diameter. More specifically, the larger the initial beam waist, the smaller the focus. For KLS, which has a beam profile that is larger in the vertical direction and smaller in the horizontal direction, the minimum spot size in the vertical direction will be smaller than in the horizontal direction. This leads to an *astigmatic beam*, as depicted in Fig. 5.12(c). An astigmatic beam not only has a different waist sizes for both projections of the beam profile, but the position of minimum focus is shifted for each. This, to say the least, represents an undesirable effect on the focal volume at the interaction region. However,

this problem is not easily fixed, and this gives further motivation for independently measuring this quantity, rather than using a value predicted by theory.

Further divergences from theory to experiment include effects due to both *chromatic aberrations* as well as *spherical aberrations*, as depicted in Fig. 5.12(a) and 5.12(b), respectively. Chromatic aberrations are caused by the frequency-dependent response of transmissive optical materials. Each frequency component in the incident laser pulse will see a different index of refraction of any transmissive optic, and so each frequency will refract through the medium along slightly different paths. This causes a broad distribution of focal positions. While the use of transmissive optics is minimized wherever possible to counterbalance this effect, some cannot be removed. For instance, in our experiment the intensity modulation is provided by a half-wave plate followed by a polarizing beams-splitter. The polarizer is 1" thick, and so we must take our spot size measurement with these components placed before the focusing mirror (as was the case in our actual experiment).

Additionally, contributions due to spherical aberrations must also be considered. This aberration is described by a longitudinal defocusing, which depends on how far away from the central axis the beam hits the mirror. While our beam diameter is only 1 cm, this effect still acts to increase the detected spot size. This issue is typically circumvented by using a parabolic mirror. This type of mirror is described by a concave focusing surface, where the outermost rays on the mirror are focused less sharply than the rays closer to the central axis. However, since our experimental arrangement had a spherical mirror, it is essential that we take the measurement to reflect our experimental setup. To quantify the affect that spherical aberrations have on the focal area, it is important that we take this measurement.

5.2.2 Experimental Design

The general idea behind the measurement of w_0 is as follows. We place a CMOS camera [`Mightex SME-B050-U`] on a motorized translational stage [`Micos LS-65`], having a uni-directional repeatability of 0.3 μm. The stage is positioned to be perfectly parallel to the beam propagation axis; this way, the position of the beam will not move as a function of the stage position. The next step is to scan the camera through the focused beam, taking an image at each step. The images produced

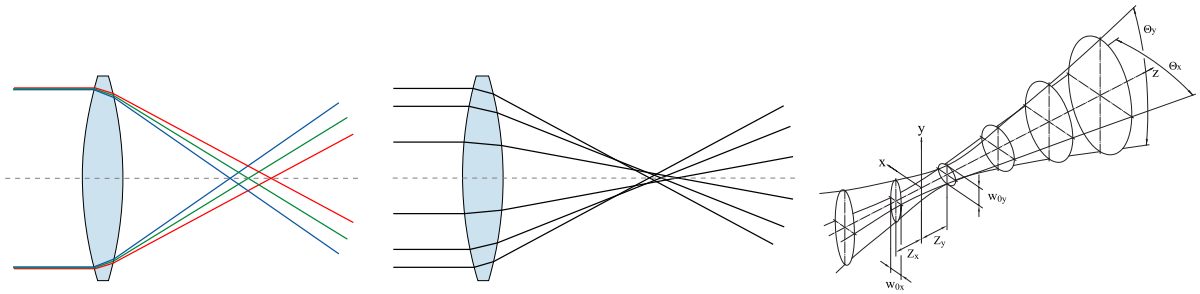

(a) Chromatic aberration (b) Spherical aberration (c) The effect of an astigmatic beam

Figure 5.12: *Different types of aberrations that must be considered for these experiments.*

by the camera represent a direct measurement of the beam profile at that particular position along the z-axis. The image is then read in to the analysis program, where the data points are projected along both the x and y-axes. These projections, which are Gaussian in nature, are fit with a Gaussian profile. The parameters of the fit determine the beam waist, amplitude and centroid position. This is done for both vertical and horizontal projections. This fitting routine is repeated for each of the images taken by the camera, each being taken at a particular z-position. The waist from each of these fits is plotted as a function of the stage position. We then perform a 2^{nd}-order polynomial fit, which has a functional form of (5.14). From the fit, we can then extract w_0, and therefore Z_{R}.

There is a specific reason why we choose to get our value for w_0 from the fit rather than from a direct measurement. The reason for this is due to the lack of statistics our measurement has in the smallest spot. In particular, the approximate size of w_0 is $10-15\mu$m, whereas the pixel size of our camera is 2.2μm. Therefore, by simply moving the camera to the position of the minimum spot, the measurement will yield a statistically inaccurate result. By making several measurements on either side of the minimum spot, we can measure how the beam diverges as a function of propagation, which is well defined by (5.14). Therefore, providing a fit to the data according to this equation is the ideal choice in taking this measurement.

The experimental arrangement of this measurement is shown in Fig. 3.15 on pg. 50. In doing this beam characterization, it is crucial that we take the measurement using the same optics used to gather data in the main experiment. The focusing element in our TOFMS is an on-axis concave spherical mirror with a focal length of $f = 7.5$ cm [`ThorLabs CM254-075-P01`], and this exact

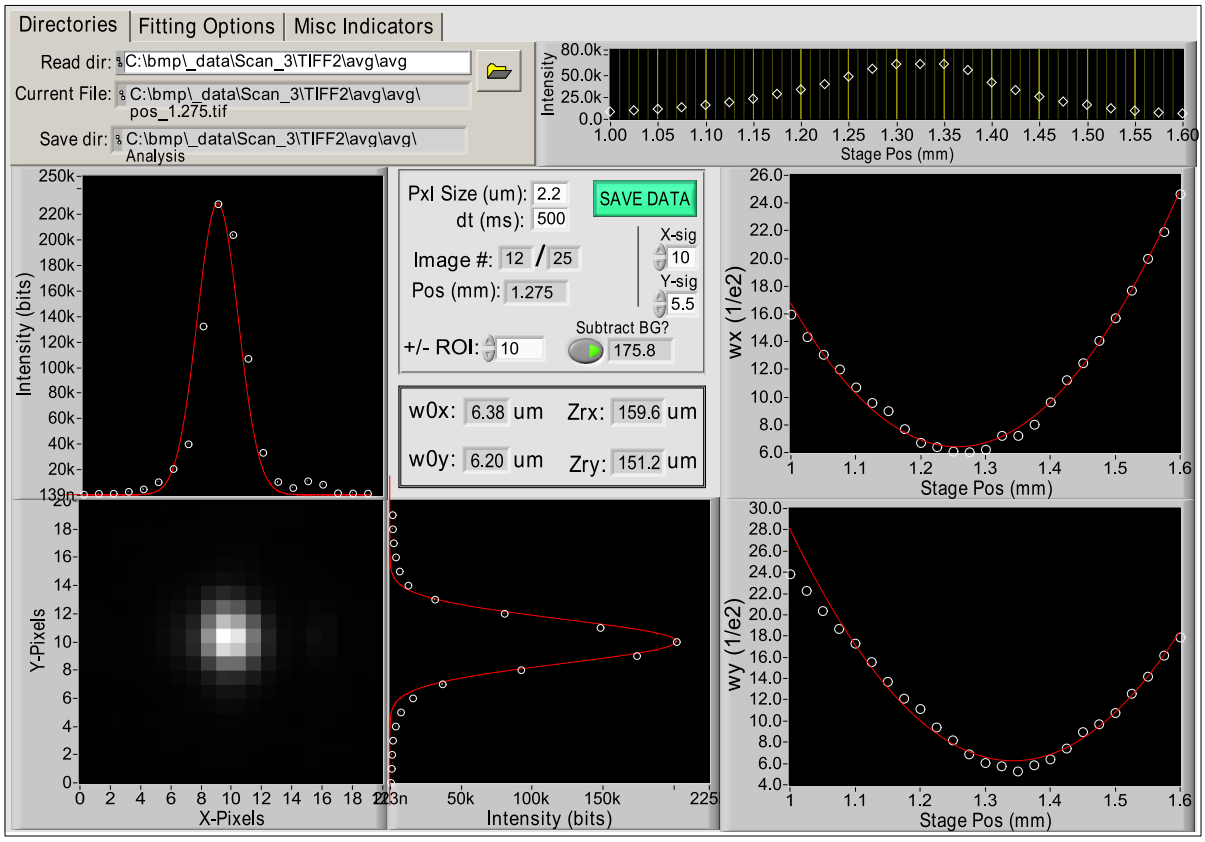

Figure 5.13: *Labview analysis program used for this experiment. The program works by reading in a group of images taken with the CMOS camera from the arrangement shown in Fig. 3.15 on pg. 50 of this document. Each image is read in and plotted, and the image is projected along both the x and y-axes. Each of these projections is fitted with a Gaussian function, and the width of the Gaussian fit for both directions is plotted as a function of the stage position. These data points are then fit with a 2^{nd}-order polynomial of the form in (5.14). From fitting this equation to our experimentally determined data points, we find both w_0 and Z_R.*

optic was used in the spot size measurement. Using a mirror to do a beam profile measurement presents a number of challenges, foremost being that the mirror must be aligned to focus on top of the incident beam. If the camera was placed at this position, then it would certainly block the beam, making the measurement impossible. We solve this issue by picking the reflection off of the focused beam and sending it perpendicular to the incident beam axis. The reflection is picked up off of 1 mm thick BK7 window [`CVI W1-PW-2004-UV-670-1064-0`]. This particular mirror is well-suited for our purposes because it is coated only on one side. The window is oriented such that the AR coating faces the incident beam, while the side closest to the mirror is uncoated. This way,

internal reflections will be minimized. This would be a problem, since if the window was uncoated on both sides, at the plane of the camera, instead of a single spot from the first reflection off the first surface of the window, we will see a second spot corresponding to reflection to the camera from the back surface.

Alignment Procedure

In particular, it is important that the sensor plane must be perfectly perpendicular to the incident beam – otherwise, the measured spot will be larger than the actual spot. This is done by rotating the camera until the spot reaches the smallest possible size. The stage alignment is also checked by looking at the spot and scanning the position. A change in the centroid position as a function of stage position indicates misalignment, and adjustments are made until this no longer occurs.

Because the spot size will be so small, it is crucial that our alignment is done such to minimize all sources of aberrations. We start by placing the HWP and PBS before the experiment using the same alignment procedure discussed in the experimental section. The next step is to place the window, which is mounted on a rotation stage. At first, we align the beam to the window at 0^{o} with respect to the incident beam. We check that this orientation is correct by overlapping the backreflected beam from the window to coincide with the incident beam. We then rotate the stage by exactly 45^{o}. The next step is to place a flat mirror in the place of the spherical mirror in Fig. 3.15 on pg. 50, which is itself mounted on a two-dimensional translational stage. Using these degrees of freedom, we can bring the position of the mirror to the refracted beam transmitted through the window.

Because of the high-bandwidth nature of the laser source used in this experiment, we need to be aware of how the index of refraction of the window changes as a function of frequency and how that will affect the transmitted beam through the window. When the window is rotated to be oriented 45^{o} with respect to the incident beam, refraction will inevitably cause the beam to shift. The degree to which this frequency-dependent shift occurs can be quantified using the Sellemier equation, which

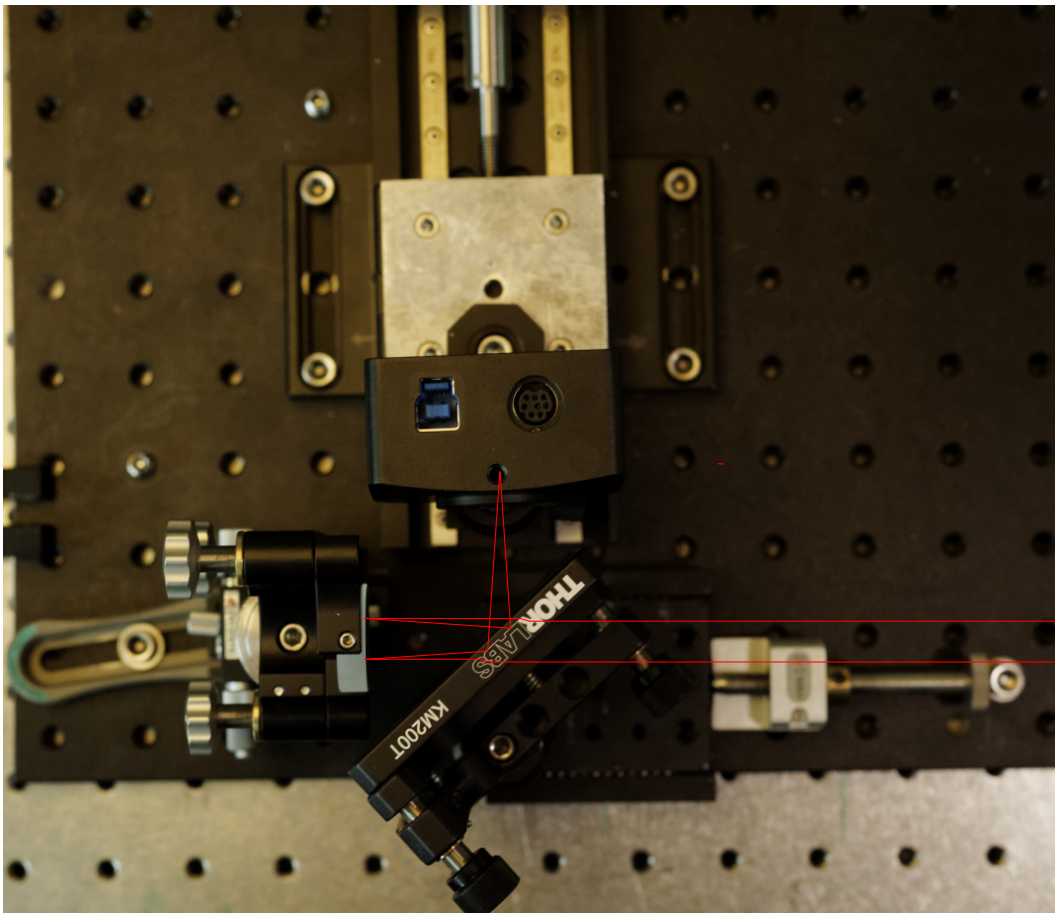

Figure 5.14: *Photo of our final experimental setup. This is the realization of our theoretical design presented in Fig. 3.15 on pg. 50 of this document. The thin red lines indicate the path taken by beam as it passes through the experiment.*

gives the index of refraction as a function of material and wavelength as:

$$n(\text{BK7}, \lambda = 754 \text{ nm}) = 1.512$$

$$n(\text{BK7}, \lambda = 790 \text{ nm}) = 1.511$$

$$n(\text{BK7}, \lambda = 845 \text{ nm}) = 1.510$$

It is clear that the frequency-dependent shift need not be considered, as a difference in the index or refraction by a tenth of a percent is not something that can be measured in our experiment. We must consider, however, the entire shift of the beam, which *is* important. Using Snell's Law, we find that the angle of refraction of a laser centered at $\lambda = 790$ nm inside a 1 mm thick window oriented at

45^o is $\theta = 27.92^o$. This results in the beam being shifted by 1.13 mm. By shifting the transverse linear stage for the mirror by this amount, we can compensate for this effect.

The beam is then reflected from the flat mirror onto the properly oriented window, where $\sim 4\%$ of the beam is reflected perpendicularly from the incident beam axis. It is very important that this reflection will be oriented perfectly perpendicular to the incident beam axis. We verify this by placing an iris in place of the camera mounted on the translational stage. By moving the stage from its closest position (near-field) to its furthest position (far-field), we can make adjustments to the beamline to ensure the beam is parallel to the axis of the stage. The far-field adjustment is achieved by adjusting the window, while the near-field is controlled by the stages beneath the mirror. Scanning the stage from end to end we achieve optical alignment through this iterative procedure.

Once the system is aligned, we replace the flat mirror with the concave mirror. The iris is removed from the stage, and replaced by the camera. We then reduce the intensity of the beam, and sending, it to the imaging sensor, repeating the near and far-field adjustments, using the CMOS sensor as the imaging plane. Using imaging software, we image the spot on the sensor, and make further adjustments to the beamline as needed.

Image Processing

Before the data is extracted from our images, we process the images carefully. When a digital camera makes an exposure, the imaging chip (CCD or CMOS) detects the amount of light that hits each pixel, which is then recorded as an analogue voltage level. The camera's analog to digital circuitry now changes this analog voltage signal into a digital signal. If the camera records 12-bits of data, then each pixel can interpret 4,096 brightness levels (2^{12}). However, if the image type is JPEG or BMP, then the camera will only record 256 brightness levels. The impact that these levels have on the total possible tones present in the image are presented in the Table 5.3. Our camera uses

Table 5.3: *Comparison of the total possible colors produced from two different bit-depths.*

Sensor Bit-Depth	Tones per Channel per Pixel	Total Possible Tones
8-bit	256	16.78 million
12-bit	4,095	68.68 billion

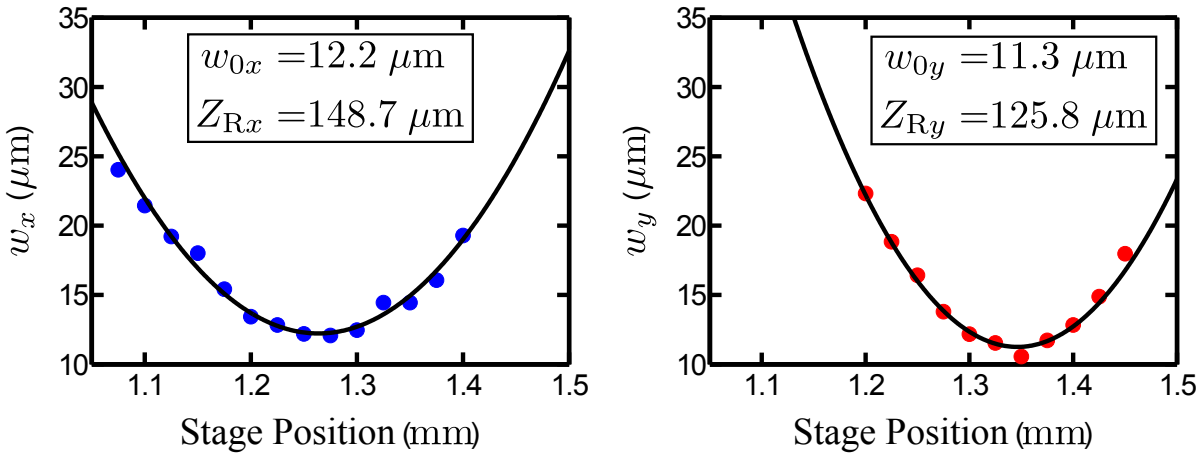

(a) X-projection

(b) Y-projection

Figure 5.15: *The main results from our spot size experiment. In particular, we see that our spot is astigmatic, which we recognize from the minimum spot for the x and y directions occur at different locations.*

a 12-bit sensor, and we saved our images as RAW pixel data. RAW files are then post-processed, where they are finally saved as TIFFs. At the time of data acquisition, at each step a total of 10 images are taken instantly; the post-processing consists only of averaging the images from each step together. The program we used to post-process our images was ImageJ, where each image is exported as a 16-bit TIFFs, and is read in to our analysis program.

5.2.3 Results & Conclusions

Our main results from this measurement can be seen in Fig. 5.15, where the corresponding values for w_0 and Z_R are subset into each figure. An important feature from these results is immediately obvious: both w_0 and Z_R are different for each projection. As mentioned at the beginning of this section, this is not at all unexpected. In particular, we recall that the profile from KLS is asymmetric, the vertical ($\hat{y}$) direction being longer than the horizontal ($\hat{x}$). From (5.14), it is clear that an increased entrance beam size results in a *smaller* minimum waist size. This is reflected in Fig. 5.15(b), as the minimum waist size for the y-projection is $w_{0y} = 11.25\,\mu$m, whereas for the x-projection we have $w_{0x} = 12.23\,\mu$m.

We can also plot the images obtained from both the minimum waist position ($z = 0$) and also

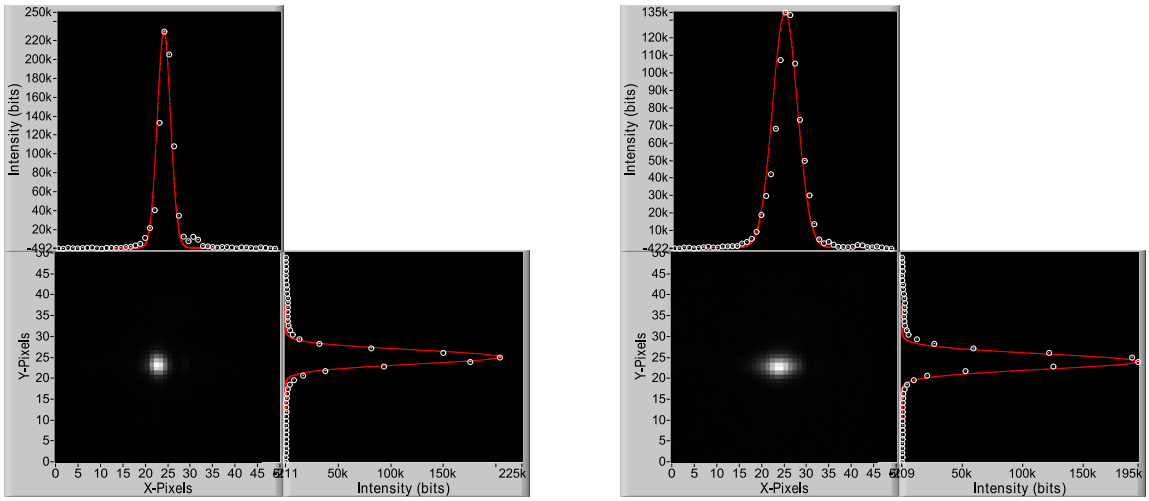

(a) Image taken at $z = 0$

(b) Image taken at $z = Z_R$

Figure 5.16: *Images Fitting parameters for the minimum spot size and also at the Rayleigh range. The astigmatic nature of the beam used in this work is clear by looking at the projected profiles for each image.*

at one Rayleigh range away from this position ($z = Z_R$). These images are shown in Fig. 5.16. In particular, in Fig. 5.16(b), it is very clear that the x-projection at this position is much more spread out than the y-projection of the same image. This is due to the different Rayleigh ranges associated with each axis. The image in Fig. 5.16(b) is taken at the closest directly measured data point.

In conclusion, we recognize that while this technique is very powerful, it is not perfect, even though special care was taken to make the measurement as accurate as possible. We are confident that the values obtained accurately represent the physical characteristics of the beam inside our chamber.

[This page intentionally left blank]

Chapter 6

Conclusions

In this work, we have successfully provided high-quality data over a wide intensity range for three molecule/atom pairs. Our technique of measuring both species simultaneously and taking the ratio is powerful, as it factors out common experimental uncertainties. We believe that our results are reliable, as a high degree of control over the experimental conditions were achieved, as discussed in Chapter 3. Specifically, we implemented a system of power discrimination, which, in addition to the inclusion of power-locking to the KLS amplifier, we were able to reduce effects caused by laser instability in our experimental results. We also performed a meticulous experimental intensity calibration, with special attention towards measuring the focal area of our laser. Furthermore, as discussed at length in Chapter 4, the absolute intensity calibration performed using PPT on our data marks an improvement over similar works, where ADK was used instead.

We believe that our simultaneous measurements indicate a pure indication of the unique ionization dynamics between the molecule and atom. Furthermore, since PPT is in excellent agreement with our *atomic* ion yields, our ratios provide a crucial test for current *molecular* ionization models. Due to the discrepancies between our experimental ratios when compared with those generated by theory, we conclude that current molecular ionization models are deficient, and we suggest that modifications to these theories are needed before an accurate model of molecular ionization is considered reliable. It is our sincere hope that our results can be used to improve these theories, allowing for a greater understanding of the basic principles driving strong-field molecular processes.

6.1 Future Work & Outlook

The collected results presented in §4.3 constitute a complete set of data, which may be used by theorists to development more accurate models for molecular ionization. While we believe that the data in its current form is sufficient to initiate the modification of molecular ionization theories, in the near future, we hope to produce a more accurate measurement of the partial pressures inside the mixed gas bottles, providing a correction to the magnitude of our ratios, which will be performed using a *residual gas analyzer*, as discussed in §4.4. Further studied may be extended from this work may prove useful, such as performing the same set of data with an aligned ensemble of target molecules.

.

Bibliography

[1] L. D. Landau, E. Lifshitz, J. Sykes, J. Bell, and M. Rose, Physics Today **11**, 56 (1958).

[2] L. Keldysh, Zh. Eksperim. i Teor. Fiz. **47** (1964).

[3] A. Perelomov, V. Popov, and M. TerentŠev, Sov. Phys. JETP **23**, 924 (1966).

[4] M. V. Ammosov, N. B. Delone, and V. P. Krainov, Sov. Phys. JETP **64**, 1191 (1986).

[5] P. Agostini, F. Fabre, G. Mainfray, G. Petite, and N. K. Rahman, Phys. Rev. Lett. **42**, 1127 (1979).

[6] A. McPherson et al., JOSA B **4**, 595 (1987).

[7] H. G. Muller and F. C. Kooiman, Phys. Rev. Lett. **81**, 1207 (1998).

[8] A. Becker, L. Plaja, P. Moreno, M. Nurhuda, and F. H. M. Faisal, Phys. Rev. A **64**, 023408 (2001).

[9] C. Guo, M. Li, J. Nibarger, and G. N. Gibson, Physical Review A **58**, R4271 (1998).

[10] M. J. DeWitt, E. Wells, and R. Jones, Physical review letters **87**, 153001 (2001).

[11] T. K. Kjeldsen and L. B. Madsen, Phys. Rev. A **71**, 023411 (2005).

[12] P. Hansch, M. Walker, and L. Van Woerkom, Physical Review A **54**, R2559 (1996).

[13] J. Wu, H. Zeng, and C. Guo, Physical review letters **96**, 243002 (2006).

[14] D. J. Griffiths, *Introduction to quantum mechanics*, Pearson Prentice Hall Upper Saddle River, NJ, 2005.

[15] C. Cohen-Tannoudji, B. Diu, and F. Laloë, *Quantum Mechanics Volume 2*, Hermann, 1977.

[16] B. Walker et al., Physical review letters **73**, 1227 (1994).

[17] A. l'Huillier, L. Lompre, G. Mainfray, and C. Manus, Physical Review A **27**, 2503 (1983).

[18] A. Becker and F. Faisal, Laser Physics **8**, 69 (1998).

[19] J. Watson, A. Sanpera, D. Lappas, P. Knight, and K. Burnett, Physical review letters **78**, 1884 (1997).

[20] A. L'Huillier, L. Lompre, G. Mainfray, and C. Manus, Journal de Physique **44**, 1247 (1983).

[21] S. Larochelle, A. Talebpour, and S.-L. Chin, Journal of Physics B: Atomic, Molecular and Optical Physics **31**, 1201 (1998).

[22] J. Chen and C. Nam, Journal of Physics B: Atomic, Molecular and Optical Physics **36**, 1463 (2003).

[23] C. Cornaggia and P. Hering, Phys. Rev. A **62**, 023403 (2000).

[24] C. Guo, M. Li, J. P. Nibarger, and G. N. Gibson, Phys. Rev. A **61**, 033413 (2000).

[25] A. Becker, R. Dörner, and R. Moshammer, Journal of Physics B: Atomic, Molecular and Optical Physics **38**, S753 (2005).

[26] X. Tong, Z. Zhao, and C. Lin, Physical Review A **66**, 033402 (2002).

[27] G. B. Arfken, H. J. Weber, and F. E. Harris, *Mathematical methods for physicists*, Academic press, 2005.

[28] B. M. Karnakov and V. V. P. Krainov, *WKB Approximation in Atomic Physics*, Springer, 2013.

[29] B. Smirnov and M. Chibisov, Sov. Phys. JETP **22**, 23 (1966).

[30] F. Yan-Zhuo, Z. Song-Feng, and Z. Xiao-Xin, Chinese Physics B **21**, 113101 (2012).

[31] D. E. Knuth, Mathematics of Computation **16**, 275 (1962).

[32] J. Muth-Böhm, A. Becker, and F. Faisal, Physical review letters **85**, 2280 (2000).

[33] L. Keldysh, Sov. Phys. JETP **20**, 1307 (1965).

[34] F. H. Faisal, Journal of Physics B: Atomic and Molecular Physics **6**, L89 (1973).

[35] H. R. Reiss, Physical Review A **22**, 1786 (1980).

[36] T. K. Kjeldsen and L. B. Madsen, Journal of Physics B: Atomic, Molecular and Optical Physics **37**, 2033 (2004).

[37] S.-F. Zhao, C. Jin, A.-T. Le, and C. D. Lin, Phys. Rev. A **82**, 035402 (2010).

[38] D. Dill and J. Dehmer, The Journal of Chemical Physics **61**, 692 (1974).

[39] S.-F. Zhao, C. Jin, A.-T. Le, T. F. Jiang, and C. D. Lin, Phys. Rev. A **81**, 033423 (2010).

[40] T. Morishita, A.-T. Le, Z. Chen, and C. D. Lin, Phys. Rev. Lett. **100**, 013903 (2008).

[41] A.-T. Le, R. R. Lucchese, S. Tonzani, T. Morishita, and C. D. Lin, Phys. Rev. A **80**, 013401 (2009).

[42] Z. Chen et al., Phys. Rev. A **74**, 053405 (2006).

[43] K. Schafer and K. Kulander, Physical Review A **42**, 5794 (1990).

[44] H. Muller and F. Kooiman, Physical review letters **81**, 1207 (1998).

[45] M. J. Nandor, M. A. Walker, L. D. Van Woerkom, and H. G. Muller, Phys. Rev. A **60**, R1771 (1999).

[46] D. Bauer, D. B. Milošević, and W. Becker, Phys. Rev. A **72**, 023415 (2005).

[47] C. P. J. Martiny, *Strong-field ionization of atoms and molecules by short femtosecond laser pulses*, PhD thesis, Aarhus University, 2010.

[48] D. Strickland and G. Mourou, Optics Communications **55**, 447 (1985).

[49] P. Maine, D. Strickland, P. Bado, M. Pessot, and G. Mourou, Quantum Electronics, IEEE Journal of **24**, 398 (1988).

[50] J. Shieh, F. Ganikhanov, K. Lin, W. Hsieh, and C. Pan, JOSA B **12**, 945 (1995).

[51] E. Ippen, L. Liu, and H. Haus, Optics letters **15**, 183 (1990).

[52] Y. Chou, J. Wang, H. Liu, and N. Kuo, Optics letters **19**, 566 (1994).

[53] A. Sennaroglu, *Solid-state lasers and applications*, volume 119, CRC, 2006.

[54] P. Kryukov, Quantum Electronics **31**, 95 (2001).

[55] K. Liu, C. Flood, D. Walker, and H. van Driel, Optics letters **17**, 1361 (1992).

[56] D. Spence, P. Kean, and W. Sibbett, Optics letters **16**, 42 (1991).

[57] A. Weiner, *Ultrafast optics*, volume 72, Wiley, 2011.

[58] G. Malcolm and A. Ferguson, Optics letters **16**, 1967 (1991).

[59] A. Gordon et al., Opt. Express **14**, 11142 (2006).

[60] R. W. Boyd, *Nonlinear optics*, Academic press, 2003.

[61] P. W. Milonni and Eberly, *Laser Physics*, Wiley Online Library, 2010.

[62] B. Shan, C. Wang, and Z. Chang, High peak-power kilohertz laser system employing single-stage multi-pass amplification, 2006, US Patent 7,050,474.

[63] J. L. Emmett, Laser system using regenerative amplifier, 1980, US Patent 4,191,928.

[64] J. I. Rudati, *A study of strong field double ionization of rare gases*, PhD thesis, State University of New York, 2003.

[65] D. E. Rivera, M. Morari, and S. Skogestad, Industrial & engineering chemistry process design and development **25**, 252 (1986).

[66] H. Wang et al., Applied Physics B: Lasers and Optics **89**, 275 (2007).

[67] E. Hecht, *Optics 4th*, Addison Wesley, 2002.

[68] M. Born and E. Wolf, *Principles of optics: electromagnetic theory of propagation, interference and diffraction of light*, CUP Archive, 1999.

[69] R. Cotter and D. Russell, Journal of the American Society for Mass Spectrometry **9**, 1104 (1998).

[70] C. P. João, J. Wemans, and G. Figueira, Applied Sciences **3**, 288 (2013).

[71] J. Zhou, C.-P. Huang, C. Shi, M. M. Murnane, and H. C. Kapteyn, Optics letters **19**, 126 (1994).

[72] V. Yanovsky, C. Felix, and G. Mourou, Selected Topics in Quantum Electronics, IEEE Journal of **7**, 539 (2001).

[73] R. Trebino et al., Review of Scientific Instruments **68**, 3277 (1997).

[74] D. J. Kane and R. Trebino, Quantum Electronics, IEEE Journal of **29**, 571 (1993).

[75] K. DeLong, R. Trebino, J. Hunter, and W. White, JOSA B **11**, 2206 (1994).

[76] R. Trebino and D. J. Kane, JOSA A **10**, 1101 (1993).

[77] Z. Chang, *Fundamentals of attosecond optics*, volume 1, CRC Press, 2011.

[78] M. L. Muga, Time-of-flight mass spectrometer, 1984, US Patent 4,458,149.

[79] G. Li and G. M. Hieftje, Time-of-flight mass spectrometer, 1997, US Patent 5,614,711.

[80] N. Mirsaleh-Kohan, W. D. Robertson, and R. N. Compton, Mass spectrometry reviews **27**, 237 (2008).

[81] M. Guilhaus, Journal of Mass Spectrometry **30**, 1519 (1995).

[82] S. Voss et al., Journal of Physics B: Atomic, Molecular and Optical Physics **37**, 4239 (2004).

[83] S. De et al., Phys. Rev. Lett. **103**, 153002 (2009).

[84] S. De et al., Phys. Rev. A **82**, 013408 (2010).

[85] D. Ray et al., Phys. Rev. Lett. **103**, 223201 (2009).

[86] J. H. Moore, C. C. Davis, M. A. Coplan, and S. C. Greer, Building Scientific Apparatus, by John H. Moore, Christopher C. Davis, Michael A. Coplan, Sandra C. Greer, Cambridge, UK: Cambridge University Press, 2009 **1** (2009).

[87] H. Goldstein, *Classical mechanics*, Addison-Wesley Pub. Co., 1980.

[88] C. Cornaggia et al., Physical Review A **44**, 4499 (1991).

[89] G. D. Gillen, M. Walker, and L. Van Woerkom, Physical Review A **64**, 043413 (2001).

[90] G. Paschmann, E. Shelley, C. Chappell, R. Sharp, and L. Smith, Review of Scientific Instruments **41**, 1706 (1970).

[91] J. Posthumus, Reports on Progress in Physics **67**, 623 (2004).

[92] H. Davis, Hearing research **9**, 79 (1983).

[93] E. Wells, M. J. DeWitt, and R. R. Jones, Phys. Rev. A **66**, 013409 (2002).

[94] A. Talebpour, C. Chien, and S. Chin, Journal of Physics B: Atomic, Molecular and Optical Physics **29**, L677 (1996).

[95] C. Guo, Physical review letters **85**, 2276 (2000).

[96] J. Muth-Böhm, A. Becker, S. Chin, and F. Faisal, Chemical physics letters **337**, 313 (2001).

[97] A. Jaroń-Becker, A. Becker, and F. Faisal, Physical Review A **69**, 023410 (2004).

[98] M. Okunishi, K. Shimada, G. Prümper, D. Mathur, and K. Ueda, The Journal of chemical physics **127**, 064310 (2007).

[99] F. Grasbon et al., Physical Review A **63**, 41402 (2001).

[100] X. Ren, J. Zhang, P. Liu, Y. Wang, and Z. Xu, Physical Review A **78**, 043411 (2008).

[101] A. Talebpour, S. Larochelle, and S.-L. Chin, Journal of Physics B: Atomic, Molecular and Optical Physics **31**, L49 (1998).

[102] A. M. Weiner, D. E. Leaird, J. S. Patel, and J. R. Wullert, Optics letters **15**, 326 (1990).

[103] A. M. Weiner et al., Quantum Electronics, IEEE Journal of **28**, 908 (1992).

[104] C. Radzewicz, P. Wasylczyk, W. Wasilewski, and J. Krasiski, Optics letters **29**, 177 (2004).

[105] D. Kaplan, T. Oksenhendler, and P. Tournois, Programmable acousto-optic device, 2003, US Patent App. 10/311,897.

[106] C. Hillegas, J. Tull, D. Goswami, D. Strickland, and W. Warren, Optics Letters **19**, 737 (1994).

[107] M. Roth, M. Mehendale, A. Bartelt, and H. Rabitz, Applied Physics B **80**, 441 (2005).

[108] M. Dugan, J. Tull, and W. Warren, JOSA B **14**, 2348 (1997).

[109] G. Gurzadëiìan, V. Dmitriev, and D. Nikogosëiìan, 3rd, rev. edition (Springer, Berlin (1999).

[110] A. N. Z. Rashed, Optical and Quantum Electronics , 1 (2012).

[111] A. M. Weiner, S. Enguehard, and B. Hatfield, Progress in Quantum Electronics **19**, 161 (1995).

[112] C. Palmer, E. G. Loewen, and R. Thermo, *Diffraction grating handbook*, Milton Roy, 1994.

[113] A. Siegman, How to (maybe) measure laser beam quality, in *Diode Pumped Solid State Lasers: Applications and Issues*, Optical Society of America, 1998.

[114] S. Hall and S. Knox, **85**, 012014 (2007).

[115] C. Roundy, Laser Focus World **35**, 119 (1999).

[116] T. F. Johnston, Applied optics **37**, 4840 (1998).

[117] S. Saghafi and C. Sheppard, Optics communications **153**, 207 (1998).

[118] A. E. Siegman and S. W. Townsend, Quantum Electronics, IEEE Journal of **29**, 1212 (1993).

[119] S. M. Hankin, D. M. Villeneuve, P. B. Corkum, and D. M. Rayner, Phys. Rev. A **64**, 013405 (2001).

Appendix A

Rate Equations

The purpose of this appendix is to provide a detailed solution to the rate equations for atomic ionization. We first derive the key results for single-electron ionization of atoms, which is the simplest ionization process we will consider. We then investigate the double ionization of atoms, where we consider depletion of the first charge state at high intensities. These derivations follows the derivation provided by Hankin *et al.* [119], but includes additional details which are relevant to our ionization studies.

A.1 Single Ionization

The general form of single ionization is given by $A \longrightarrow A^+$, where A represents a generic atomic species. The ionization probability to the first excited state as a function of time is given simply by $P_1(t) = 1 - P_0(t)$, where P_1 represents the probability of being in the first excited state, while P_0 is the probability of being in the ground (neutral) state. The so-called rate equation for the $A \rightarrow A^+$

Figure A.1: *Oscillator cavity of KLS. (a) is the layout of major optical elements present in the oscillator which are responsible for pulse formation. The oscillator achieves mode-locking by displacing the end mirror by a distance Δx. (b) shows a photograph of the Ti:Sapph crystal at the same orientation as the corresponding elements in (a). The crystal is located inside the lower indentation in the crystal holder in (b), where the crystal itself is approximately the size of a single grain of rice.*

transition is given by

$$\frac{\mathrm{d}P_0(t)}{\mathrm{d}t} = -w_{01}(r,t)P_0(t), \tag{A.1}$$

where $w_{01}(r,t)$ is the ionization rate from the neutral state. We can now solve (A.1),

$$\begin{aligned}\frac{\mathrm{d}P_0}{\mathrm{d}t} = -w_{01}(r,t)P_0(t) \longrightarrow \frac{1}{P_0(t)}\,\mathrm{d}P_0 &= -\,w_{01}(r,t)\,\mathrm{d}t \\ \ln\left[P_0(t)\right] &= -\int w_{01}(r,t)\,\mathrm{d}t \\ P_0(t) &= e^{-\int w_{01}(r,t)\,\mathrm{d}t}.\end{aligned}$$

Integrating this equation over time,

$$P_1(t) = 1 - e^{-\int w_{01}(r,t)\,\mathrm{d}t}. \tag{A.2}$$

Now, the yield, or the *signal*, S, is defined by

$$\mathrm{d}S(t) = P(t)\,\mathrm{d}V. \tag{A.3}$$

The signal in our case is determined by the volume element of our laser beam, which is given by $\mathrm{d}V = 2\pi\ell r\mathrm{d}r$. Inserting this expression as well as (A.2) into (A.3) yields

$$\mathrm{d}S_1(t) = P_1(t)\,\mathrm{d}V \longrightarrow S_1(t) = 2\pi\ell\int_0^R \left[1 - e^{-\int w_{01}(r,t)\,\mathrm{d}t}\right] r\mathrm{d}r. \tag{A.4}$$

At this point, it is important that we recognize that the transition rate, $W_0(r,t)$, is also a function of intensity, which in turn has a spatial dependence on r. We now wish to undergo a change in variables, such that the spatial integral in (A.4) is reformed in terms of an integral over intensity:

$$S_1(t) = 2\pi\ell\int_0^R \left[1 - e^{-\int w_{01}(r,t)\,\mathrm{d}t}\right] r\frac{\mathrm{d}r}{\mathrm{d}I}\,\mathrm{d}I \tag{A.5}$$

We now recall that $I(r=R)=I_0$, the *peak intensity*, we find that we can decouple the integral equation from the explicit dependence on the spatial coordinate r. Therefore,

$$S_1(t) = 2\pi\ell\left(\frac{R^2}{2}\right)\int_0^{I_0}\left[1-e^{-\int w_{01}(I,t)\,\mathrm{d}t}\right]\cdot\frac{1}{I}\,\mathrm{d}I$$

$$\longrightarrow \boxed{S_1(t) = \pi\ell R^2\int_0^{I_0}\left[1-e^{-\int w_{01}(I,t)\,\mathrm{d}t}\right]\cdot\frac{1}{I}\,\mathrm{d}I} \tag{A.6}$$

A.2 Double Ionization

It is now time to acknowledge the presence of second atomic ionization processes, which can be populated via two distinct mechanisms:

$$A \xrightarrow{w_{01}(r,t)} A^{+} \xrightarrow{w_{12}(r,t)} A^{++} \tag{A.7a}$$

$$A \xrightarrow{w_{02}(r,t)} A^{++} \tag{A.7b}$$

where (A.7a) represents *sequantial* ionization, whereas (A.8a) represents the *non-sequential* ionization, as discussed in §1.3.1 and §1.3.2 on pgs. 11 and 12, respectively. Let's assume that the production of doubly charged ions is strictly sequential, which is described by (A.7a). Even though the process $A \longrightarrow A^{+}$ was already investigated, we are unable to use our previous results because the population of the first ion will be effected by the presence of second ions. Therefore, our rate equations are:

$$\frac{\mathrm{d}P_0(t)}{\mathrm{d}t} = -w_{01}(r,t)P_0(t) \tag{A.8a}$$

$$\frac{\mathrm{d}P_1(t)}{\mathrm{d}t} = w_{01}(r,t)P_0(t) - w_{12}(r,t)P_1(t) \tag{A.8b}$$

$$\frac{\mathrm{d}P_2(t)}{\mathrm{d}t} = w_{12}(r,t)P_1(t) \tag{A.8c}$$

The solution for (A.8a) was previously evaluated,

$$\frac{\mathrm{d}P_0(t)}{\mathrm{d}t} = -w_{01}(r,t)P_0(t) \longrightarrow P_0(t) = e^{-\int w_{01}(r,t)\,\mathrm{d}t}. \tag{A.9}$$

Solving (A.8b) is not quite as straightforward. This first-order non-homogeneous differential equations is most easily solved by the introduction of an *integrating factor*, denoted μ. Let's first rewrite (A.8b) slightly:

$$\frac{\mathrm{d}P_1(t)}{\mathrm{d}t} + w_{12}(r,t)P_1(t) = w_{01}(r,t)P_0(t) \tag{A.10}$$

Defining our integrating factor as $\mu = e^{\int w_{12}(r,t)\,\mathrm{d}t}$. Multiplying both sides of (A.10) by μ yields

$$\mu\frac{\mathrm{d}P_1(t)}{\mathrm{d}t} + \mu w_{12}(r,t)P_1(t) = \mu w_{01}(r,t)P_0(t) \tag{A.11}$$

We now notice that

$$\frac{\mathrm{d}\mu}{\mathrm{d}t} = \frac{\mathrm{d}}{\mathrm{d}t}e^{\int w_{12}(r,t)\,\mathrm{d}t} \Rightarrow \mu w_{12}(r,t)$$

Substituting this back into (A.11),

$$\begin{aligned}
\mu\frac{\mathrm{d}P_1(t)}{\mathrm{d}t} + \frac{\mathrm{d}\mu}{\mathrm{d}t}P_1(t) &= \mu w_{01}(r,t)P_0(t) \\
\frac{\mathrm{d}}{\mathrm{d}t}\left[\mu P_1(t)\right] &= \mu w_{01}(r,t)P_0(t) \\
P_1(t) &= \frac{1}{\mu}\int \mu w_{01}(r,t)P_0(t)\,\mathrm{d}t \\
&= e^{-\int w_{12}(r,t)\,\mathrm{d}t}\int e^{\int w_{12}(r,t)\,\mathrm{d}t} w_{01}(r,t)P_0(t)\,\mathrm{d}t
\end{aligned} \tag{A.12}$$

We can now solve (A.8c) in precisely the same way we did for (A.8a). The result is

$$\frac{\mathrm{d}P_2(t)}{\mathrm{d}t} = w_{12}(r,t)P_1(t) \longrightarrow P_2(t) = e^{\int w_{12}(r,t)\,\mathrm{d}t}. \tag{A.13}$$

Summarizing our main results,

$$P_0(t) = e^{-\int w_{01}(r,t)\,\mathrm{d}t} \tag{A.14a}$$

$$P_1(t) = e^{-\int w_{12}(r,t)\,\mathrm{d}t}\int e^{\int w_{12}(r,t)\,\mathrm{d}t} w_{01}(r,t)P_0(t)\,\mathrm{d}t \tag{A.14b}$$

$$P_2(t) = e^{\int w_{12}(r,t)\,\mathrm{d}t}$$

and now substituting (A.14a) into (A.14b), our new set of equations becomes

$$P_0(t) = e^{-\int w_{01}(r,t)\,\mathrm{d}t} \tag{A.15a}$$

$$P_1(t) = e^{-\int w_{12}(r,t)\,\mathrm{d}t} \int e^{\int [w_{12}(r,t) - w_{01}(r,t)]\,\mathrm{d}t} w_{01}(r,t)\,\mathrm{d}t \tag{A.15b}$$

$$P_2(t) = e^{\int w_{12}(r,t)\,\mathrm{d}t} \tag{A.15c}$$

We see that (A.15a)-(A.15c) represents the population of each charged state as a function of the ionization rates for each transition. The functional form of the ionization rates are determined by theoretical models, such as ADK, PPT, MO-ADK and so on. Until a specific model is chosen, the integrals in (A.15a)-(A.15c) must remain arbitrary.

[This page intentionally left blank]

Appendix B

Intensity Calibration

B.1 Introduction

The purpose of this section is to provide details on the intensity calibration used in our molecular ionization experiments. This includes the derivation of a relationship between various parameters in the experiment – mainly intensity, energy, and pulse duration. Furthermore, experimental techniques are included as a supplement.

B.2 Connecting Intensity to $E_{\mathbf{n}}$, τ, and w_0

We begin our journey by defining several key quantities:

$$P_{\text{avg}} = \frac{\text{Energy of Pulse}}{\text{Period of Laser}} \Rightarrow \frac{E_{\text{n}}}{T}, \qquad P_{\text{pk}} = \frac{\text{Energy of Pulse}}{\text{Duration of pulse}} \Rightarrow \frac{E_{\text{n}}}{\tau}$$
$$I_{\text{avg}} = \frac{\text{Average Power}}{\text{Area}} = \frac{P_{\text{avg}}}{\text{Area}} \Rightarrow \frac{E_{\text{n}}}{A \cdot T}, \qquad I_{\text{pk}} = \frac{\text{Peak Power}}{\text{Area}} = \frac{P_{\text{pk}}}{\text{Area}} \Rightarrow \frac{E_{\text{n}}}{A \cdot \tau}$$

where T is the period of the laser ($T = 1/f$), and τ is the Full Width at Half Maximum (FWHM) of the laser pulse. The equation for a vanilla-plain normalized Gaussian function is given by

$$f(x) = \exp\left[\frac{-x^2}{2\sigma^2}\right], \tag{B.1}$$

where σ is the standard deviation in space. It is important to recognize that the size of our beam, quantified by the *spot size*, or $w(z)$, is measured in terms of the distance from the center of the beam, *i.e.* a radius. The spatial variable, x, in (B.1) is measured as a total distance, not necessarily from the mean of the profile. So, in order to convert x to a half-width, we must introduce a factor of $1/2$, which is included in (B.1). We also note that the spot size is defined by the $1/e^2$ distance, as opposed to the FWHM (See Fig. B.1).

The intensity of a Gaussian is given in both space and time by

$$I(r,z,t) = I_0 \exp\left[\frac{-r^2}{w(z)^2} - \frac{t^2}{\sigma_\tau^2}\right], \tag{B.2}$$

where r is the radius from the beam center, and $w(z)$ is the spot size of the beam, measured from the center to the $1/e^2$ point. We also recognize that σ_τ is the standard deviation of the pulse duration of the laser. However, we actually measure the FWHM of the pulse duration, and in order to find an equation linking the FWHM to the standard deviation we take the equation for a normalized Gaussian, and evaluate it at half of its maximum value:

$$0.5 = \exp\left[\frac{-t^2}{2\sigma_\tau^2}\right]. \tag{B.3}$$

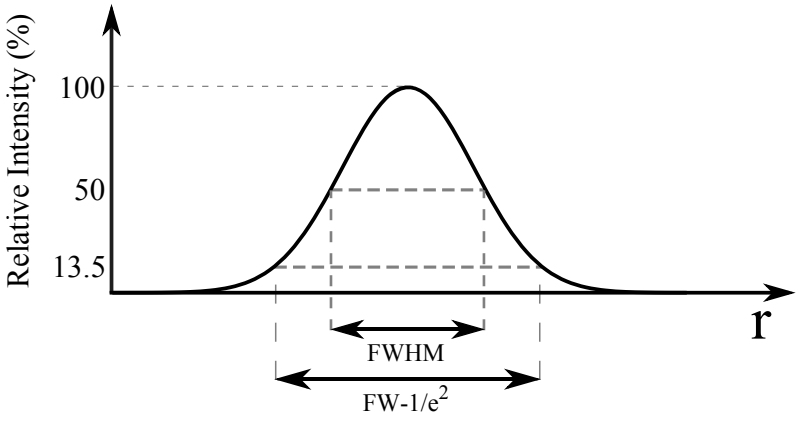

Figure B.1: *A Gaussian profile, with designations for both the FWHM and the* $1/e^2$ *point.*

At this point, we take $t \rightarrow \text{FWHM}_\tau/2$, and (B.3) becomes

$$0.5 = \exp\left[\frac{-(\text{FWHM}_\tau/2)^2}{2\sigma_\tau^2}\right] \longrightarrow \ln 2 = \frac{\text{FWHM}_\tau^2}{8\sigma_\tau^2} \longrightarrow \text{FWHM}_\tau = 2\sqrt{2\ln 2}\,\sigma_\tau. \tag{B.4}$$

Substituting (B.4) into (B.2) yields*

$$I(r,z,t) = I_0 \exp\left[\frac{-r^2}{w(z)^2} - \frac{4\ln 2\, t^2}{\tau^2}\right] \tag{B.5}$$

We can now separate (B.5) into both the space part and the time part:

$$I(r,z,t) = I(r,z)\cdot I(t) = \underbrace{I_0 \exp\left[\frac{-r^2}{w(z)^2}\right]}_{\text{Space Part}} \cdot \underbrace{\exp\left[\frac{-4\ln 2\, t^2}{\tau^2}\right]}_{\text{Time Part}} \tag{B.6}$$

To find the peak intensity, we examine the spatial part of (B.6) at $z = 0$, where the spot size is at a minimum value (appropriately called the *minimum spot size*, or w_0). To do this, we set $w(z) \rightarrow w_0$, and the spatial part of (B.6) becomes:

$$I(r,0) = I_0 \exp\left[\frac{-r^2}{w_0^2}\right] \tag{B.7}$$

We recall that power is defined as energy per unit area, while intensity is energy per unit area per unit time. So, we can find the power by integrating the intensity over space from (B.7), and then the energy by integrating over the temporal function from (B.6):

$$E_\text{n} = \int I(r,0)\,\text{d}A \cdot \int I(t)\,\text{d}t. \tag{B.8}$$

Let's perform the spatial integration first by substituting (B.7) into the first integral in (B.8):

$$P = \int_{-\infty}^{\infty} I_0 \exp\left[\frac{-r^2}{w_0^2}\right]\,\text{d}A \tag{B.9}$$

*For notational convenience we denote $\text{FWHM}_\tau \rightarrow \tau$ from this point forward.

And we now recall that $\mathrm{d}A = 2\pi r \mathrm{d}r$, and (B.9) becomes,

$$\begin{aligned}
P =& \pi I_0 \int_{-\infty}^{\infty} \exp\left[\frac{-r^2}{w_0^2}\right] 2r\mathrm{d}r \quad \left.\begin{array}{l} u = r^2 \\ \mathrm{d}u = 2r\mathrm{d}r \end{array}\right\} \\
=& \pi I_0 \int_{-\infty}^{\infty} \exp\left[\frac{-u}{w_0^2}\right] \mathrm{d}u \\
=& 2\pi I_0 \int_{0}^{\infty} \exp\left[\frac{-u}{w_0^2}\right] \mathrm{d}u \\
=& 2\pi I_0 \left[-\frac{w_0^2}{2} \exp\left[-\frac{u}{w_0^2}\right]\right]\Bigg|_0^{\infty} \\
=& \pi I_0 w_0^2. \qquad \text{(B.10)}
\end{aligned}$$

Substituting (B.10) as well as the temporal function from (B.6) back into (B.8),

$$\begin{aligned}
E_{\mathrm{n}} =& \pi I_0 w_0^2 \int_0^{\infty} \exp\left[\frac{-4\ln 2\, t^2}{\tau^2}\right] \mathrm{d}t \quad \left.\begin{array}{l} \\ \\ \end{array}\right\} \quad \text{Let } a = \frac{4\ln 2}{\tau^2} \\
=& \pi I_0 w_0^2 \int_0^{\infty} \exp\left[-at^2\right] \mathrm{d}t \\
=& \frac{\pi I_0 w_0^2}{2} \sqrt{\frac{\pi}{a}} \\
=& \frac{\pi I_0 w_0^2}{2} \sqrt{\frac{\pi\tau^2}{4\ln 2}} \qquad \text{(B.11)}
\end{aligned}$$

Solving (B.11) for I_0, we are left with

$$\boxed{I_0 = \frac{4E_{\mathrm{n}}}{\pi w_0^2 \tau} \sqrt{\frac{\ln 2}{\pi}}} \qquad \text{(B.12)}$$

This represents a key result, which will be used to calibrate the intensity in our data sets. The implementation of (B.12) is presented in §3.3 on pg. 48 of this document.